AN ABSTRACT OF THE THESIS OF

Catherine A. Remley for the degree of Doctor of Philosophy in Electrical and Computer Engineering presented on March 16, 1999.

Title: Time Domain Modeling of Electromagnetic Radiation with Application to Ultrafast Electronic and Wireless Communication Systems.

Redacted for Privacy

Abstract approved: _____

Andreas Weisshaar

A versatile computational technique for improved time domain modeling of electromagnetic radiative systems is demonstrated. Two computational methods are combined: the finite-difference time domain (FDTD) method, a full-wave electromagnetic field solver, and the Kirchhoff surface integral formulation, a spatial transformation technique. The combined FDTD/Kirchhoff technique is shown to increase accuracy and efficiency in the analysis of a wide variety of electronic systems. Two approaches to the implementation of the Kirchhoff surface integral formulation are discussed, using exact expressions and using the FDTD method for the generation of the components of the integral. Several examples are presented which validate the technique and illustrate the roles of the various components.

Utilizing the combined FDTD/Kirchhoff technique, improved modeling of radiative systems is presented in two applications. The first involves characterization of broadband non-time-harmonic radiation from an ultrafast electronic system. Increased accuracy in the representation of the far-field radiation arising from a photoconducting structure is demonstrated by inclusion of inhomogeneous material parameters such as the substrate and metal electrodes. By comparison of results with those from the FDTD/Kirchhoff method, a simple technique is developed for obtaining the far-field radiation by considering the edges of the substrate as secondary diffracting sources.

In the second application, the accuracy of a commonly used propagation modeling technique, the ray-tracing method, is investigated as the size of local scatterers approaches the wavelength of operation. By comparison with results from the FDTD/Kirchhoff technique, the accuracy of the ray-tracing method for scatterer sizes down to a fraction of a wavelength is demonstrated. Additionally, the FDTD/Kirchhoff technique is used in developing improvement terms for a set of heuristically derived diffraction coefficients, the Luebbers' coefficients, that are frequently used in the ray-tracing method. The thesis ends with an examination of the applicability of the FDTD/Kirchhoff method to various simulation scenarios. The use of this technique as a standard to assist in the assessment, improvement, and development of more computationally efficient methods is discussed, and recommendations for future work are given.

Time Domain Modeling of Electromagnetic Radiation with Application to Ultrafast Electronic and Wireless Communication Systems

by

Catherine A. Remley

A THESIS

submitted to

Oregon State University

in partial fulfillment of
the requirements for the
degree of

Doctor of Philosophy

Completed March 16, 1999
Commencement June 1999

Doctor of Philosophy thesis of Catherine A. Remley presented on March 16, 1999

APPROVED:

Redacted for Privacy

Major Professor, representing Electrical and Computer Engineering

Redacted for Privacy

Chair of the Department of Electrical and Computer Engineering

Redacted for Privacy

Dean of the Graduate School

I understand that my thesis will become part of the permanent collection of Oregon State University libraries. My signature below authorizes release of my thesis to any reader upon request.

Redacted for Privacy

Catherine A. Remley, Author

ACKNOWLEDGMENTS

I would like to express my gratitude to the National Science Foundation for the award of a three-year Graduate Research Fellowship which enabled research in areas of special interest. Additionally, support from NSF grant ECS-9312240 aided in research on modeling radiation from ultrafast electronic systems, and support from EDX Engineering assisted in the area of propagation modeling.

I would especially like to thank my advisor, Andreas Weisshaar, for his continued guidance and support throughout my graduate career. The love of learning imparted to me by my parents, Fred and Anne Remley, has made graduate school a much richer experience.

TABLE OF CONTENTS

TABLE OF CONTENTS (Continued)

LIST OF FIGURES

LIST OF FIGURES (Continued)

LIST OF FIGURES (Continued)

LIST OF FIGURES (Continued)

LIST OF FIGURES (Continued)

LIST OF FIGURES (Continued)

LIST OF TABLES

LIST OF APPENDICES

LIST OF APPENDIX FIGURES

TIME DOMAIN MODELING OF ELECTROMAGNETIC RADIATION WITH APPLICATION TO ULTRAFAST ELECTRONIC AND WIRELESS COMMUNICATION SYSTEMS

1. INTRODUCTION

Accurate computational modeling of radiative effects has become a significant aspect of circuit and system design, particularly with the increased availability of portable personal communication devices [1]. Increased precision in fabrication techniques has enabled large-scale circuit integration, with the incorporation of hundreds or even thousands of components into a single package or circuit board. This, in turn, has led to the development of high-speed, compact devices such as laptop computers and personal communications systems (pagers, cellular phones, wireless modems, etc.). Radiative effects can be significant in these high speed, often digital, circuits and systems. The radiation may be desirable, as in the received signal from a personal communication system, or parasitic, as in crosstalk caused by the crowding of components on a circuit board.

The increased precision in fabrication techniques which has enabled large-scale integration has also led to the development of many ultrafast electronic circuits and systems in which the wavelength of excitation is on the order of feature size. For example, one type of ultrafast device, the electro-optic modulator, typically may have an electrode length of 4-8 mm, which is electrically equivalent to roughly a quarter to a half wavelength of the free space microwave modulating frequency of, for example, 15 GHz [2, 3]. Parasitic radiation in ultrafast electronic circuitry can be extremely troublesome since components with feature sizes on the order of a wavelength may easily act as radiating elements.

Computational modeling is essential for the design of radiative systems and it can also reduce the need for difficult and time-consuming measurements of some systems. Modeling can be carried out either in the time domain (where the time evolution of a signal or system is considered) or in the frequency domain (where the phase and frequency response of a system are considered). In some situations, time domain modeling has important advantages.

Efficient characterization of systems with broadband and/or non-time-harmonic excitation is one of the strengths of time domain modeling. For example, time domain models are often used for analysis of transient effects such as time dispersion and crosstalk in digital circuits [4]–[6]. For many years, time domain analysis has been commonly used on pulsed transmission lines and antenna systems [7]–[10]. Recently, time domain techniques are also finding use in the analysis of ultrafast electronic systems with non-time-harmonic excitation, such as photoconducting switches [11, 12] and photoconducting antenna structures [13, 14].

With the advent of digitally-modulated communication systems, time domain field analysis finds increasing use in channel characterization [15]–[17] as well. Instantaneous parameters such as power delay spread and fast fading of multipath signals may be accurately and efficiently determined. Mobile communication systems with time-varying channel parameters may be more easily characterized in the time domain than in the frequency domain [18]–[20].

There are several areas, however, in which difficulties are encountered in time domain computational modeling. For example, characterization of radiation from structures with arbitrary inhomogeneous material parameters, such as those found in ultrafast electronic systems, has historically been difficult. Analytical expressions are generally not available for the electromagnetic fields in systems which include a variety of materials. Numerical techniques capable of including such material inhomogeneity tend to be computationally intensive, particularly so because a fine level of detail is often required to describe the radiating components.

Another area in which modeling difficulties may be encountered is the characterization of propagation in wireless communication systems. When a detailed description of the propagation environment is included in the model, standard computational techniques often become very complex, and thus, computationally inefficient. Approximate numerical techniques exist which are computationally efficient but which require large feature size of objects in the simulation space with respect to the wavelength of operation for accurate results. As the limits of this requirement are approached, these techniques may give er-

roneous results. Additionally, these techniques sometimes utilize heuristically developed parameters which may introduce inaccuracy into simulation results.

The goal of the present work is to improve both the accuracy and the efficiency of time-domain techniques for the modeling of electromagnetic systems such as those just described. A versatile full-wave time domain computational technique, capable of characterizing a wide variety of electronic systems, is developed. Utilizing this technique, improved modeling of radiative systems is presented in two applications. The first application involves characterization of broadband non-time-harmonic radiation from an ultrafast electronic system. Increased accuracy in the representation of the far-field radiation arising from a photoconducting structure is demonstrated using the full-wave technique. Then, by comparison to results generated using the full-wave method, a computationally efficient technique for modeling the far-field radiation from the photoconducting structure is developed. In the second application, the accuracy of a commonly used propagation modeling technique, the ray-tracing method, is investigated as the limits of its inherent approximations are approached. Errors are quantified by comparison to the full-wave computational technique developed in this thesis. Additionally, the full-wave technique is used in developing improvement terms for a heuristically derived parameter frequently used in the ray-tracing method.

1.1 Time Domain Modeling Techniques for Radiative Systems

Several commonly used modeling techniques for radiative electromagnetic systems can incorporate time domain effects. One of the most simple techniques is the direct calculation of radiation from a known excitation (generally, a current density distribution or a dipole moment). In a limited number of cases, analytic expressions are available [7, 21, 22]. More generally, the Method of Moments (MoM) combined with Green's function techniques can be used to find radiation for structures with simple geometries [23, 24]. This technique typically requires use of the Fourier transform to obtain time domain information. Recently, however, hybrid methods combining the MoM with time domain techniques have been proposed [25, 26].

As the frequency of operation rises and the feature sizes approach the wavelength of operation, the ability to include arbitrary environmental and/or device material parameters becomes increasingly important. Finite-element and finite-difference techniques are extremely versatile in this respect, and may easily be implemented in the time domain. The finite-difference time domain (FDTD) technique [27]–[29] is a commonly used time domain method which can be accurate over a wide frequency range. This technique may incorporate arbitrary excitation, including discrete, distributed, and multiple sources, and can provide for accurate representation of radiating elements. Increased computing power enabled by large-scale integration has made computationally intensive techniques such as the FDTD method viable.

Computational efficiency can be substantially increased when a spatial transformation technique is combined with the FDTD method. Spatial transformation techniques may have either scalar [21], [30] - [39] or vector form [40] - [55]. These "equivalent source" techniques are based on Huygens' Principle, which states that a point on an expanding wavefront can be used as a new source of radiation [31]. An advantage of most spatial transformation techniques is that they may be incorporated into the FDTD method in a straightforward manner.

One final computational modeling technique is the ray-tracing method [56]–[58]. Although it is a frequency domain technique, it may easily provide time domain propagation characteristics such as power delay profile and delay spread. Ray-tracing is based on Geometrical Optics [56, 59] and the Uniform Theory of Diffraction [60]–[62]. Signals are represented as ray "tubes," cylinders of extremely small diameter in which cross-sectional phase and amplitude are constant. The ray-tracing technique is a high frequency approximation, i.e., it is assumed that the wavelength of operation is much smaller than the size of local scatterers.

1.2 Organization of the Present Work

Chapter 2 presents the development of a computational technique combining the FDTD method and the Kirchhoff surface integral formulation, a scalar spatial transforma-

tion technique. Derivations of both the FDTD and the combined FDTD/Kirchhoff technique are presented, and two approaches to the implementation of the Kirchhoff surface integral formulation are discussed. The first approach involves the use of exact expressions for the generation of the components of the integral. This formulation enables a very efficient solution for cases where an analytic expression exists for the source fields. The second approach uses the FDTD method to calculate the source fields. This is useful for simulations of structures with inhomogeneous material parameters or complex sources. Several examples are presented which validate the technique and illustrate the roles of the various components of the integral. Implementation and analysis of this spatial transformation technique are important contributions of this thesis, so these aspects are discussed in some detail.

In Chapters 3 and 4, the combined FDTD/Kirchhoff technique is utilized in two diverse applications. In Chapter 3, the technique is applied to the characterization of the broadband radiation from a photoconducting structure. The physics of radiation generation from the structure are first presented, and a commonly used technique for characterizing the radiation is described. Then, simulation results provided by the FDTD/Kirchhoff technique are used to deduce a very computationally efficient model for radiation from the gallium arsenide substrate of the photoconducting structure. Finally, it is shown that the FDTD/Kirchhoff technique applied to the full photoconducting structure provides a more accurate portrait of the far-field radiation than has previously been reported.

A second application of the FDTD/Kirchhoff technique is presented in Chapter 4, where indoor propagation is modeled using both the FDTD/Kirchhoff technique and the ray-tracing method. The accuracy of the ray-tracing technique is quantified for several different propagation configurations as feature size approaches the wavelength of operation by comparison to results found using the FDTD and the combined FDTD/Kirchhoff method. Additionally, a method for improving the accuracy of a commonly used diffraction coefficient in the ray-tracing method is heuristically derived. The thesis ends with a conclusion and recommendations for future work.

2. DEVELOPMENT OF A COMPUTATIONAL TECHNIQUE COMBINING THE FINITE-DIFFERENCE TIME DOMAIN METHOD WITH THE KIRCHHOFF SURFACE INTEGRAL FORMULATION

In this chapter, two time domain computational techniques are combined to increase the accuracy and efficiency of modeling for certain radiative systems. As mentioned in Chapter 1, the finite-difference time domain (FDTD) method is a well-established computational technique capable of characterizing radiation and scattering in environments with objects of arbitrary shape and material parameters. All six Cartesian field components are accessible at discrete grid cell locations throughout the computational domain. However, in some situations, observation of the fields at the FDTD grid cell points does not provide sufficient information. Problems may arise, for example, if the observation point is far from the radiative system or is outside the computational domain. Another potential problem arises when the observation point is located between FDTD grid cell points. These problematic situations often arise in the modeling of ultrafast electronic systems, where a high level of structural detail representing a small physical region may necessitate a large computational domain (due to small grid cell size). Observation points external to the computational domain may be required in this case. A similar situation may arise in propagation modeling, where the observation point may be located many wavelengths from the source or from scattering interactions. Additionally, the fields available at the FDTD grid cell points may not provide sufficient or accurate enough information, that is, it may be necessary to specify observation points between grid cell locations.

In these cases, the FDTD method may be combined with a spatial transformation technique, enabling determination of the fields at analytically specified observation points. The observation points may be located either far from the source and/or scattering interactions, or between FDTD grid cell locations. In a spatial transformation technique, the field on a virtual surface surrounding the source or scatterers is integrated with respect to an external observation point. The results of the integration are used to determine the time evolution of the field at the observation point. The combination of the FDTD method

with a spatial transformation technique may increase accuracy because the observation points can be analytically assigned. This approach can also enhance efficiency since field calculation is not required beyond the virtual surface.

In this chapter, a review of the finite-difference time domain technique is first presented. The governing equations are developed and important implementation considerations are discussed. Then, a scalar spatial transformation technique, the Kirchhoff surface integral formulation, is presented. The combination of the Kirchhoff surface integral with the FDTD method is heavily utilized in the present work for the characterization of radiative systems. Analysis, implementation, and application of this technique are major contributions of this thesis, and are therefore presented with a high level of detail. Two different techniques for calculation of the surface fields are presented, one based on analytic expressions, and one based on the FDTD method. Then, new work is presented demonstrating the way in which the components of the integral combine to give an accurate final solution. Several examples are given to demonstrate and validate the implementation of the Kirchhoff surface integral formulation.

2.1 Review of the Finite-Difference Time Domain Method

The finite-difference time domain (FDTD) technique [27, 28, 29, 63] is a versatile numerical method that enables incorporation of arbitrary three-dimensional geometries and a wide range of material parameters into the problem space. Since it is a time domain technique, broadband response predictions are possible with a single excitation. A comparable frequency domain technique would require simulations at several different frequencies followed by a Fourier transformation to the time domain.

The FDTD method can incorporate material parameters ranging from perfect conductors to perfect dielectrics, as well as lossy dielectric, anisotropic, and magnetic. As a result, it is well-suited to the analysis of many types of electromagnetic systems. The FDTD method has been used for a wide variety of applications including microwave circuit analysis [4, 5, 64, 65], optical/photoconducting system analysis [11, 66, 67], and scattering problems [68, 44, 69, 70]. In the analysis of radiative systems, one advantage of the FDTD

technique is that it can model both the physical source of radiation and the materials of the propagation environment [9, 47, 71, 72]. An extensive survey of FDTD literature may be found in Ref. [73].

In the FDTD method, the differential forms of Maxwell's equations are discretized in time and space and are solved iteratively in an alternating fashion. First, the electric field equations are solved, and then these results are used to solve the magnetic field equations. Field component values are accessible throughout the simulation space at each time step, enabling determination of a variety of response quantities such as antenna patterns, scattered fields, surface currents, radar cross section (RCS), penetration, and coupling [74].

In the simulation of a problem in an infinite (open) domain, such as propagation in free space, the problem space must be terminated in boundary conditions that prevent reflections of outgoing waves. Several types of absorbing boundary conditions (ABCs) have been developed over the years [21, 75, 76, 77]. In 1994, Berenger developed the Perfectly Matched Layer (PML) [77] which utilizes a fictitious magnetic loss for impedance matching of the outgoing wave to a highly lossy material. The PML effectively attenuates outgoing waves over a wide frequency range and over a wide range of angles of incidence. It is currently considered the state of the art for absorbing boundary conditions and is utilized in all FDTD simulations presented in this thesis.

In the following section, a brief derivation of FDTD equations in the context of the Yee cell [27] is presented, and important aspects of accurate FDTD implementation are discussed, including grid cell size and time step size. A discussion of numerical phase velocity follows, with an example demonstrating the undesirable dispersive effect which is implicit in the FDTD formulation.

2.1.1 The Yee Cell and FDTD Equations

The differential form of Maxwell's equations in the time domain may be given as

$$\nabla \times \vec{H} = \epsilon \frac{\partial \vec{E}}{\partial t} - \vec{J} \tag{2.1}$$

$$\nabla \times \vec{E} = -\mu \frac{\partial \vec{E}}{\partial t} - \vec{M} \tag{2.2}$$

where electric current density $\vec{J}$ may represent either actual or equivalent sources, and the magnetic current density $\vec{M}$ represents equivalent sources [78].

In Cartesian coordinates, these equations can be discretized as follows [79]:

$$\frac{\partial H_x}{\partial t} = \frac{1}{\mu}\left(\frac{\partial E_y}{\partial z} - \frac{\partial E_z}{\partial y}\right) - M_x \tag{2.3}$$

$$\frac{\partial H_y}{\partial t} = \frac{1}{\mu}\left(\frac{\partial E_z}{\partial x} - \frac{\partial E_x}{\partial z}\right) - M_y \tag{2.4}$$

$$\frac{\partial H_z}{\partial t} = \frac{1}{\mu}\left(\frac{\partial E_x}{\partial y} - \frac{\partial E_y}{\partial x}\right) - M_z \tag{2.5}$$

$$\frac{\partial E_x}{\partial t} = \frac{1}{\epsilon}\left(\frac{\partial H_z}{\partial y} - \frac{\partial H_y}{\partial z}\right) - J_x \tag{2.6}$$

$$\frac{\partial E_y}{\partial t} = \frac{1}{\epsilon}\left(\frac{\partial H_x}{\partial z} - \frac{\partial H_z}{\partial x}\right) - J_y \tag{2.7}$$

$$\frac{\partial E_z}{\partial t} = \frac{1}{\epsilon}\left(\frac{\partial H_y}{\partial x} - \frac{\partial H_x}{\partial y}\right) - J_z \tag{2.8}$$

In the Yee cell formulation, it is assumed that the electric fields are updated at time step n and that the magnetic fields are updated at time step $n + \frac{1}{2}$. Using centered differences and field components as specified in the Yee cell (Figure 2.1), the discretized Maxwell's equations can be written as follows:

$$E_z^{n+1}(i,j,k+0.5) = E_z^n(i,j,k+0.5) +$$

$$\frac{\Delta t}{\epsilon}\left[\frac{H_y^{n+0.5}(i+0.5,j,k+0.5) - H_y^{n+0.5}(i-0.5,j,k+0.5)}{\Delta x} - \right.$$
$$\left.\frac{H_x^{n+0.5}(i,j+0.5,k+0.5) - H_x^{n+0.5}(i,j-0.5,k+0.5)}{\Delta y} - J_z^{n+0.5}(i,j,k+0.5)\right] \tag{2.9}$$

$$H_x^{n+0.5}(i,j+0.5,k+0.5) = H_x^{n-0.5}(i,j+0.5,k+0.5) -$$

$$\frac{\Delta t}{\mu}\left[\frac{E_z^n(i,j+1,k+0.5) - E_z^n(i,j,k+0.5)}{\Delta y} - \right.$$
$$\left.\frac{E_y^n(i,j+0.5,k+1) - E_y^{n+0.5}(i,j+0.5,k)}{\Delta z} - M_x^n(i,j+0.5,k+0.5)\right] \tag{2.10}$$

where (2.9) and (2.10) are examples of the centered difference equations based on the Yee cell for two field components.

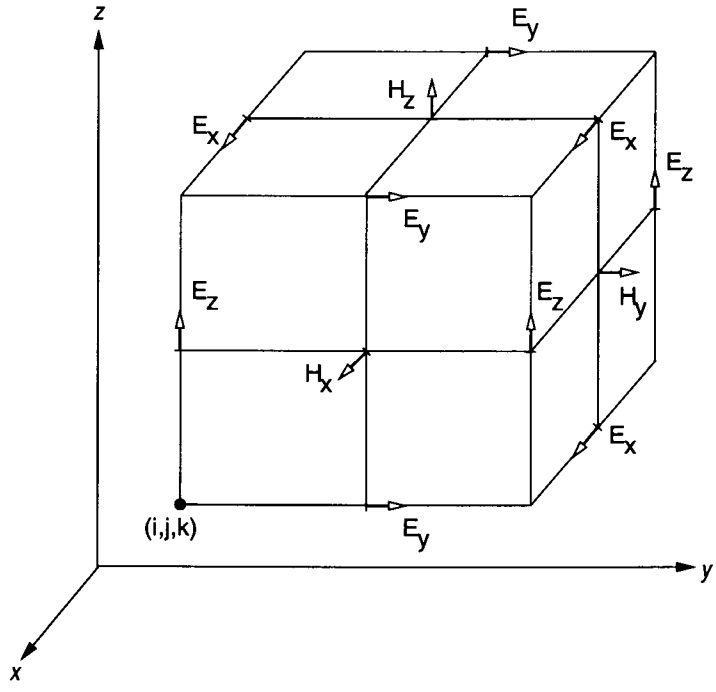

Figure 2.1: Positions of the field components in the Yee cell.

2.1.2 Creating the Grid: Cell Size and Time Step Size

The grid cell size chosen for use in a particular FDTD simulation is typically based on minimizing the effects of numerical dispersion (a phenomenon discussed in the next section). Generally the grid cell size is determined first and then the time step size is based on this calculation. If the highest significant frequency component in the simulation has a wavelength given by λ_u in material medium, it has been found that the cell size should generally be smaller than $\lambda_u/10$ [29, 80]. The required level of discretization beyond $\lambda_u/10$ depends on several factors including the following:

- The degree of geometrical detail required in describing objects in the propagation environment.

- The frequency considered to be the "highest significant frequency component." See, for example, Figure 4.4, where the highest frequency component is arbitrarily defined as 10 dB below the signal level at the carrier frequency.

Once the grid cell size is determined, the time step, Δt, can be ascertained. In a single time step, the farthest a signal can propagate in the FDTD algorithm is from one cell to its nearest neighbors. Therefore, any point on a propagating wave must not travel farther than one grid cell in one time step [74]. For a cubic grid cell and a given velocity of propagation, this sets a limit on the maximum time step size, i.e.,

$$\Delta t \leq \frac{\Delta s}{c\sqrt{3}} \tag{2.11}$$

where $\Delta x = \Delta y = \Delta z = \Delta s$, $\sqrt{3}\Delta s$ is the distance along the diagonal of a cube, and c is the velocity of propagation in free space. In fact, the *Courant stability condition*, outlined in [63], is the generally accepted rule for determining time step size in an FDTD grid where Δx is not necessarily equal to Δy, etc. It is based on (2.11), and is given as

$$\Delta t \leq \frac{1}{c\sqrt{\frac{1}{(\Delta x)^2} + \frac{1}{(\Delta y)^2} + \frac{1}{(\Delta z)^2}}} \tag{2.12}$$

2.1.3 Numerical Grid Dispersion

Numerical grid dispersion is a phenomenon caused by the discretization of Maxwell's curl equations in the FDTD method. The phase velocity of the numerical waves propagating through the FDTD grid can differ from the physical phase velocity depending on factors such as grid discretization and direction of propagation through the grid [80]. Numerical dispersion can be a significant source of error in FDTD simulations, especially for large grids. The derivation of an expression for the numerical dispersion error of a plane wave propagating through a two-dimensional FDTD grid is given in Appendix A.

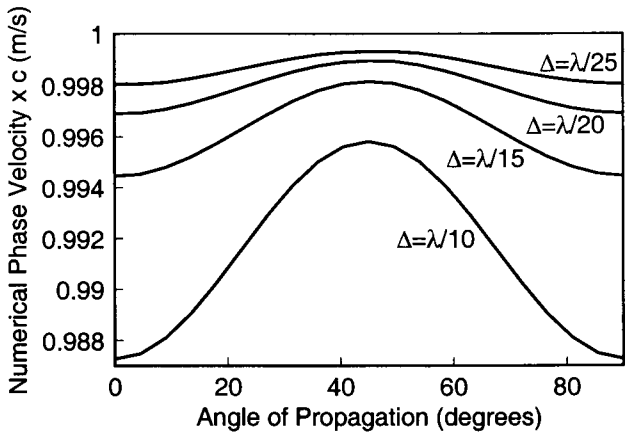

Figure 2.2: Theoretical phase velocity for the FDTD method for various propagation angles in free space. An angle of zero degrees corresponds to the direction of the Cartesian axis. Cell sizes are λ/z.

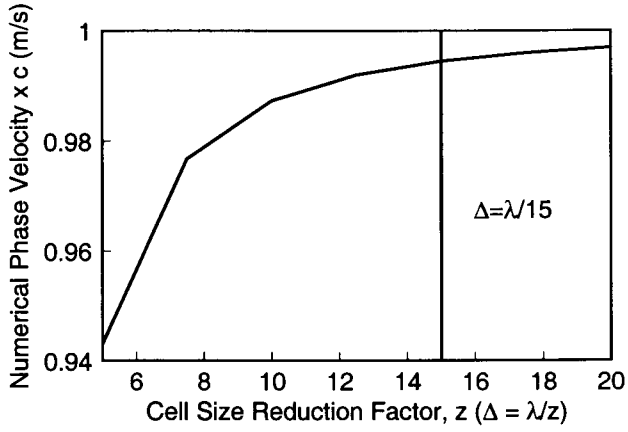

Figure 2.3: Theoretical phase velocity in free space for the FDTD method in the direction of the Cartesian axis for cell sizes of $\Delta = \lambda/z$, where z is the cell size reduction factor.

According to the results of (A.7) and (A.8), the free-space propagation error of the FDTD method is maximum when a plane wave is propagating in the direction of the grid, i. e., in one of the Cartesian axis directions. Figure 2.2 demonstrates this effect, showing the expected numerical phase velocity due to grid dispersion for a plane wave propagating through the FDTD grid at various angles for four different grid cell sizes. A propagation angle of 0° corresponds to the direction of the Cartesian axes. Figure 2.3

shows the decreasing error in the numerical phase velocity at 0° propagation angle for a plane wave propagating through an FDTD grid. From these results, it is apparent that it is necessary to compromise between computational efficiency and the minimization of phase velocity error when implementing the FDTD grid.

A graphical demonstration of numerical grid dispersion is presented in Figure 2.4. A signal with an operating frequency of 900 MHz (a commonly used frequency in wireless PCS applications) has propagated 2.046m ($\approx 6\lambda$) through the FDTD grid in the direction of one Cartesian axis. The FDTD grid cell size is 2.2cm ($\approx \lambda/15$). From Figure 2.3, the expected numerical phase velocity for a wave propagating in the direction of the Cartesian coordinates in a 2-D FDTD grid with cell size $\lambda/15$ is approximately $0.9944c$. Therefore, comparison of the signal which has propagated through the grid with an ideal signal which has propagated this distance with phase velocity of $0.9944c$ will verify the grid dispersion calculation and will thus give an indication of the accuracy of the FDTD implementation.

The first result (solid line) in Figure 2.4 represents the signal which has propagated 2.046 meters in the horizontal plane (i. e., essentially a 2-D case) in the FDTD program utilized throughout this thesis. The second result (dashed line) represents an ideal signal traveling with a phase velocity based on predicted numerical dispersion, $v_p = 0.9944c$. The third case (dotted line) shows, for comparison, an ideal signal with a velocity of propagation equal to the free space value of $c = 3\text{x}10^8\text{m/s}$. In all three cases a Hertzian dipole source is used. Good agreement is seen between the FDTD simulation and the predicted phase velocity of $v_p = 0.9944c$, indicating that the FDTD implementation used in the present work is behaving according to theory.

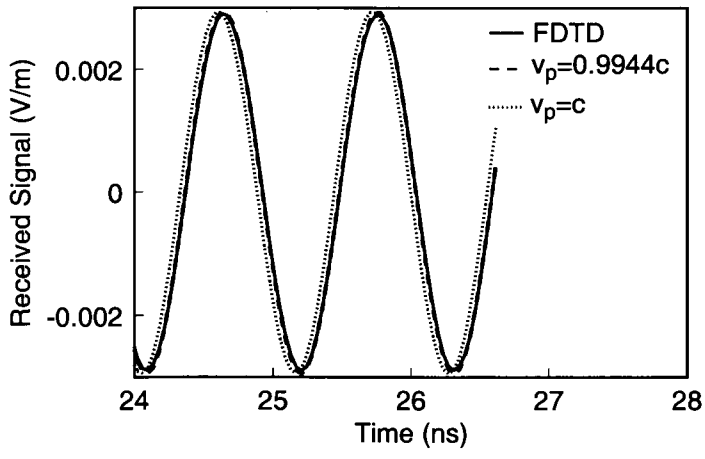

Figure 2.4: A sinusoidal signal which has propagated through the FDTD grid is compared with two ideal signals, one whose phase velocity, $v_p = 0.9944c$, corresponds to the predicted numerical phase velocity, and the other, where $v_p = c$.

2.2 Development of the Kirchhoff Surface Integral Formulation

The Kirchhoff surface integral [30, 31] is one of several near-to-near and near-to-far field transformation techniques (see Section 1.1). These spatial transformation techniques are based on Huygens' principle, which states that each point on an expanding wavefront may act as a new source of radiation.

Spatial transformation techniques allow determination of electromagnetic fields anywhere in a source-free problem space in terms of known field values on a "virtual" surface (see Figure 2.5). Sources, scatterers, and any other material inhomogeneities are specified inside this surface. The transformation enables calculation of radiative fields arising from these sources (or secondary sources) at any analytically specified observation point external to the virtual surface. When combined with the FDTD method, the spatial transformation allows calculation of fields at points external to the FDTD grid and at points located between FDTD grid cell points, as stated earlier.

The Kirchhoff formulation differs from that of other spatial transformation techniques because it is a *scalar* technique, that is, one scalar field quantity is utilized and determined separately in each calculation. For example, E_z at a far-field point is determined only in terms of E_z on the calculation surface

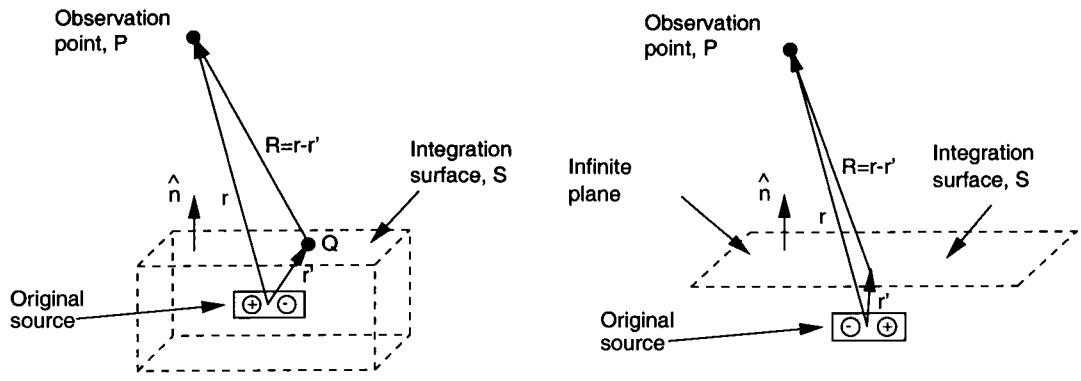

Figure 2.5: Equivalent source representations for the Kirchhoff surface integral. A closed surface or, equivalently, an infinite plane may be used.

The Kirchhoff surface integral may be stated as follows: Given a homogeneous problem space outside a closed surface, S, let $\phi(x,y,z,t)$ be a solution of the wave equation

$$\nabla^2\phi = \frac{1}{c^2}\frac{\partial^2\phi}{\partial t^2} \tag{2.13}$$

whose first and second order partial derivatives are continuous on S, and let P be a point outside S. Then,

$$\phi(P,t) = \frac{1}{4\pi}\iint_{S'}\left\{[\phi]\frac{\partial}{\partial n'}\left(\frac{1}{R}\right) - \frac{1}{cR}\frac{\partial R}{\partial n'}\left[\frac{\partial\phi}{\partial t}\right] - \frac{1}{R}\left[\frac{\partial\phi}{\partial n'}\right]\right\}dS, \tag{2.14}$$

where the prime refers to points on the integration surface. Refer to Figure 2.5 for definition of the remaining terms.

The square brackets indicate retarded time corresponding to the time required for a signal to travel from a point, Q, on the surface to P with speed $c = 1/\sqrt{\mu_0\epsilon_0}$, that is,

$$[\phi] = \phi\left(x',y',z',t - \frac{R_i}{c}\right). \tag{2.15}$$

The first term on the right side of (2.14) will be called the *direct* term, since it is directly proportional to the scalar field. The second and third terms will be called the *time* and *normal* terms, since they are proportional to the time and normal derivatives of the scalar field, respectively. Note that the *direct* term decreases as $1/R^2$ (once the derivative $\partial/\partial n'(1/R)$ is taken), while the *time* and *normal* terms decrease as $1/R$. The derivation of the Kirchhoff surface integral, based on Kirchhoff's original paper in 1883 (published four years before his death), is presented in Appendix B.

2.2.1 Implementation of the Kirchhoff Surface Integral

The Kirchhoff surface integral formulation used in the present work is designed for implementation on a digital computer. This means that the development of a discretized version of the integral is a primary consideration in the implementation of the spatial transformation. As discussed in [21], the discretized Kirchhoff surface integral may be readily combined with a Yee-cell-based FDTD code (described in Section 2.1). For efficient combination with the FDTD method, similar levels of discretization and the use of similar

indexing techniques are desirable features. These issues, among others, are addressed in the following discussion.

A primary aspect of implementation of the Kirchhoff surface integral is determination of the fields at the surface of integration. These surface fields can be found using a variety of computational methods, including the FDTD technique, the MoM, and, in a limited number of cases, analytical solutions. The Kirchhoff surface integral utilized in the present work has been implemented in two versions. One uses analytic equations for the surface fields, and was written for use with the Matlab [81] software. Because analytic expressions are used, this method is computationally very efficient, although the use of a higher-level programming language somewhat slows the calculation time. The second implementation utilizes a computer program incorporating the FDTD method previously developed by researchers at Oregon State University [82]. This FDTD program is extended in the present work to include the Kirchhoff surface integral formulation. A source term specified in the FDTD code generates the fields at the integration surface. Each of the two versions follows the same basic procedures for determining the components of the integral and the integration. Because of the versatility of the combined FDTD/Kirchhoff integral formulation, it is used extensively throughout the thesis. Therefore, its implementation is discussed in detail here.

In the discretized version of the Kirchhoff surface integral, the integration surface for a given field component is considered to lie midway between two of the component's discrete spatial locations, e. g., FDTD grid points, designated ϕ_{in} and ϕ_{out} in Figure 2.6, where ϕ may refer to any of the six field components in Cartesian coordinates. Using difference equations, the fields at the integration surface may be efficiently calculated from quantities already computed in the FDTD code. For example, the surface field may be given by

$$\phi_{i,j,k} = \frac{\phi_{in} + \phi_{out}}{2} \tag{2.16}$$

Difference equations are also used to find the other terms in the integral (2.14) efficiently. For example, the normal derivative term may be given by

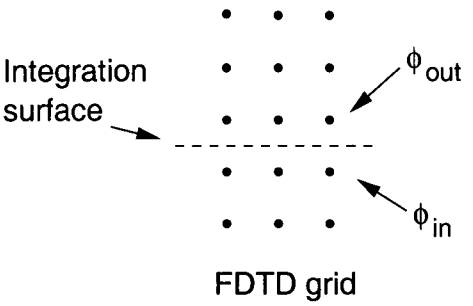

Figure 2.6: Implementation of the integration surface in the FDTD code. Here, ϕ may refer to any of the six field components in Cartesian coordinates.

$$\frac{\partial \phi_{i,j,k}}{\partial n} = \frac{\phi_{in} + \phi_{out}}{\Delta} \tag{2.17}$$

where Δ refers to the grid cell size between ϕ_{in} and ϕ_{out}. The time derivative term may be found in a similar manner.

The discretized version of the surface integration may be considered as a time weighted summation. Time is discretized as $n\Delta t$, with n corresponding to the time step and Δt to the time increment. The delay time between surface element $\Delta s_{i,j,k}$ and the observation point is given by $\tau^d_{i,j,k} = R_{i,j,k}/c$, where the velocity of propagation is the speed of light, c. (See Figure 2.7.) This delay time is used to assign the evolving surface field terms to the proper elements of the *delayed field vector*. The delayed field vector contains the final result of the integration, i. e., the time evolution of the spatially-transformed field at the observation point. The contribution from an individual surface element to the final result is incorporated into the delayed field vector sequentially in time. However, since the time delays, $\tau^d_{i,j,k}$, are not uniform, the initial entry into the delayed field vector will generally be different for each surface element. For the case shown in Figure 2.7, for example, the surface fields generated by the dipole source will be equal in both amplitude and arrival time at surface elements $\Delta s_{i,j,k}$ and $\Delta s_{i,j,-k}$. However, since $R_{i,j,k}$ is greater than $R_{i,j,-k}$, the contribution to the final result from $\Delta s_{i,j,k}$ will be incorporated into the delayed field at a later time step than the contribution from element $\Delta s_{i,j,-k}$.

Because the delay time from each surface point to the observation point rarely falls as an integer multiple of Δt, time interpolation is used. A simple linear interpolation

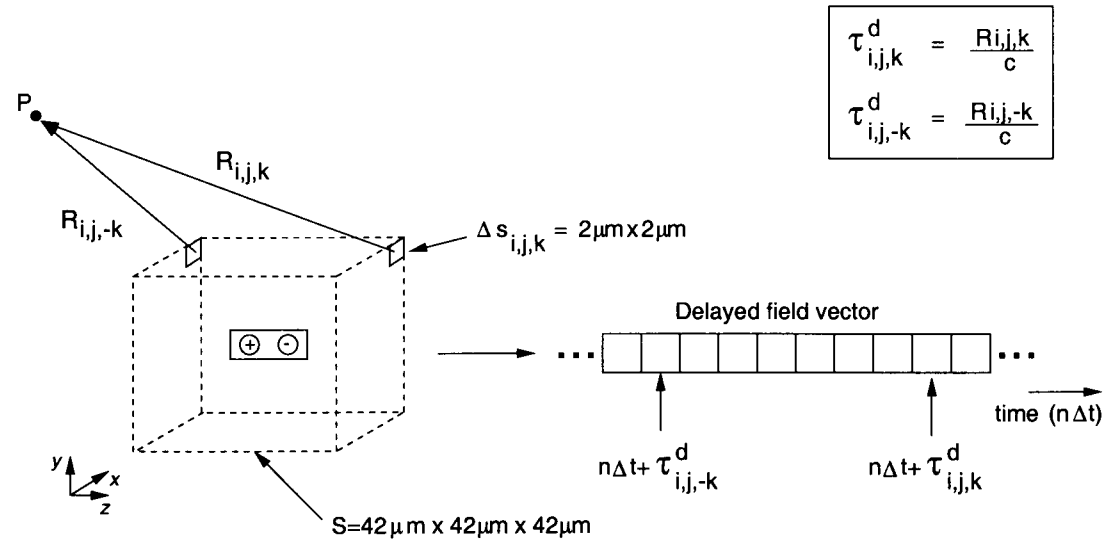

Figure 2.7: The evolution of the delayed field vector at time step n. The schematic shows the delay time from each surface element to the observation point.

scheme is used for the direct and normal derivative terms, and second order Lagrangian interpolation is used to maintain second order accuracy of the time derivative [21]. Thus, the expressions for the *direct*, *time*, and *normal* terms calculated with respect to retarded time, $\tau = n\Delta t + \tau^d_{i,j,k}$ (see (2.14)), can be given by

$$\left.\begin{aligned}
&[\phi_{i,j,k}] = (1-p)\,\phi^n_{i,j,k} + p\,\phi^{n+1}_{i,j,k} && \text{Direct}\\
&\left[\frac{\partial \phi_{i,j,k}}{\partial t}\right] = \frac{1}{\Delta t}\left\{\left(p-\tfrac{1}{2}\right)\phi^{n-1}_{i,j,k} - 2\,p\,\phi^n_{i,j,k} + \left(p+\tfrac{1}{2}\right)\phi^{n+1}_{i,j,k}\right\} && \text{Time}\\
&\left[\frac{\partial \phi_{i,j,k}}{\partial n}\right] = (1-p)\frac{\partial \phi^n_{i,j,k}}{\partial n} + p\frac{\partial \phi^{n+1}_{i,j,k}}{\partial n} && \text{Normal}
\end{aligned}\right\} \qquad (2.18)$$

where n is the integer part and p is the fractional part of $\tau/\Delta t$, the term $\phi_{i,j,k}$ is the surface field given by (2.16), and the term $\partial\phi_{i,j,k}/\partial n$ is the normal derivative given by (2.17).

In this formulation, the terms $\frac{\partial R}{\partial n}$ and $\frac{\partial}{\partial n}\left(\frac{1}{R}\right)$ in (2.14) are equivalent to $(\hat{n}\cdot\hat{a}_R)$ and $\frac{-(\hat{n}\cdot\hat{a}_R)}{R^2}$, respectively, where $\hat{n}$ is the unit vector directed outward from and normal to the

integration surface, and $\hat{a}_R$ is the unit vector in the direction of $\vec{R}$. The subscripts i, j, k have been omitted for clarity.

With the use of these expressions for the individual terms of the Kirchhoff surface integral and the time-weighted surface integration method described above, the combined FDTD/Kirchhoff spatial transformation computational technique is complete. Details of the computational algorithm used in the present work can be found in Appendix C.

2.2.2 Validation of the Technique and Evolution of the Delayed Field Vector

To validate the accuracy of the FDTD/Kirchhoff integral formulation and to illustrate the evolution of the delayed field vector, an example is presented comparing the numerical results to the exact solution. Again refer to Figure 2.7. The source is a Hertzian dipole excited by a Gaussian current pulse

$$p(n\Delta t) = e^{\left(\frac{n\Delta t - t_0}{\tau}\right)^2} \tag{2.19}$$

with pulse width $\tau=\beta\Delta t$, and delay time $t_0=4\tau$. This choice of t_0 sets the starting value of the pulse at $\exp(-16) = -140$ dB in order to minimize noise in the FDTD caused by the turn-on characteristics of the source [29]. With β=32 and $\Delta x=\Delta y=\Delta z=2\mu$m, the time step, Δt, is taken as Δt=3.47 fs, which is 0.9 times the Courant stability condition for the FDTD technique. The E_z field component is calculated at observation point P, located 60 μm and 45° off the axis of a z-oriented dipole.

The exact solution for the electric field from a Hertzian dipole source may be found using the equations for an infinitesimal dipole [7, 83]:

$$\begin{aligned}
&\vec{E}(R,t) = \\
&\quad \hat{a}_R \left[\frac{2dl\cos\theta}{4\pi\epsilon_0} \left(\int_t \frac{\int_v J_{v'}\left(\tau - \frac{R}{c}\right) dv'}{R^3} d\tau + \frac{\int_v J_{v'}\left(t - \frac{R}{c}\right) dv'}{cR^2} \right) \right] \\
&\quad -\hat{a}_\theta \left[\frac{dl\sin\theta}{4\pi\epsilon_0} \left(\int_t \frac{\int_v J_{v'}\left(\tau - \frac{R}{c}\right) dv'}{R^3} d\tau - \frac{\int_v J_{v'}\left(t - \frac{R}{c}\right) dv'}{cR^2} \right.\right. \\
&\qquad \left.\left. + \frac{\frac{\partial}{\partial t}\int_v J_{v'}\left(t - \frac{R}{c}\right) dv'}{c^2 R} \right) \right]
\end{aligned} \tag{2.20}$$

Here R is the distance from the dipole to the observation point, dl is the length of the dipole, J_v is the volume current density induced by the dipole, and θ is measured off the dipole axis. The permittivity and velocity of propagation corresponding to free space are given by ϵ_0 and c, respectively. Note that the subscript R corresponding to the unit vector a_R indicates the radial direction in spherical coordinates rather than the distance R.

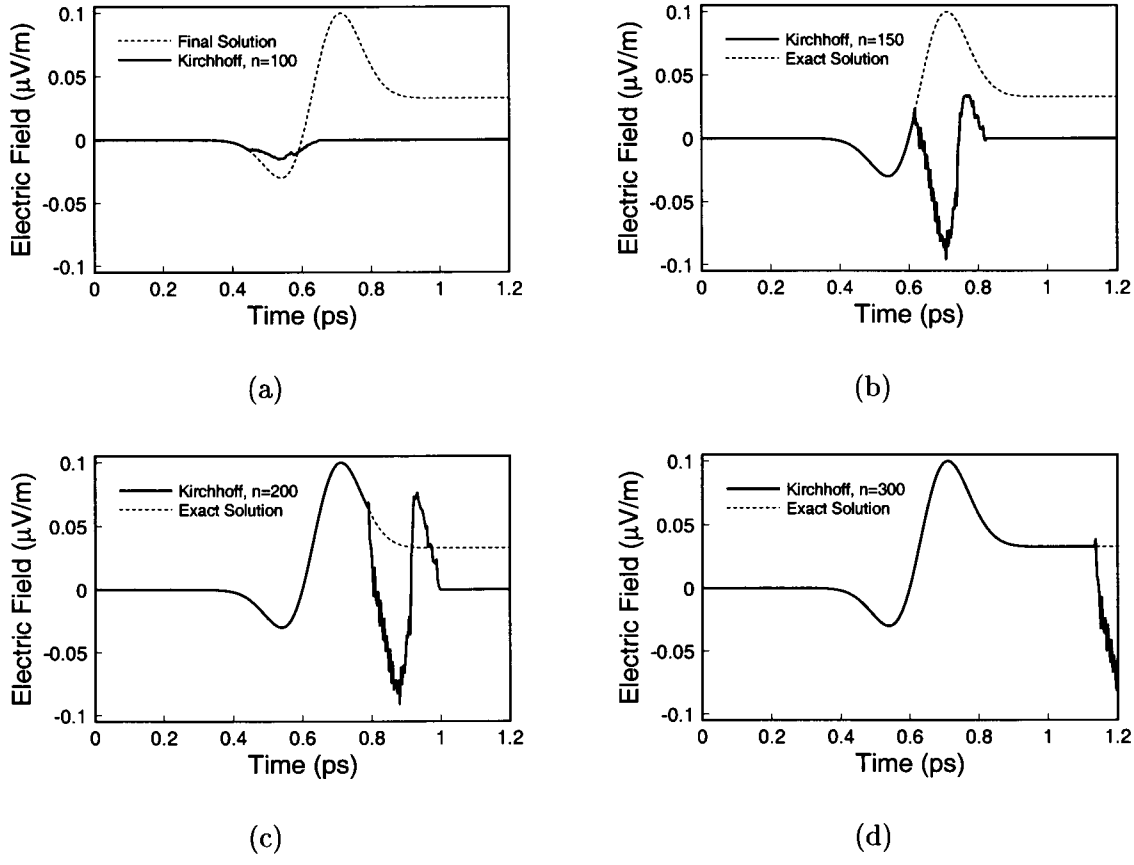

Figure 2.8: The evolution of the delayed field vector at time steps (a) $n = 100$, (b) $n = 150$, (c) $n = 200$, and (d) $n = 300$ using the Kirchhoff surface integral formulation.

For the FDTD method, the Hertzian dipole is approximated using the technique described in [84], that is, the current distribution is assumed constant over the volume of one grid cell. The field at the integration surface is found using the FDTD technique. To

implement the Kirchhoff transformation, at time step n, the elements of the delayed field vector (found using (2.14)) accumulate according to $n\Delta t + \tau^d_{i,j,k}$. In the evolution of the delayed field vector, each surface element may be considered as a secondary source [1].

As can be seen in Figure 2.8, agreement between the exact solution and the combined FDTD/Kirchhoff technique is excellent. Even for simulations in the near field, such as the present example, the additional calculation time required by the Kirchhoff technique is often offset by the propagation time through the FDTD grid required when the FDTD method is used alone. Additionally, use of the FDTD/Kirchhoff technique reduces the time dispersion associated with the FDTD method [80] since the FDTD calculation only extends spatially from the original dipole source to the surface of integration.

2.2.3 The Components of the Kirchhoff Surface Integral

In the present work, the combined FDTD/Kirchhoff technique is used to simulate the fields arising from non-time-harmonic sources of radiation. It may not be readily apparent how the correct solution is obtained when contributions from the surface integral may arrive at the observation point at times *later* than the duration of the pulse. The way in which the various components of the integral interact can resolve its apparent nonphysicality. Therefore, in this section two aspects of the evolution of the integral are described – how contributions from the various regions of the integration surface combine, and how contributions from the three terms of the integral combine. Other researchers have utilized the Kirchhoff surface integral formulation in the time and frequency domains [21], [33]–[35]. However, a discussion of the relationships among the various components of the integral has not, to the author's knowledge, been presented.

In the first case, the contribution from each side of a closed rectangular integration surface similar to the schematic shown in Figure 2.7 is considered. A scalar (non-

[1] Because the Kirchhoff surface integral is a scalar technique, each surface element may not be considered as a true "source" of electromagnetic radiation since that would imply a vector quantity. As stated in *Huygens' Principle* by Baker and Copson [31], p.103, "...the secondary disturbances obtained in this way are not solutions to Maxwell's equations...[E]ach secondary source in Huygens' principle ought to give rise to an electromagnetic wave." However, the concept of a secondary source accurately describes the time delay.

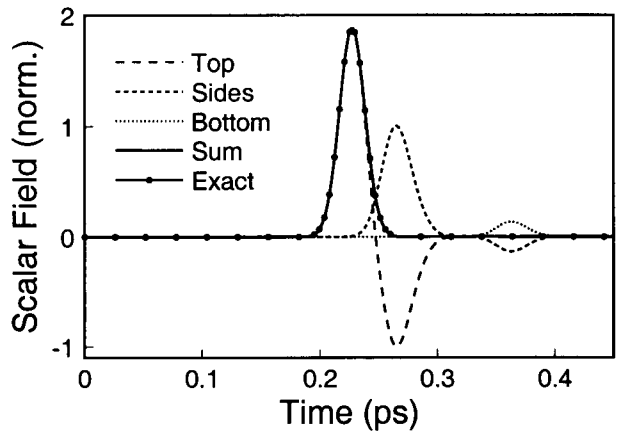

Figure 2.9: The time evolution of the contribution from each region of the integration surface. The contributions are summed to yield the complete result of the Kirchhoff surface integral calculation.

electromagnetic) source is used to present clearly the interrelationships between components of the integral. Excitation is a Gaussian pulse (2.19) with $\beta = 18$, $\tau = 154$ ps, and $t_0 = 616$ ps. The exact equations for fields at the integration surface from the scalar source were implemented in Matlab [81] with Δx=Δy=Δz=0.75μm and $\Delta t = 86.7$ fs. The surface of integration is a cube with 30.75μm side dimensions, and the observation point is located 50μm directly above the source at the point (0, 50μm, 0).

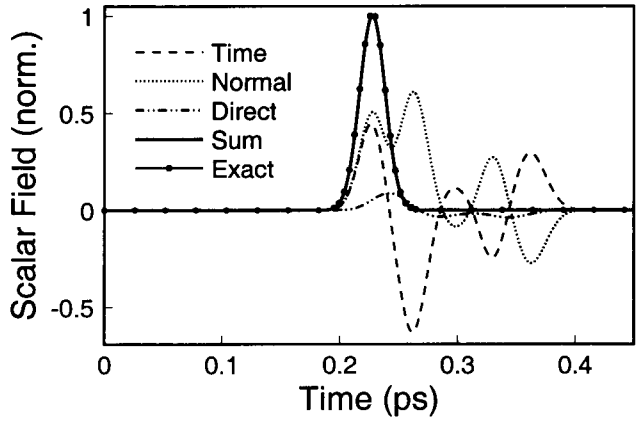

Figure 2.10: The time evolution of the *direct*, *time*, and *normal* terms of the Kirchhoff surface integral.

Figure 2.9 shows that the contribution from the top surface is exact until the time the evolving surface field reaches the edge of the top surface (at approximately 0.23 ps). From this time on, contributions from the top and four sides must be considered collectively. Because the excitation is scalar and centered in the box, the contribution from each of the four sides is equal. Similarly, at around 0.33 ps the contribution from the bottom surface must also be included. Note that components of the received signal have significant value long after the duration of the original pulse.

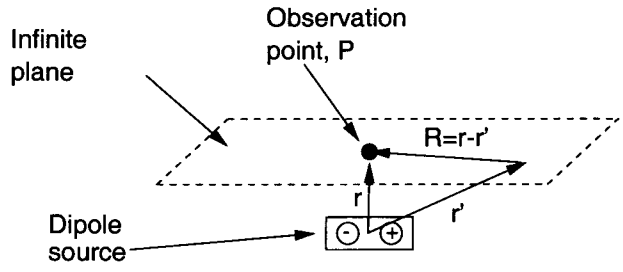

Figure 2.11: Structure used for the single infinite surface example.

The individual contributions from the *direct*, *time*, and *normal* terms of the Kirchhoff surface integral (2.14) are next considered. Using the same structure and excitation as in the previous example, the time evolution of each of the three components is displayed in Figure 2.10. Because the *direct* term decreases as $1/R^2$, its contribution to the integral is minimal except in the very near field. The *time* and *normal* terms combine to form the received pulse and cancel at times greater than the received pulse duration. Again, it may be seen that the fields generated at times that are greater than the pulse duration effectively cancel, and thus the correct solution is produced.

In a second example, the results of De Moerloose and De Zutter [21] are reproduced using an infinite plane as the integration surface. This integration surface is shown

schematically in Figure 2.11. The infinite plane formulation is valid as long as the integration surface is large enough to contain the surface field for the duration of the simulation, as is here demonstrated by comparison to analytical results. The authors of [21] utilize a closed integration surface similar to those shown in prior examples. The present example additionally demonstrates the equality of the *normal* term and the sum of the *time* and *direct* terms for the case of symmetric source and observation points relative to the integration surface.

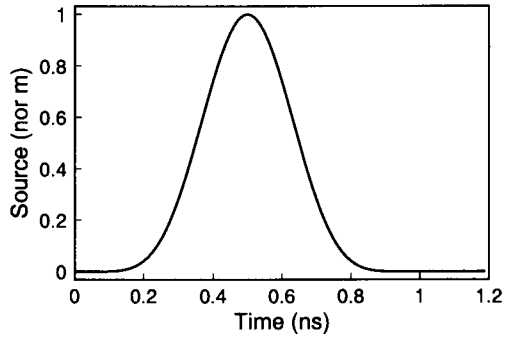

Figure 2.12: Source excitation used for the infinite plane integration surface example.

The observation point, P, is located half a grid cell above the integration surface. The spatial transformation is generally more difficult when the observation point is extremely close to the integration surface because of the need for more precise determination of angles and distances.

In this example, the source is a z-directed dipole whose excitation is described by the time variation of the dipole moment (Figure 2.12). The time variation of the dipole moment is given by [76]:

$$f(t) = \begin{cases} 10 - 15\cos\omega_1 t + 6\cos\omega_2 t - \cos\omega_3 t, & t \leq \tau \\ 0 \qquad\qquad\qquad\qquad\qquad\qquad\qquad\quad , & t > \tau \end{cases} \tag{2.21}$$

where

$$\omega_n = \frac{2\pi n}{\tau}, \qquad \tau = 1 \text{ ns} \tag{2.22}$$

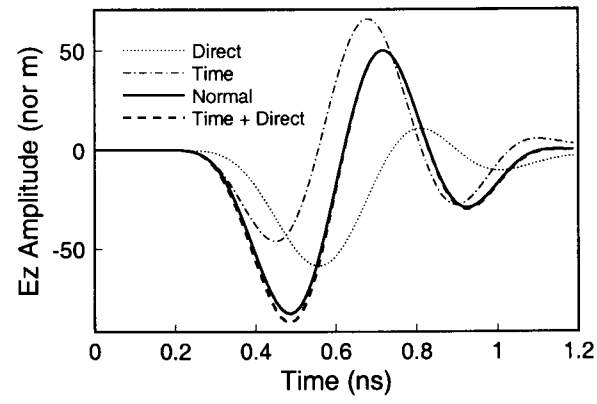

(a)

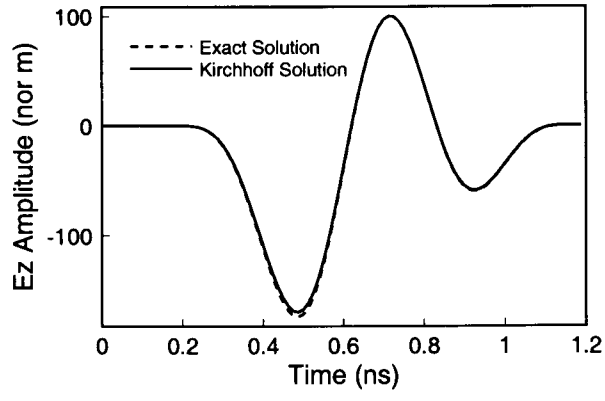

(b)

Figure 2.13: (a) Comparison of *direct, time, and normal* terms, and the sum of the *direct* and *time* terms, showing the equivalence of the *normal* and sum terms. (b) Comparison of the solution found using the Kirchhoff surface integral formulation and the exact solution.

Figure 2.13(a) shows the individual components of the integral as well as the sum of the *direct* and *time* components. Note that the sum of the *direct* and *time* terms is approximately equal to the *normal* term. This condition is true for symmetric cases, where the observation point is located directly above the center of the integration surface (an effect seen also in Figure 2.10). Calculations made near the integration surface are more difficult than are calculations at distant observation points because accurate integration over each grid space becomes more critical. (Note the discrepancy between the sum term and the *normal* term.) Additionally, the source data are precalculated in this example and

the surface fields are found using linear interpolation between pre-calculated data points, adding some error.

Figure 2.13(b) compares the Kirchhoff transformation results with the exact solution. The exact calculation was found using a Hertzian dipole source with dipole moment excitation given by (2.21). Note that the sum of all terms of the Kirchhoff surface integral do not add to give the precise solution, a manifestation of the effect shown in Figure 2.13(a). However, the results shown in Figure 2.13(b) are similar to those found in Figure 6 of [21].

2.3 Conclusion

In this chapter, the incorporation of a discretized version of the Kirchhoff surface integral into the FDTD technique has been presented. The basic FDTD equations were first reviewed and implementation considerations were discussed. A demonstration of numerical grid dispersion, an artifact inherent to the FDTD method, was presented, serving to illustrate the effect and to validate the FDTD implementation used in this thesis. The Kirchhoff surface integral, a spatial transformation technique, was next presented. The development of a discretized expression for the Kirchhoff surface integral was discussed. Various techniques for obtaining the fields at the integration surface were included, as well as the representation of the surface integration routine as a time-weighted summation. Results found using the combined FDTD/Kirchhoff technique and an exact calculation for the field arising from an ideal Hertzian dipole were compared, and agreement was shown to be excellent. To illustrate how the various components of the integral combine to provide the final solution, a demonstration was given using a pulsed scalar source. It was shown that significant contributions from the integral may arrive at the observation point at times later than the duration of the pulse, but that these contributions always combine to provide the correct final solution. Finally, it was demonstrated that a single infinite plane may replace the standard closed surface of integration.

In the following two chapters, the combined FDTD/Kirchhoff technique is applied to improve modeling of radiative systems in two different areas: ultrafast electronic and wireless communication systems. It is shown that this versatile technique can offer improved

efficiency and accuracy when compared to the standard FDTD method. Additionally, because of its high degree of accuracy, it can also be used as a standard for comparison in the development of other highly efficient computational techniques for modeling radiative systems.

3. MODELING TERAHERTZ RADIATION FROM ULTRAFAST ELECTRONIC STRUCTURES

Technology for the fabrication of electronic devices has greatly improved in recent years. These improvements have enabled reduction in device feature size, which, in turn, has led to large-scale integration of electronic components with reduced inter-device transit times, as well as development of high speed devices which utilize traveling-wave and/or guided-wave effects. With incorporation of these advances has come the possibility of increasing device frequency of operation beyond the microwave region into the millimeter-wave and low infrared (terahertz) regions. The resulting *ultrafast* devices have a number of uses, for example, as modulators [2, 3], in switching applications [11, 12, 85], and in material characterization [86, 87].

Characterization of radiative effects is particularly important in the design and analysis of ultrafast electronic systems. Relative to the small wavelength of excitation, the radiative source is often spatially distributed. That is, radiation may originate from an entire component or region of a component. Therefore, there is a high probability of parasitic radiation and resulting crosstalk, which should be accounted for in the design stages of ultrafast electronic devices. Additionally, some ultrafast systems, such as the photoconducting structure discussed in this chapter, utilize radiative coupling exclusively between system components. Accurate representation of the radiative fields in these cases is essential for system design and development.

However, radiation from ultrafast electronic systems can be difficult to characterize for a variety of reasons. The distributed nature of the source often makes the use of many analytic techniques infeasible. A variety of material parameters may be involved as well, significantly increasing the complexity of the characterization. Frequency domain techniques, such as the method of moments (MoM), generally are not capable of efficiently modeling the broadband radiation often associated with ultrafast electronic structures.

The combined FDTD/Kirchhoff technique is a natural choice for analyzing radiation from a wide array of ultrafast electronic structures, since, as discussed in Chapter 2, it is

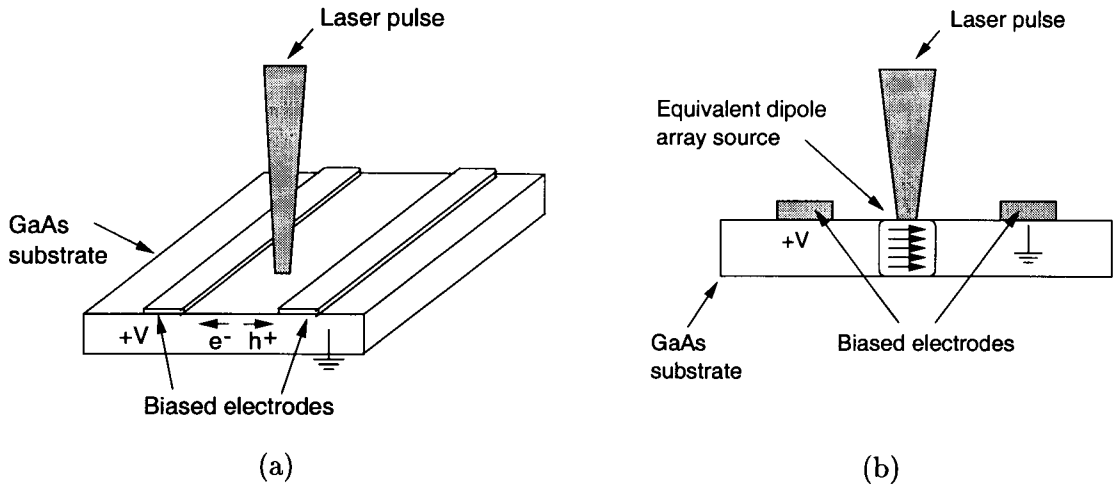

Figure 3.1: Typical photoconducting structure for an electro-optic sampling experiment. A sub-picosecond laser pulse is incident on a GaAs substrate with two biased metal electrodes. (a) Photogenerated electron-hole pairs migrate toward the biased electrodes. (b) Side view of the same structure showing the uniformly distributed source of radiation.

capable of addressing all of the issues mentioned above. Additionally, this technique allows determination of radiative fields at large distances from the source.

In this chapter, analysis of a photoconducting structure (Figure 3.1) is carried out as an example of the use of the FDTD/Kirchhoff technique for ultrafast electronic device characterization. First, a description of the photoconducting structure is given, including the physical system and the source of radiation. Then, a commonly used modeling technique for characterizing the radiation is presented. This model, the *far-field approximation*, is based on the derivative of the source current and is limited to determination of the far-field radiation. Additionally, because it is based on an analytic expression derived for free-space propagation, material parameters cannot be included. The far-field approximation is improved upon with the use of the FDTD/Kirchhoff technique. Utilizing this technique, homogeneity of the problem space is not required and the radiative fields may be determined in either the near or far field. The development of this technique is given in two steps: first, inhomogeneous material parameters are introduced into the FDTD simulation and their effects on the radiative fields are demonstrated. Then, results are presented utilizing the FDTD/Kirchhoff technique in the characterization of radiation from the full

photoconducting structure. Simulation results show a significantly more accurate portrait of the far-field radiation compared to the standard far-field approximation [88, 89].

3.1 The Photoconducting Structure

As the name implies, photoconducting structures utilize optically (photo-) generated carriers in electronic (conducting) device operation. The movement of these carriers gives rise to electromagnetic radiative fields, which may have frequency content into the terahertz range. Many ultrafast electronic systems that utilize photoconducting structures rely on the coupling of these fields between the source, the electronic device, and/or the detector. In some ultrafast electronic applications, however, the generation of radiative fields is an unwanted effect. In either case, accurate characterization of the radiative fields is important.

The utilization of radiative field coupling in photoconducting structures is called *electro-optic (EO) sampling* [86, 90, 91, 92]. The process of EO sampling includes: photo-generation of carriers in the device from an external laser source; carrier/device interaction resulting in generation of an electric field; and subsequent photodetection of the electric field at a point removed from the photoconducting structure. EO sampling provides a method of in situ testing and excitation of devices. It provides spatial resolution in the micron range without the need for physical contact. Applications which utilize EO sampling include high-speed switching [11, 12, 93, 94], photoconducting dipole antennas [13, 14, 95, 96, 97], and terahertz spectroscopy for material characterization [87, 98, 99, 100].

A general photoconducting structure is shown in Figures 3.1(a) and (b). Two metal electrodes lie parallel to each other on a gallium arsenide (GaAs) substrate. A sub-picosecond laser pulse is incident on the substrate, creating electron-hole pairs. Application of a bias voltage to the electrodes accelerates the electrons and holes in opposite directions, as shown in Figure 3.1(a). This produces a time-varying current density, which can be modeled as a uniformly-distributed dipole source [66, 88], as indicated in Figure 3.1(b). The orientation of the dipole is parallel to the substrate surface and transverse to the biased electrodes. This time-varying source of radiation has a rise time on the order

of a few hundred femtoseconds. Once the excitation is removed, the biased electrodes continue to attract the electrons and holes. Therefore recombination occurs (and the resulting electric field is generated), over a time-scale much longer than the simulation time.

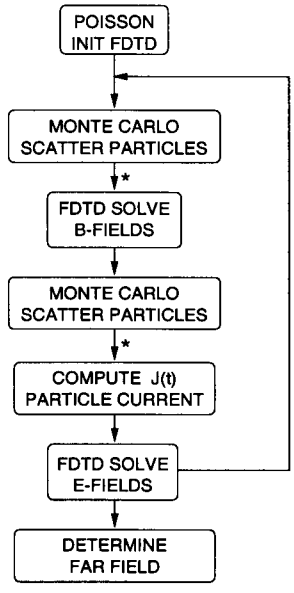

Figure 3.2: Computer algorithm used in the PMC-3D.

To determine accurately the current density generated in the photoconducting structure, a simulation tool developed by researchers at Oregon State University [101] is utilized. The tool, called the PMC-3D, couples a Monte Carlo particle simulator [2] to either a Poisson solver or an FDTD electromagnetic field solver to determine device characteristics such as potential, particle distribution, and current density anywhere in the computational domain. In the present case, an FDTD solver rather than a Poisson solver is used, enabling determination of the electromagnetic (EM) fields throughout the simulation space. The

[2]The Monte Carlo particle simulator allows stochastic solution of the Boltzmann transport equation for particle motion. Particle motion is modeled as a series of free flights subject to magnetic and electric forces. Motion is terminated by instantaneous, random scattering events. Random scattering times are generated using a random number generator and the calculated quantum mechanical scattering cross-section. Important scattering mechanisms for the three lowest energy bands of GaAs are included in the model.

Monte Carlo simulator and the FDTD solver are coupled together in a leap-frog manner, allowing updates of both the particle distribution and the EM fields at each time step. Figure 3.2 shows the computer algorithm for this numerical procedure.

Before time stepping commences, each grid cell in the computational domain is initialized using a Poisson solver. At each time step, the Monte Carlo routine first calculates the particle motion, and then the magnetic fields are updated by the FDTD routine. The effects of the magnetic fields are next incorporated into a second particle motion calculation. At this point, the volume particle current density, $J_v(t)$, is calculated, based on the carrier distributions in the GaAs substrate. The particle current density, which is the source of the radiative fields, is next incorporated into the FDTD routine for calculation of the electric fields. When the time stepping has been completed, the far-field radiation is calculated using either the far-field approximation discussed in the next section or the FDTD/Kirchhoff spatial transformation. The PMC-3D has been implemented on both standard single processor workstations and on an n-cube parallel processor supercomputer. The asterisks in Figure 3.2 indicate processor information exchange in the parallel implementation of the PMC-3D.

3.2 Far-Field Approximation Based on the Time Derivative

The far-field approximation has been used for many years by engineers to describe the electromagnetic fields arising from antennas in free space [102, 103]. It gives very accurate results for cases where the field may be described by an analytic expression and the where the observation point is sufficiently far from the source. For example, to approximate the far-field radiation from an ideal dipole, only terms in dipole equations (2.20) which decrease as $1/R$ are retained. Then, the electric field is given by:

$$E_\theta(R,t) = \frac{dl \sin\theta}{4\pi\epsilon_0 R c^2} \frac{\partial}{\partial t} \iiint_V J'_V dV' \tag{3.1}$$

See page 20 for a definition of terms. (3.1) states that the far-field radiation is proportional to the time derivative of the excitation. This expression has been used to approximate the far-field radiation arising from photoconducting antennas and arrays [13, 14, 66].

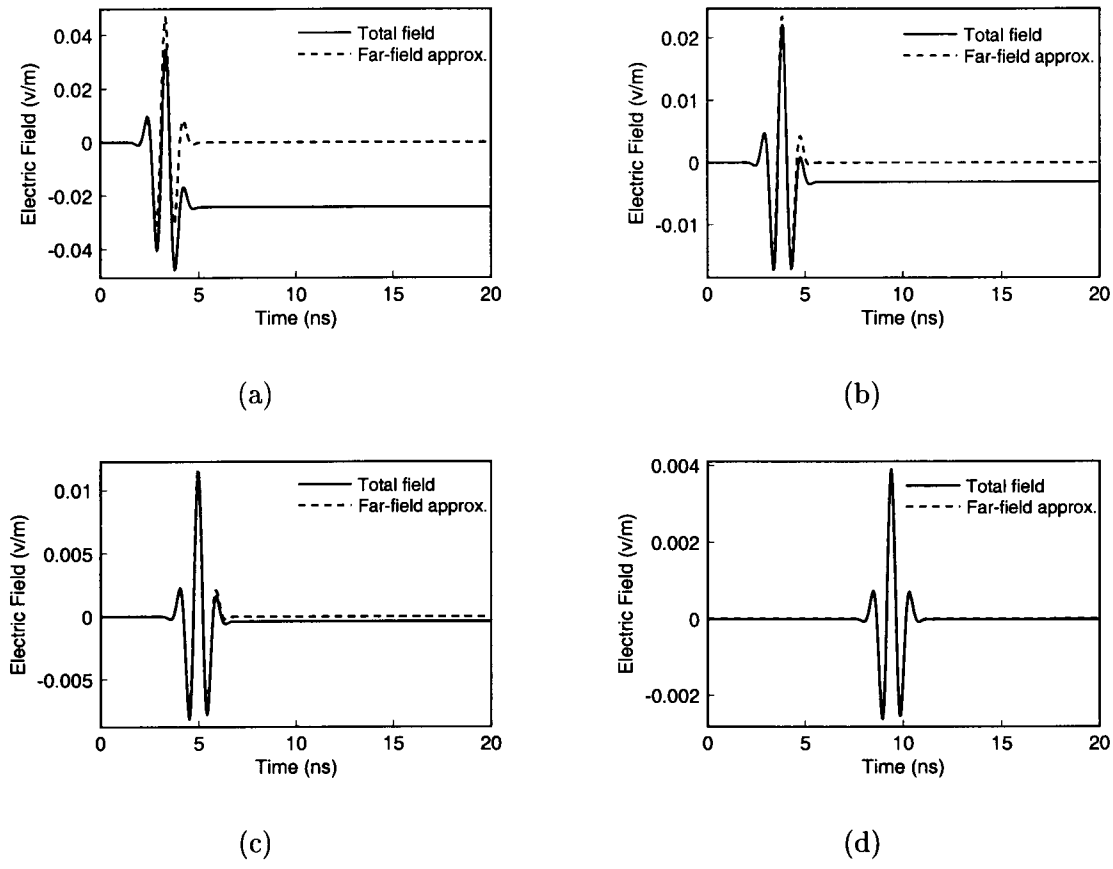

Figure 3.3: Comparison of the total field and the far-field approximation for a pulse-modulated ideal dipole source in free space. (a) $R = 0.5\lambda$, (b) $R = 1\lambda$, (c) $R = 2\lambda$, and (d) $R = 6\lambda$, where R is the distance from the source.

The far-field approximation is valid several wavelengths from the source. For example, refer to Figure 3.3, which shows the electric field arising from a Gaussian-pulse-modulated ideal dipole source in free space. The solid line shows the field utilizing the full set of dipole equations (2.20), and the dashed line shows the far-field approximation. Approximately 6λ from the source, the two curves are almost indistinguishable.

In a typical PMC-3D simulation of the photoconducting structure, it is assumed that the laser pulse has a Gaussian wavefront with a beam radius standard deviation of 2μm and a Gaussian-distributed energy variation between 1.42 eV and 1.62 eV (larger than the bandgap of GaAs). The laser pulse duration is approximately 20 fs. Because the source distribution is spatially so small with respect to the physical structure, it is approximated

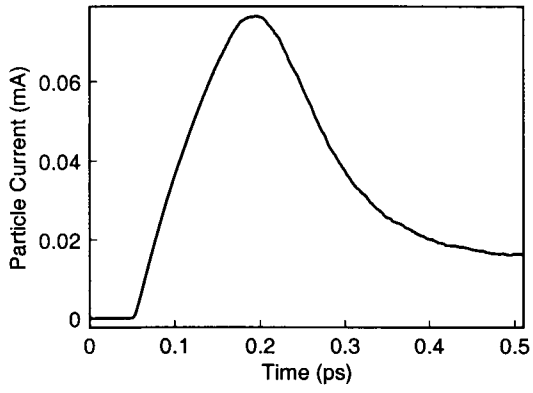

Figure 3.4: Typical current pulse generated in the electro-optic sampling experiment.

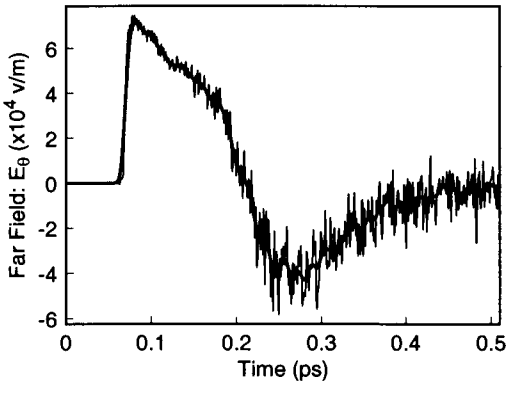

Figure 3.5: Two smoothed versions of the derivative of the current pulse shown in Figure 3.4. The thicker line represents the case with more smoothing.

as an ideal dipole. The excitation of the ideal dipole is a current pulse found by integration of the current density throughout the GaAs substrate. Figure 3.4 shows an example of the current pulse generated with a bias of 40 volts on the metal electrodes and an injection rate of 1e15/cm^3.

Figure 3.5 shows two numerically smoothed versions of the derivative of the pulse in Figure 3.4, representing the far-field radiation over time. Smoothing is necessary because numerical implementation of time differentiation emphasizes the high frequency noise components. Smoothing is accomplished using a moving average filter. Use of the far-field approximation, (3.1), assumes a dipole source of negligible length and free space propaga-

tion, and also neglects the effects of the GaAs substrate and metal electrodes. How close this representation is to a more physical one incorporating material parameters depends on several factors, including the duration of the pulse relative to the transit time through the substrate, the spacing of the metal electrodes, and the observation angle. For example, Figure 3.5 compares well to measured results such as [91], but may not be accurate enough when the pulse duration of the excitation is shorter. An indication of the effects of the material parameters for the present case may be found by looking at the near-field radiation.

Figures 3.6(a) and 3.7(a) show the near-field radiation along a surface above and parallel to the GaAs substrate of the structure shown in Figure 3.1. These fields are calculated using the PMC-3D, with the dipole excitation given in Figure 3.4. Figures 3.6(b) and 3.7(b) show the fields from an ideal dipole for comparison. The effects of the various material parameters in the simulation space may be seen clearly in Figure 3.7(a). The GaAs/air interface causes some variation in the field distribution near the center of the surface. The effects of the interface are accounted for in the next section.

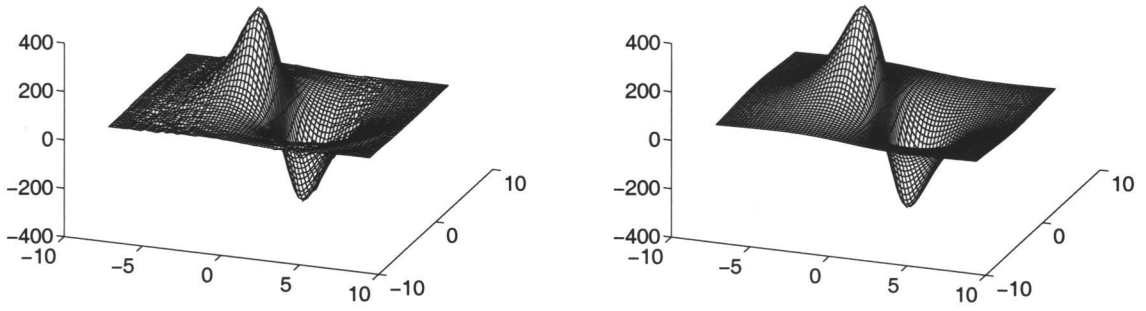

(a) (b)

Figure 3.6: E_R: (a) Near-field radiation from the photo-conducting structure found using FDTD. (b) Near-field radiation from an ideal Hertzian dipole.

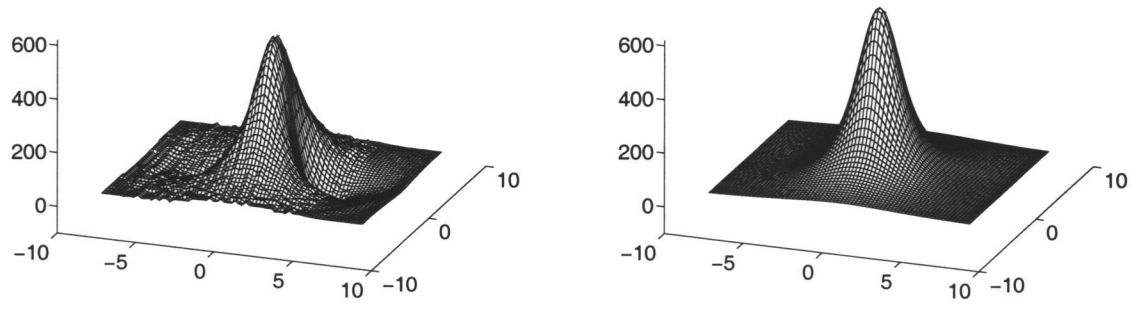

(a) (b)

Figure 3.7: E_θ: (a) Near-field radiation from the photo-conducting structure found using FDTD. (b) Near-field radiation from an ideal Hertzian dipole.

3.3 Inclusion of Inhomogeneous Material Parameters

In the following section, the effects of the inhomogeneous material parameters on the radiation characteristics are addressed. The FDTD/Kirchhoff method is first applied to radiation from a GaAs substrate only. Then, analysis of the full photoconducting system is considered.

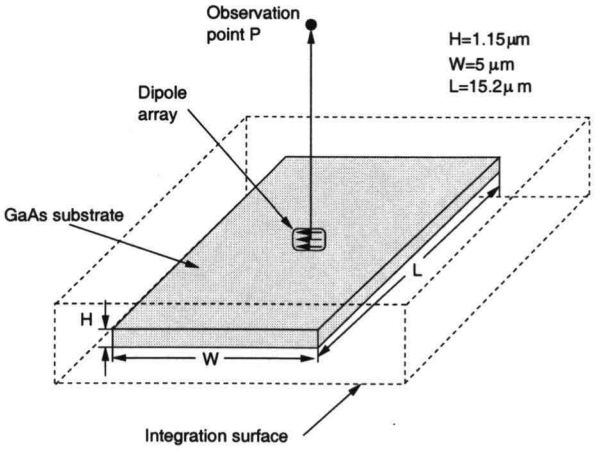

Figure 3.8: Structure used to determine the effects of including inhomogeneous material parameters in the simulation. The integration surface is located external to the inhomogeneous problem space.

The extent to which inhomogeneous material parameters significantly alter results depends on several factors, including the temporal characteristics of the excitation relative to the dimensions of the structure. The effects of the material parameters on the radiation are illustrated with a representative structure, with excitation provided by a Gaussian current pulse. The structure consists of a GaAs substrate with relative permittivity of approximately 12 at the highest frequency involved in the experiment. A worst-case scenario is presented, with absorption equal to zero. The integration surface is placed external to the inhomogeneous material, as discussed in Section 2.2. The dimensions of the structure are shown in Figure 3.8. For some applications, such as the photoconducting system, a uniformly distributed current density transverse to the plane of the GaAs substrate is as-

sumed. Therefore, the excitation model for this experiment consists of a vertical array of dipoles embedded uniformly in the GaAs substrate, as shown in Figures 3.1(b) and 3.8. The observation point is 100μm above the center of the GaAs substrate, where the received pulse is approaching the far-field response, i. e., the derivative of the current excitation in free space.

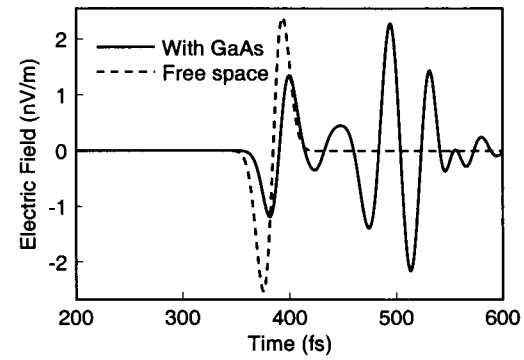

(a)

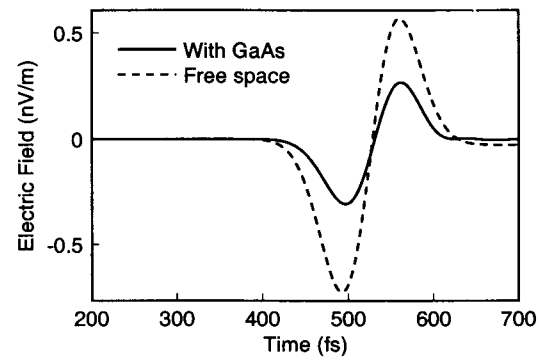

(b)

Figure 3.9: Electric field 100μm from the source for two different pulse widths: (a) τ=56 fs and (b) τ=30 fs. Transit time to the far edge of the GaAs substrate is 87.8 fs. Dashed lines represent the calculation for an ideal dipole in free space, with an appropriate time delay to account for the presence of the GaAs.

Distortion of the received signal occurs when the pulse width, τ, is narrow enough for reradiation from the air/GaAs interfaces to become resolvable. Results are presented

in Figure 3.9 for two cases with pulse widths that correspond to approximately (a) 2/3 (τ=56 fs) and (b) 1/3 (τ=30 fs) of the transit time to the far edge of the GaAs substrate (which is 87.8 fs). Also shown are the cases for an ideal Hertzian dipole in free space. For both pulse widths, diffraction from the edges of the GaAs/air interfaces alters the received electric field. For the narrower pulse width, the diffraction additionally causes distortion of the received waveform. These effects would be neglected using the far-field approximation discussed in the previous section.

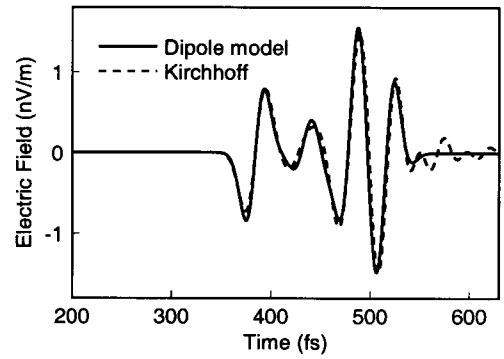

(a)

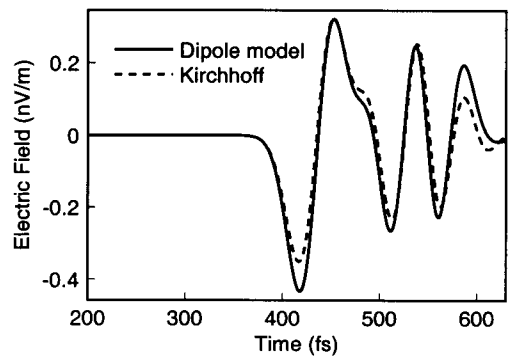

(b)

Figure 3.10: Model based on ideal Hertzian dipoles used to represent the reradiation from the corners of the GaAs/air interfaces of the structure shown in Figure 3.8. In (a) $\beta = 32$ and in (b) $\beta = 64$.

The edges and corners of the GaAs substrate shown in Figure 3.8 effectively act as new sources of radiation. A simple model using ideal Hertzian dipoles to represent the diffracting sources has been developed for this structure, based on the simulations using the FDTD/Kirchhoff technique. The excitation for each dipole is delayed corresponding to transit time through the GaAs substrate and attenuated appropriately. Results for the simple dipole model are presented in Figure 3.10, where comparison is made to the field found using the FDTD/Kirchhoff technique. Five dipoles are used to represent reradiation from the top and bottom edges, where advantage has been taken of the symmetry of the structure relative to the observation point. It may be seen that, while the model is not exact, many of the effects of inclusion of the GaAs material may be accounted for using a very efficient computational technique. This model would be difficult to develop without comparison to a rigorous solution such as that provided by the FDTD/Kirchhoff technique.

3.4 Characterization of the Photoconducting Structure

Building on results from the previous example, the complete photoconducting structure shown in Figure 3.11 is now characterized. The dimensions of the structure are similar to those given in the last example, but with W=14.26μm and L=35.88μm. The metal strips are assumed to be perfect conductors, 1.6μm wide, 0.23μm thick, and separated by 10μm. The time-varying current density in the substrate has been modeled using the combined Monte Carlo/FDTD simulation technique described in Section 3.1. Three typical current pulses are shown in Figure 3.12 to demonstrate the effects of varying the bias voltage and the thickness of the GaAs substrate.

These realistic current pulses contain random high frequency content. To study effects caused by inhomogeneous material parameters, rather than by errors in FDTD modeling (see Section 2.1.2), the frequency content of each pulse is limited to the degree that FDTD stability criteria are satisfied. This is verified by comparing the time derivative of the current pulse to the far-field radiation generated by the combined FDTD/Kirchhoff integral method for the homogeneous case.

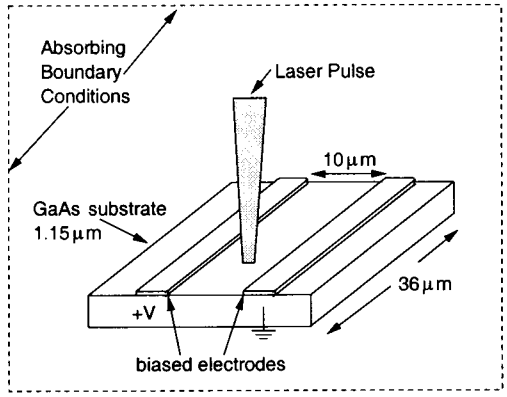

Figure 3.11: The complete photoconducting structure, including GaAs substrate and metal electrodes. The location of the absorbing boundary conditions used in the combined FDTD/Kirchhoff method is indicated.

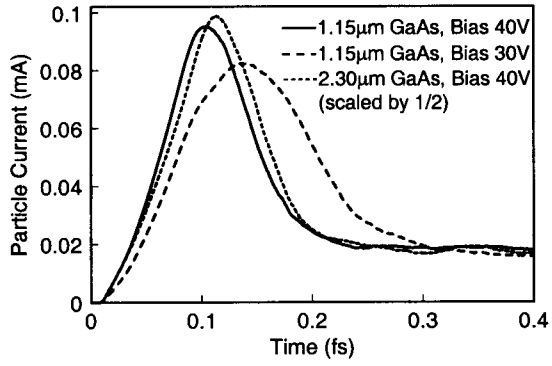

Figure 3.12: Comparison of three different current pulses generated by the photoconducting experiment.

The far-field radiation arising from two of these current pulses is presented in Figures 3.13 and 3.14, where the fields are measured: a) off the axis of the dipole (E-plane) and b) transverse to the axis of the dipole (H-plane). Simulation results are presented for a narrow pulse (the solid line in Figure 3.12, with 1.15μm GaAs, bias=40V) and for a wider pulse (the dashed line in Figure 3.12, with 1.15μm GaAs, bias=30V). In each case the GaAs substrate is included and comparison is made with and without the metal electrodes. The narrower pulse shows more distortion due to reradiation from the edges of the GaAs substrate, particularly for the H-plane observation points. In a homogeneous problem

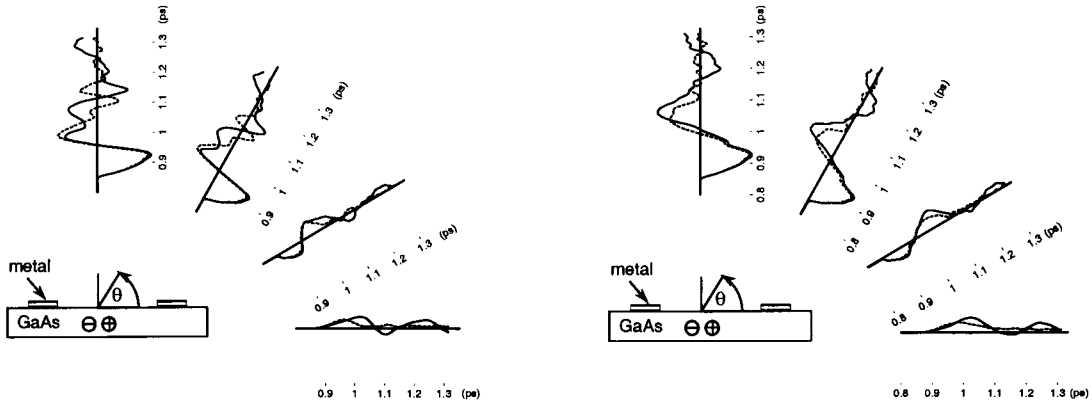

(a) (b)

Figure 3.13: E-plane comparison of the fields from (a) the narrower current pulse and (b) the wider current pulse in Figure 3.12 at observation points 250μm from the center of the structure at angles of 0°, 30°, 60°, and 90° from the plane of the substrate and off the axis of the dipole array. The dashed lines represent the structure with the GaAs substrate only; the solid lines include the metal contacts.

space, the H-plane waveforms would be identical. Effects of the metal electrodes include increased confinement of the field to the substrate region and additional distortion due to reradiation from the edges and corners of the metal. The significance of these effects is, again, pulse-width-dependent, with quite severe distortion of the field from the narrower pulse. For the wider pulse width, the effects of reradiation are less significant, however, the pulse is still distorted. For the narrower pulse in particular, severity of the distortion could affect timing measurements of the received signal pulse. Effects such as these due to inclusion of the material parameters would be difficult to model using other techniques, particularly for far-field radiation.

3.5 Conclusion

Use of the combined FDTD/Kirchhoff technique has been demonstrated to determine accurately and efficiently near- and far-field radiation from microwave and ultrafast electronic devices. Effects of the inclusion of materials in simulations of high frequency systems was explored with an example in which a dipole source embedded in a GaAs sub-

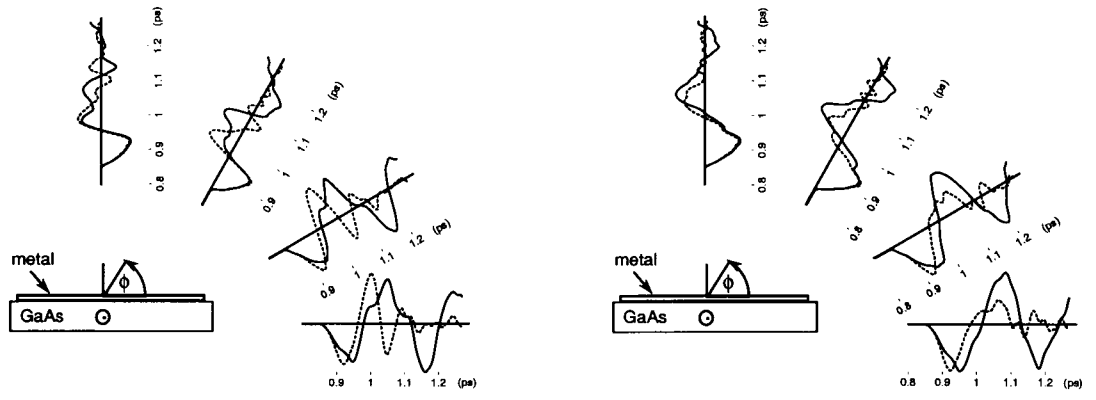

(a) (b)

Figure 3.14: H-plane comparison of the fields from (a) the narrower current pulse and (b) the wider current pulse in Figure 3.12 at observation points 250μm from the center of the structure at angles of 0°, 30°, 60°, and 90° from the plane of the substrate and perpendicular to the axis of the dipole. The dashed lines represent the structure with the GaAs substrate only; the solid lines include the metal contacts.

strate was excited with current pulses of various durations. Pulse-width-dependent effects were shown to be significant in an application of the method to the analysis of a photoconducting structure. Additionally, the combined FDTD/Kirchhoff technique was used to develop a simple model of the radiation from an inhomogeneous structure. Further improvements to the method may include consideration of the frequency-dispersive effects of the substrate material. The technique described here is, in many situations, more efficient than the FDTD method alone since the wave needs to propagate only to the integration surface, where it is transformed in space to the observation point. It is expected that the technique will be of benefit in a wide range of ultrafast device modeling applications.

4. INDOOR PROPAGATION MODELING

The utilization of wireless communication systems in indoor environments has greatly increased in recent years. Radiative systems including cellular phones, pagers, personal communication systems (PCS), wireless modems, and wireless local area networks (LANs) are used in both the workplace and the home. Wide bandwidth signals utilized in many of these modern communication systems are particularly sensitive to the detrimental effects of multipath distortion and dispersion. In digital systems, these effects can cause intersymbol interference (ISI) and can ultimately limit the data rate of the entire system. Multipath and dispersion tend to be more pronounced in indoor environments where object feature size often approaches the wavelength of operation. As a result, computational modeling of indoor wireless communication systems is critical for accurate and efficient system design. Additionally, computational modeling of propagation systems reduces the need for measurements, which are often time consuming and/or expensive.

Computational techniques currently used in propagation modeling can be classified into two main categories: empirical techniques and deterministic techniques. Empirical modeling techniques utilize statistically-derived classifications based on measurements performed in various types of environments. Classification of these propagation environments is based on the density and size of scatterers (objects that interact with the propagating signal). As an example, an indoor propagation environment may have significant loss due to interference caused by a relatively large number of scatterers in the local environment, and would therefore have a high loss classification. An outdoor suburban environment, where objects are more widely spaced and are of larger size relative to the incident wavelength, would tend to have a lower loss classification. Examples of statistical modeling techniques are given in Refs. [15, 16, 19, 104].

Deterministic techniques for computational modeling are site-specific, that is, models are developed incorporating the physical features of each propagation environment. In Chapter 4, only deterministic propagation modeling techniques are considered. Currently, one of the most common site-specific computational modeling techniques is ray-tracing

[56, 57, 58]. In ray-tracing, the principles of ray optics analysis are utilized, that is, field propagation is assumed along discrete ray paths from transmitter to receiver. In general, this assumption is valid when the wavelength is small compared to the geometrical dimensions of objects in the propagation environment, the so-called "high frequency approximation."

The goal of the work presented in this chapter is to improve the ray-tracing technique for use in indoor wireless applications. Ray-tracing is a computationally efficient deterministic method. However, because of the inherent high frequency approximation, the accuracy of the ray-tracing method depends, among other things, on the wavelength of operation as compared to the size of local scatterers. This is a particularly important issue in indoor environments, where obstacle feature sizes may approach or be less than the wavelength of operation, especially at the lower PCS frequencies of 900 MHz ($\lambda \approx 34$ cm) and 1800 MHz ($\lambda \approx 17$ cm).

Therefore, the accuracy of the ray-tracing technique in the characterization of indoor propagation environments, or *channels*, is first explored. Errors in the ray-tracing method as the high frequency approximation becomes invalid are quantified by comparison to a "standard," that is, a solution known to be accurate. The standard is generated, in this case, using the FDTD method or the combined FDTD/Kirchhoff method. Additionally, based on simulation results, a method is developed to enhance the accuracy of ray-tracing in the characterization of non-line-of-sight (NLOS) diffracted signals arising from objects with finite conductivity.

The chapter begins with a review of the ray-tracing method in Section 4.1. The method is described, and the basic equations used in the method are derived. In Section 4.2, some basic parameters relevant to the modeling of wireless communication channels are defined. In Section 4.3, the use of both ray-tracing and the FDTD method for wireless communication channel modeling is demonstrated, including a discussion of important implementation considerations for each technique. Both techniques are then utilized in a simple numerical experiment designed to illustrate channel modeling concepts in an indoor environment. Results are compared to published measurement data. In Section

4.4, experiments are carried out characterizing the accuracy of the ray-tracing method as scatterer size approaches the wavelength of operation. Results are presented for a variety of propagation channel configurations, including those in which both reflection and diffraction play dominant roles, and those in which diffraction dominates. In Section 4.5, it is shown that the model for diffraction commonly used in ray-tracing programs can give inaccurate results in certain propagation configurations for scatterers made of dielectric material with finite or zero conductivity. The development of a method to minimize the inaccuracies in the diffraction model is then presented. The chapter ends with a summary and conclusion.

4.1 A Review of the Ray-Tracing Method

Ray-tracing is a commonly used method for site-specific prediction of the radio channel characteristics of wireless communication systems. The ray-tracing technique inherently provides time delay and angle of arrival information for multipath reception conditions. Therefore, the ray-tracing technique is particularly attractive for indoor propagation environments, since accurate representation of multipath and dispersion can be important for system design.

One of the primary calculation requirements in the ray-tracing technique is the determination of the dominant ray propagation paths, that is, determination of the rays which will significantly affect the received signal. The efficient calculation of dominant ray propagation paths for ray-tracing models is an active area of current research. Several different techniques have been proposed. The most basic is ray launching [58] in which the radiation sphere around the transmitter is divided into solid angular segments from which rays are launched. Imaging theory [57, 105, 106] replaces reflecting walls and corners with images of the illuminating source. Other techniques to determine the dominant propagation paths include the use of neural network algorithms [107, 108], the use of "cone launching" [109], in which cones are launched instead of rays, and various sweep algorithms [110]. The method of moments (MoM) combined with boundary integral equation (BIE) formalism [111] has been proposed for a full-wave deterministic solution. Full-wave solutions utilizing the FDTD method [112, 113, 114, 115] are also occasionally used in propagation model-

ing. The use of full-wave techniques is less common than the use of ray-based techniques because of the computational intensity involved. The MCS^{TM} ray-tracing software used in the present work utilizes imaging theory. Refer to [116] for a more complete discussion of this technique.

Ray-tracing is based on geometrical optics (GO) [56, 59, 62], a method for describing the propagation of EM radiation in terms of rays, that is, narrow "tubes" in which cross-sectional amplitude and phase are assumed constant. As the name geometrical optics implies, this technique is useful in the analysis of systems in which the *geometry* of the problem space, rather than the wave nature of the signal in scattering interactions, dominates in determining the received signal. Generally this condition implies that antennas or scatterers are electrically large, and it is the reason that GO-based techniques are called high frequency approximations. Scattering events are considered independent of each other in high frequency approximations; that is, it is assumed there is no interaction on the scatterer between, for example, reflected and diffracted rays. In modern GO-based techniques used for analysis of wireless communication systems (e. g., ray-tracing), the intensity, polarization, phase (or delay time), and angle of arrival of rays are considered in determination of the received signal. Rays which have propagated along various paths to the receiver are combined appropriately in order to accurately describe wave interactions.

The methodology of geometrical optics, however, is not always sufficient to describe propagation with adequate accuracy. Therefore, other related techniques are often combined with GO in the ray-tracing model. For example, a diffracted field is generated when a ray encounters an abrupt, wedge-like material discontinuity. The diffracted field may be described by the uniform theory of diffraction (UTD) [60, 61] and may simply be added to the GO field under the high frequency approximation.

4.1.1 Propagation Primitives

Ray-tracing techniques, such as the MCS^{TM} software [117] considered in the present work, utilize GO, UTD, and other scattering techniques to describe the effects of various environmental interactions on the amplitude, phase, and time delay of the received signal.

These environmental interactions are called *propagation primitives* in Ref. [116]. Three propagation primitives are considered in this chapter: free space propagation, specular reflection, and diffraction. Each is discussed briefly below. The reader is referred to [116] for a more complete discussion.

4.1.1.1 Free Space Propagation

Free space propagation occurs when a ray is propagating in a homogeneous medium (generally air) and encounters no environmental obstacles such as walls or corners. The expression for the free space field at the receive antenna can be found from the power flux density, P_d [118, 119],

$$P_d = \frac{P_t G_t}{4\pi s^2} = \frac{EIRP}{4\pi s^2} = \frac{|E_d|^2}{\eta_0} \qquad \left(\frac{W}{m^2}\right) \tag{4.1}$$

where P_t is the time average power into the transmit antenna, G_t is the gain of the transmit antenna in the direction of maximum radiation (as compared to an isotropic radiator), $4\pi s^2$ is the surface area of a sphere with radius s, and s is the distance from the source to the observation point. The commonly used expression *effective isotropic radiated power*, $EIRP$, is the maximum radiated power in the direction of maximum antenna gain, as compared to an isotropic radiator. The magnitude of the electric field at the input to the receive antenna is given by $|E_d|$, and η_0 is the intrinsic impedance of free space, $\sqrt{\mu_0/\epsilon_0}$.

The third expression for power flux density indicates that the amplitude of the electric field at the input to the receive antenna can be written as

$$|E_d| = \sqrt{P_d \eta_0} = \frac{1}{s}\sqrt{\frac{P_t G_t \eta_0}{4\pi}} \tag{4.2}$$

where $\sqrt{\frac{P_t G_t \eta_0}{4\pi}}$ is the reference amplitude at the transmit antenna. The complete expression for the electric field (magnitude and phase) becomes

$$E_d = \frac{1}{s}\sqrt{\frac{P_t G_t \eta_0}{4\pi}} e^{j(\phi_0 - \beta s)} \tag{4.3}$$

where ϕ_0 is the reference phase, and $e^{-j\beta s}$ is the spatial delay factor.

4.1.1.2 Specular Reflection

Reflection occurs when a ray propagating in some homogeneous material is incident on a second material with different electrical properties. In the high frequency approximation, it is assumed that reflection occurs from the specular point, that is, the point where the angle of reflection equals the angle of incidence, and that no sharp irregularities such as corners or edges are encountered (see Figures 4.1(a) and 4.1(b)). Reflection from and transmission through smooth surfaces, i. e., those in which "surface roughness" may be neglected, are used exclusively in this thesis. These reflections can be described using the Fresnel reflection coefficients, which are different for parallel and perpendicular polarizations. When the first medium is free space and $\mu_1 = \mu_2$, the Fresnel reflection coefficients can be given by [18, 56, 116]

$$R_{||} = \frac{\epsilon_r \sin\theta_i - \sqrt{\epsilon_r - \cos^2\theta_i}}{\epsilon_r \sin\theta_i + \sqrt{\epsilon_r - \cos^2\theta_i}} \tag{4.4}$$

$$R_{\perp} = \frac{\sin\theta_i - \sqrt{\epsilon_r - \cos^2\theta_i}}{\sin\theta_i + \sqrt{\epsilon_r - \cos^2\theta_i}} \tag{4.5}$$

where $R_{||}$ and $R_{\perp}$ refer to parallel and perpendicular polarization, respectively, θ_i is the angle of incidence, and ϵ_r is the relative permittivity of medium two. Parallel polarization occurs when the incident electric field is in the plane of incidence, while perpendicular polarization implies the electric field is not in the plane of incidence. The plane of incidence is defined as the plane containing the direction vector of the incident ray (β^i in Figure 4.1) and the normal to the reflecting surface (given by $\hat{n}$). For the cases shown in Figures 4.1(a) and 4.1(b), the plane of incidence is the plane of the page. For vertical wall reflections, a vertically polarized antenna (with respect to the ground) is perpendicular to the plane of incidence, while for horizontal reflections, such as from the surface of the ground, a vertically polarized antenna is parallel to the plane of incidence.

The electric field created by reflection is given by

$$\underset{\perp}{E^r_{||}}(s) = A(s)_R \underset{\perp}{R_{||}} \underset{\perp}{E^i_{||}} e^{-j\beta s} \tag{4.6}$$

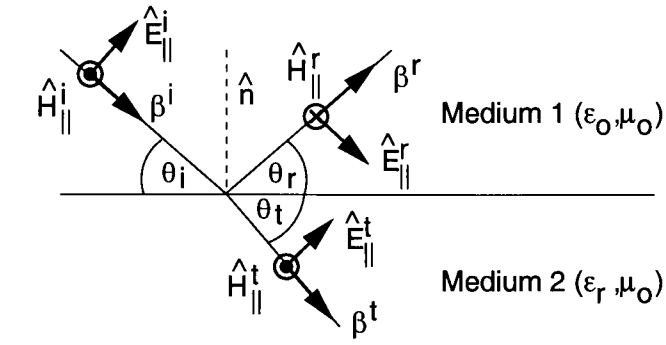

(a)

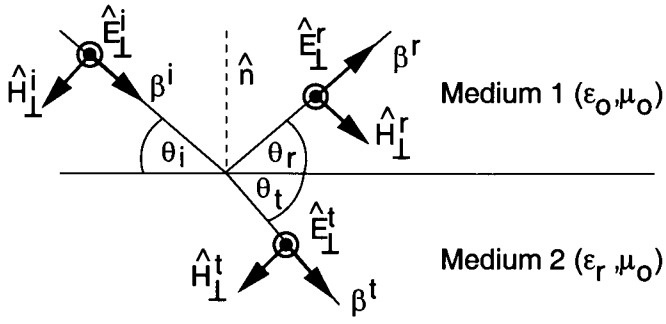

(b)

Figure 4.1: Uniform plane wave obliquely incident on an interface with (a) parallel polarization and (b) perpendicular polarization.

where s is the distance from the reflection point to the observation point and E^i is the incident field. The attenuation factor, $A(s)_R$, is given by

$$A(s)_R = \frac{1}{s} \tag{4.7}$$

For a perfect conductor, the magnitude of $R_{\substack{\parallel \\ \perp}}$ is one and there is no transmitted power. If the second medium is a dielectric, however, power will also be transmitted through the interface. The field corresponding to this transmitted signal is given by

$$E^t_{\substack{\parallel \\ \perp}}(s) = A(s)_R(1 + R_{\substack{\parallel \\ \perp}})E^i_{\substack{\parallel \\ \perp}} e^{-j\beta s}. \tag{4.8}$$

4.1.1.3 Wedge Diffraction

The principles of geometrical optics predict that in the *incident field shadow region* of an obstacle, that is, in the region not directly illuminated by the source (see Figure 4.2), the field is zero. Furthermore, GO predicts that in the transition region from the illuminated region to the shadow region, the field abruptly drops to zero. Both of these conditions are non-physical. *Diffracted rays* permit calculation of the fields in shadow regions and provide a more accurate representation of the fields in the transition regions [56, 116]. Wedge diffraction occurs when a freely propagating ray is incident on an edge or corner of a material other than the original transmission medium (often, the original transmission medium is air). Other types of diffraction include the creeping wave that arises when a field is incident tangentially on a curved surface, or diffraction that arises from the tip of a structure (a higher order effect than simple wedge diffraction [120]). In the present work, only wedge diffraction is considered, since diffraction of a radio signal around buildings, indoor furnishings, or other wedge-like objects is an important phenomenon in providing an accurate model of a wireless communication channel.

Under the high frequency approximation, diffraction is considered to be a local effect. Therefore, the diffracted ray is proportional to the incident ray multiplied by a diffraction coefficient, found from the solution of the appropriate boundary value problem. The development of the solution to this boundary value problem for use in ray-tracing was carried out by Joseph Keller in 1953 [60] and is known as the geometrical theory of diffraction (GTD). Diffracted rays originating from the edge of an infinite wedge are represented as cylindrical wave fields that decay as $\rho^{-1/2}$, where ρ is the distance from the edge.

The original GTD erroneously predicted singularities in the field at the shadow boundaries. Kouyoumjian and Pathak [61] proposed the uniform theory of diffraction (UTD) in 1967, introducing a correction factor based on a Fresnel integral in the shadow boundary regions to eliminate the singularities. The Fresnel integral goes to zero at the same rate the original diffraction coefficient tends to infinity. Away from the transition regions, the magnitude of the Fresnel integral is approximately one.

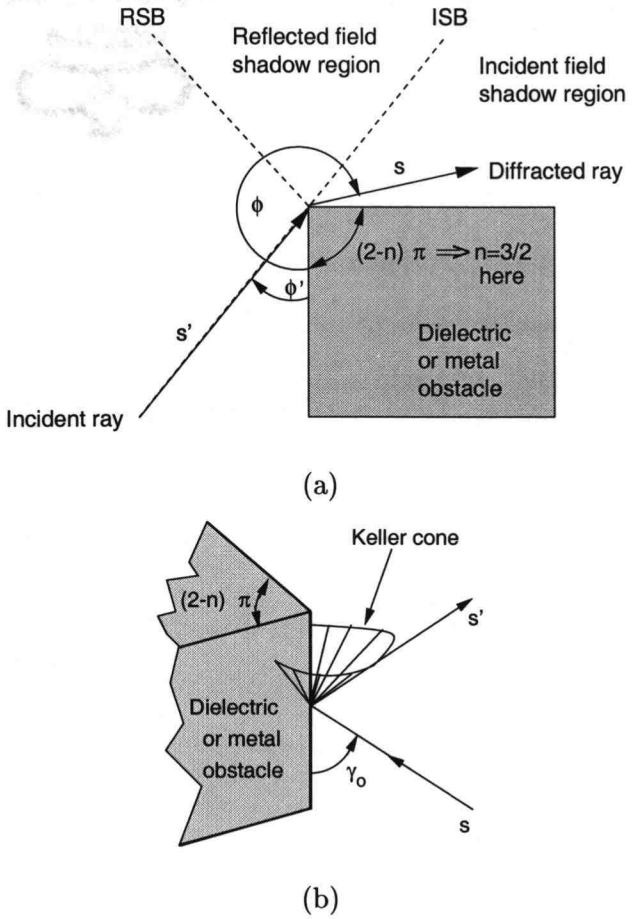

Figure 4.2: Geometry for diffraction calculations. (a) Top view showing the reflected field shadow boundary (RSB) and the incident field shadow boundary (ISB). (b) Elevated side view showing the Keller cone, created when the angle of incidence is not perpendicular to the diffracting wedge.

The GTD and the UTD were both developed utilizing only perfectly conducting wedge materials. Luebbers [121] in 1984 proposed the incorporation of Fresnel reflection coefficients in the diffraction coefficients to account for dielectric and lossy wedge materials. Luebbers' diffraction coefficients are used in many ray-tracing programs including MCS^{TM} [117], and their accuracy is one of the topics explored in the present work (Section 4.5). Luebbers' diffraction coefficients are given in Appendix D.

The expression for the diffracted field, E^d, is:

$$\underset{\perp}{E^d_{\parallel}}(s) = A(s', s)_D \underset{\perp}{D_{\parallel}}(L, \phi, \phi') \underset{\perp}{E^i_{\parallel}} e^{-j\beta s} \tag{4.9}$$

where s is the distance from the point of diffraction to the observation point, s' is the dis-

tance from the source to the point of diffraction, $D(L, \phi, \phi')$ are the diffraction coefficients given in Appendix D, and $A(s', s)_D$ is an attenuation factor given by

$$A(s', s)_D = \begin{cases} \frac{1}{\sqrt{s}} & \text{for plane and cylindrical wave incidence} \\ \left[\frac{s'}{s(s+s')}\right]^{1/2} & \text{for spherical wave incidence} \end{cases} \tag{4.10}$$

4.1.2 The Total Received Signal

In general, a ray may undergo several reflections and/or diffractions before it reaches the receive antenna. This can be accounted for simply by compounding the effects of each interaction. For each interaction, the field incident on the scatterer is multiplied by the coefficient associated with the appropriate propagation primitive (e. g. $R_{\substack{\parallel \\ \perp}}$ from (4.4) and (4.5) or $D_{\substack{\parallel \\ \perp}}$ from (D.2)) and the associated attenuation coefficient. The phase delay is also accounted for. For example, the total field received at a distance s from the transmitting antenna may be given as:

$$E_{ray}(s) = \frac{1}{s'_f}\sqrt{\frac{P_t G_t \eta_0}{4\pi}} \left[\prod_i A(s_{R,i})_R R_i\right] \left[\prod_j A(s'_{D,j}, s_{D,j})_D D_j\right] e^{-j\beta(s'_f + \sum_i s_{R,i} + \sum_j s_{D,j})} \tag{4.11}$$

where s'_f is the free space propagation distance to the first interaction and $\sqrt{\frac{P_t G_t \eta_0}{4\pi}}$ is the reference level at the transmit antenna (defined in (4.2)). The distance $s_{R,i}$ is from the i_{th} reflection point to the next interaction or observation point, $A(s_{R,i})_R$ is the i_{th} attenuation coefficient, defined in (4.7), and R_i is the i_{th} reflection coefficient, given by (4.4) or (4.5). The attenuation coefficient for the j_{th} diffraction is given by $A(s'_{D,j}, s_{D,j})_D$, defined in (4.10), and the j_{th} diffraction coefficient D_j is defined in (D.2)). The phase delay is given by $e^{j\beta(s'_f + \sum_i s_{R,i} + \sum_j s_{D,j})}$, and $s = (s'_f + \sum_i s_{R,i} + \sum_j s_{D,j})$ is the sum of all interaction path lengths.

In propagation environments where there are multiple ray paths from receiver to transmitter, i. e., for a multipath channel, the field due to each ray may be found by using (4.11) repeatedly. An example of this technique is presented in Section 4.3.

4.2 Multipath Channel Modeling for Indoor Environments

Accurate computational modeling of the propagation channel is especially important for indoor environments because of the number of objects (floors, ceilings, furnishings, etc.) which can provide multiple signal paths. Indoor propagation channels are therefore particularly sensitive to this type of "multipath distortion," which occurs when a signal is able to take more than one path from transmitter to receiver. Associated with each path is a corresponding amplitude and time delay. As a result, the various signal components may interfere with each other. In this section, some of the key parameters used in describing multipath channels are defined.

One important parameter characterizing multipath channels is the *power delay spread.* This parameter describes the extent of multipath in a particular environment. Generally, the larger the power delay spread, the more severe the multipath distortion and the greater the potential for intersymbol interference (ISI) in a digital signal. Depending on system design, detection errors resulting from ISI may ultimately limit the bit rate for a digital signal.

The *power delay profile* is a plot of the received power of the various multipath components over time. When measurements of the power delay profile are made ("channel sounding") [122], RF pulses are generated at a repetition rate longer than any observed delay [16, 18]. The *direct RF pulse method* [20] involves direct modulation of the RF carrier signal by short duration pulses. Because envelope detection is typically used, this technique has problems with interference and noise in detection of the wideband received signal. Additionally, the use of an envelope detector means that the phases of the individual multipath components are not detected. Frequency domain channel sounding is also possible [123]. An RF sweep generator scans a frequency band centered around the carrier frequency. A vector network analyzer monitors the frequency response of the received signal and performs an inverse Fourier transformation to recover the time domain pulse. This method requires careful calibration and synchronization between the transmitter and receiver, and it is not useful for characterization of time-varying systems. A third alternative for channel sounding is the use of a sliding correlator [124].

Whichever technique is used to determine the multipath components, the pulse must be narrow enough for resolution of the most significant multipath components, and so it will generally have a wide bandwidth. The power delay profile is therefore one type of *wideband* measurement. The pulse-modulated signal can be expressed as [123]:

$$s(t) = p(t)e^{j(\omega t+\phi)} \tag{4.12}$$

where $p(t)$ is the baseband pulse shape, ω is the RF carrier frequency, and ϕ is the phase of the signal.

Many multipath channels can be represented as a collection of discrete received signals (as opposed to a "diffuse channel," where the multipath components are not resolvable [19]). A discrete multipath channel can be represented as [18, 19]

$$h(t) = \sum_k a_k \delta(t - \tau_k) \tag{4.13}$$

where a_k is the amplitude of each multipath component, τ_k is the delay of each component, and δ is the Dirac delta function.

If there is no overlap of pulses, the signal may be represented by the baseband, or *low pass equivalent* model. The derivation of the low pass equivalent of the multipath channel is given in Appendix E. The power representation of the multipath signal may be then be found from (E.18), also described in [16]

$$|y(t)|^2 = \sum_k a_k^2 p^2(t - \tau_k). \tag{4.14}$$

Calculation of the power delay profile and other parameters is vastly simplified with the use of the low pass equivalent.

Three parameters often used in describing the characteristics of the multipath signal are the *multipath power gain*, the *mean excess delay*, and the *RMS delay spread* [18, 16]. These quantities are measured relative to the first signal which arrives at the receiver, usually along the direct path for line-of-sight systems. The expression for the multipath power gain simply shows that the total received power is related to the sum of the powers in the individual multipath components. The multipath power gain is defined as:

$$G \equiv \sum_k a_k^2. \tag{4.15}$$

Equations (4.14) and (4.15) can be used to calculate the received power for either wideband or narrowband signals, since received local ensemble average power will be equivalent for both [18, page 150].

The RMS delay spread is a description of the differential delay, that is, the difference in time between the shortest and the longest received signal paths above a given threshold. It gives the time period for which the received multipath signal is essentially non-zero. The RMS delay spread is defined as the square root of the second central moment of the power delay profile:

$$\sigma_\tau \equiv \sqrt{\bar{\tau^2} - (\bar{\tau})^2}, \tag{4.16}$$

where

$$\bar{\tau^n} \equiv \frac{\sum_k \tau^n a_k^2}{\sum_k a_k^2}, \qquad n = 1, 2. \tag{4.17}$$

The mean excess delay, $\bar{\tau}$, is the mean of the power delay profile. It gives information about the expected length of the delay spread, and thus the severity of multipath distortion. It is defined as the first central moment of the power delay profile.

To calculate these quantities (multipath power gain, mean excess delay, and RMS delay spread), a computational method is needed to find the amplitude and phase (or, equivalently, the time delay) of the arriving multipath components. In the following section, the ray-tracing method and the FDTD method are compared for this purpose. The relative accuracy of each method is discussed and important implementation considerations are presented.

4.3 Generation of the Power Delay Profile for a Multipath Channel

As described in Section 4.1, the ray-tracing method can be used to find the amplitude and phase or time delay of the multipath components of a received signal. These quantities can also be derived from FDTD simulation results. Because the FDTD method is a full-wave simulation tool, it is capable of providing very accurate information in multipath propagation environments. The FDTD method is not commonly employed in propagation modeling, however, because of the computational intensity of the technique.

In this section, utilization of the ray-tracing and FDTD methods for multipath channel modeling is introduced in the simulation of a simple multipath environment. Requirements for an accurate FDTD implementation are discussed. The ray-tracing and FDTD techniques are compared and contrasted in the determination of some key parameters commonly considered in wireless communication channel modeling (as described in Section 4.2). The section begins with a description of the simulation model, including the physical space and the radiative systems. Details of implementation specific to each modeling technique are next discussed. Finally, simulation results are presented showing a comparison to published measurements.

4.3.1 The Simulation Model

In the simple multipath environment considered here, a physical configuration consisting of an open space with a reflecting floor and a reflecting metal side wall is simulated. This system is similar to that described in Ref. [123]. The layout is given in Figure 4.3. Transmitting and receiving antennas 0.5 meter high and separated by 2.5 meters are placed at equal distances from the side faces of a metal wall whose front face is one meter square and whose depth is several meters. The wall is offset from the direct transmission path by one meter. There are four primary propagation paths: the direct, floor-reflected, side wall-reflected, and combined side-wall/floor-reflected paths. With this large wall size, diffraction is neglected since specular reflection dominates the multipath received signal.

The transmit and receive antennas are both modeled as dipole antennas of small physical size, approaching that of an ideal Hertzian dipole. This source is utilized since it is easy to model in the FDTD [84], the corresponding field equations arising from it are well known, and its small physical size makes it appropriate for wideband simulations.

As mentioned previously (see Section 2.1), several factors must be taken into account in the implementation of the FDTD method for an accurate simulation. The source excitation, grid size, and terminating boundary conditions are all important parameters.

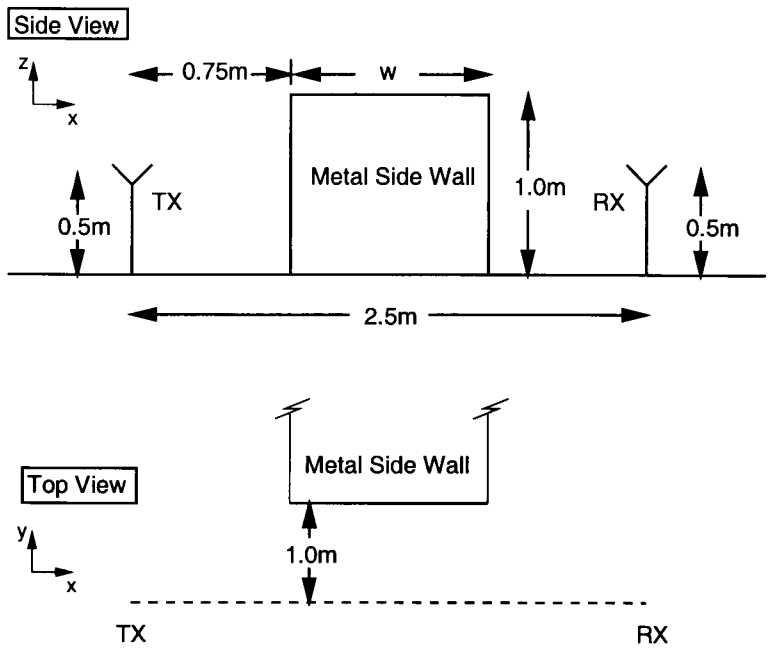

Figure 4.3: Configuration used to determine power delay profile. A room with a reflecting floor and a vertical metal plate one meter square is simulated. Transmitting and receiving antennas are placed equidistant from the vertical edges of the wall.

The source excitation is a 900MHz carrier modulated by a Gaussian pulse, $p(t)$, given by

$$p(t) = P_0 e^{-((t-t_0)/\tau)^2} \tag{4.18}$$

where $\tau \approx 1$ ns defines the pulse width, and $t_0 \approx 3.66$ ns is a time offset. See Figure 4.4. The pulse width is narrow enough for accurate resolution of the various multipath components. In this example, use of a pulse rather than sinusoidal excitation enables easy resolution of the multipath components. The received signal is demodulated using a lowpass filter, in this case, a 4-pole Chebyshev filter with a cutoff frequency of 600 MHz. Calculations of the power delay profile and other parameters are performed using the low pass equivalent (4.14).

The FDTD grid dimensions utilized here are small enough for accurate simulation of a modulated 900 MHz carrier. The frequency response of the modulated carrier used in this example is shown in Figure 4.4(b). The FDTD grid cell dimensions are chosen to be less than $1/10\lambda$ per cell side for f=1.27 GHz, the frequency at which the source

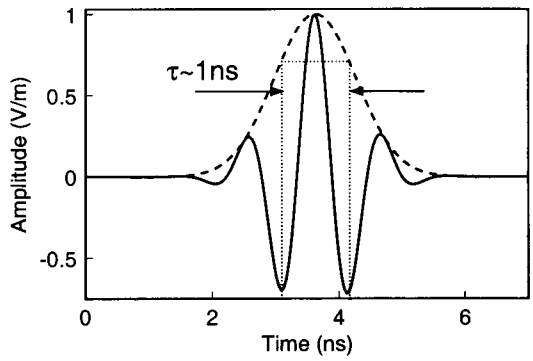

(a)

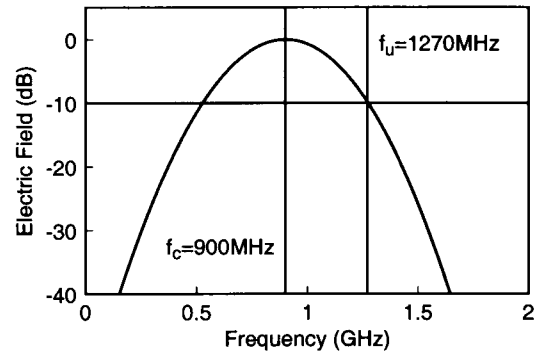

(b)

Figure 4.4: The modulated pulse used for calculation of the power delay profile. The Gaussian pulse is given in (4.18). The carrier frequency is 900 MHz. (a) Time domain representation. (b) Frequency domain representation.

signal strength is reduced by 10 dB. This frequency, denoted by f_u in Figure 4.4(b), has a corresponding wavelength of approximately 25 cm. Therefore, the grid cell size chosen for the FDTD simulations is 2.5 cm. For the simulation of the multipath environment, where dimensions are on the order of meters, the computational domain then becomes very large. In the present example, the overall grid size is 115x45x37 cells. The computational domain is terminated in absorbing boundary conditions (Berenger's Perfectly Matched Layer), as discussed in Section 2.1.

The measured data for this configuration are those presented in [123], in which a semi-anechoic chamber with an aluminum floor is configured as shown in Figure 4.3. Frequency

	Ray-Tracing	FDTD	Measured [123]
Direct	8.34ns	8.28ns	8.5ns
Floor	9.04ns	8.97ns	9.2ns
Side	10.67ns	10.53ns	10.9ns
Side/Floor	11.2ns	11.09ns	11.5ns

Table 4.1: Delay Time using Ray-Tracing, FDTD, and Measurements in Simulation of a Simple Multipath Environment.

domain channel sounding measurements are made using the technique described in Section 4.2. The microwave measurement system consists of a vector network analyzer (HP8510C), an X-band waveguide, open-ended waveguide aperture antennas, and hardware for data acquisition. The frequency is swept from 8.2-12.4 GHz, and the impulse response of the system is estimated using the network analyzer time domain option.

4.3.2 Computational Results

Simulation results showing delay times for the propagation environment of Figure 4.3 are presented in Table 4.1. The ray-tracing timing results were calculated analytically using the free space and reflected field propagation primitives (Section 4.1). The maximum FDTD discretization error of one-half grid space is $0.025m/(2c) \approx 0.042$ ns, corresponding to a significant part of the difference between the FDTD method results and the ray-tracing (theoretical) results. The remaining error may be attributed to grid dispersion, since the overall grid size is quite large (115x45x37 cells). Note that use of the Kirchhoff transformation would alleviate both the grid discretization and grid dispersion problems since the observation points would not be limited to grid cell locations and the grid size could be reduced, minimizing the effects of grid dispersion. The discrepancies between the measurement timing data and the ray-tracing solution are not surprising since timing measurements into the tenths of nanoseconds are at the limit of current channel sounding technology [123].

Figure 4.5 shows the power delay profile generated using the FDTD method (solid lines) and the ray-tracing/theoretical technique (vertical lines with circles). The four multipath components that correspond to the direct, floor-reflected, side-reflected and combined side/floor-reflected paths are clearly discernible. Note that the amplitude of the floor-reflected pulse is lower than the side-reflected pulse, even though the free space path is shorter. This is because the ideal dipole source (2.20) has maximum E-plane radiation perpendicular to the axis of the antenna, where the angle of elevation, $\theta, = 90°$. For lower angles of elevation, as in the case of the ray angled toward the floor, the radiation is less, reaching 0.707 E_{max} at $\theta = 45°$. In these simulations, the radiation angle is calculated analytically for each ray-tracing/theoretical solution.

The mean excess delay for the FDTD method is calculated to be 1.18 ns, and the RMS delay spread is 1.17 ns (the horizontal line marked with triangular symbols in Figure 4.5). Error in received signal amplitude found using the ray-tracing method is caused in part by the exclusion of diffracted rays in the simulation and by the difficulty in incorporating the antenna pattern in the side/floor-reflected ray. For the ray-tracing method, the mean excess delay is 1.19 ns and the RMS delay spread is 1.16 ns. These results are similar to those found using the FDTD method, indicating good agreement between the two computational techniques.

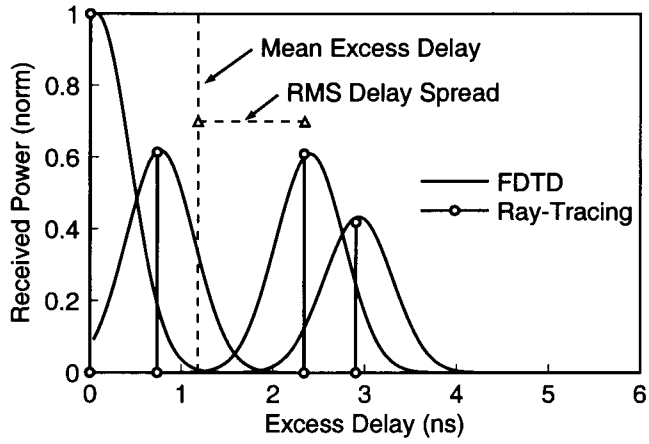

Figure 4.5: The power delay profile for the simulated configured in Figure 4.3. The FDTD solution (solid lines) is compared to a ray-tracing calculation (vertical lines with symbols) demonstrating comparable timing and amplitude results for both techniques.

4.4 Accuracy of the Ray-Tracing Method for Small Scatterers

As stated in Section 4.1, ray-tracing is a high frequency approximation technique for site-specific characterization of electromagnetic wave propagation. In other words, the size of local scatterers relative to the wavelength of operation is an important consideration in the accurate implementation of the ray-tracing method. As feature size decreases relative to incident wavelength, limits on the accuracy of GO and UTD emerge, as has been discussed in previous work [120, 125, 126]. The work presented in this section extends these discussions.

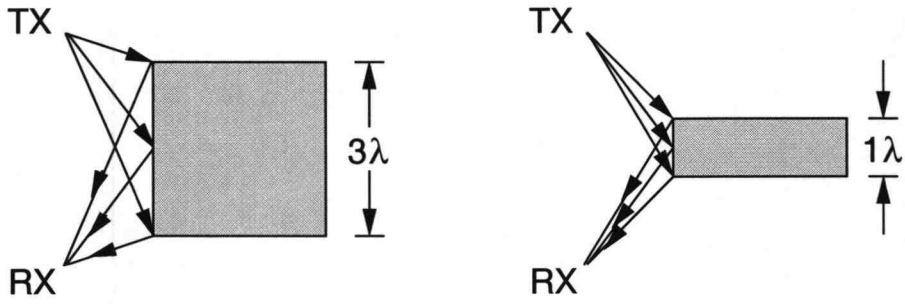

Figure 4.6: The limits on the accuracy of ray-tracing for various scatterer sizes is demonstrated in Section 4.4.

The accuracy of the ray-tracing method for local scatterer sizes approaching the wavelength of operation is investigated, as illustrated in Figure 4.6. A comparison is made between simulation results provided by the FDTD method and results based on ray-tracing. The FDTD method is computationally intensive and is therefore generally not practical for site-specific modeling and/or for use with large computational domains. It is, however, very accurate for moderately sized grids [80]. For larger computational domains, the FDTD method may be combined with a near-to-near or near-to-far field transformation technique such as the Kirchhoff surface integral formulation, as demonstrated in Section 2.2. The ability of the FDTD technique to analyze structures of arbitrary shape and material is a great asset in the present application. In this section, the FDTD method and the combined

FDTD/Kirchhoff technique are used as standards for verification and validation of the ray-tracing technique.

A numerical experiment designed to illustrate the dependence of the ray-tracing method on feature size of local scatters is presented. Simulation results show that when the magnitude and phase of the received rays are properly accounted for, the ray-tracing technique describes the received scattered signal strength quite accurately, even when the scatterer size is a fraction of a wavelength. The importance of the inclusion of the diffracted rays in simulations with so-called "small" scatterers is also demonstrated.

4.4.1 Description of the Numerical Experiment

In the following section, the numerical experiment used to quantify the accuracy of the ray-tracing method for electrically small scatterers is described. The physical configuration of the experiment is first given. Then important implementation aspects for both the ray-tracing method and the FDTD method in the experimental procedure are discussed.

4.4.1.1 Physical Configuration

The experimental configuration is similar to that presented in Section 4.3, with a vertical wall offset between transmit and receive antennas of equal height, as shown in Figure 4.7. There are two primary differences in this example compared to the earlier structure: First, the wall is of variable width, which means that diffracted rays must be included in the analysis, and second, the reflective floor is eliminated. Because diffracted rays are now included in the simulation, the wall is made higher to ensure that diffraction over the top may be neglected. With this configuration, the ray-tracing method generates four rays corresponding to the direct path, as well as a specular reflection from the wall and two corner diffractions from the vertical edges of the wall.

To demonstrate the effect of obstacle size on the scattered signal, consider the FDTD mesh plots shown in Figures 4.8(a) and 4.8(b). These plots show a horizontal cross section of the simulation space, including the wall, which is made, in this example, of a perfect electrically conducting (PEC) metal. The locations of the transmitter and receiver are

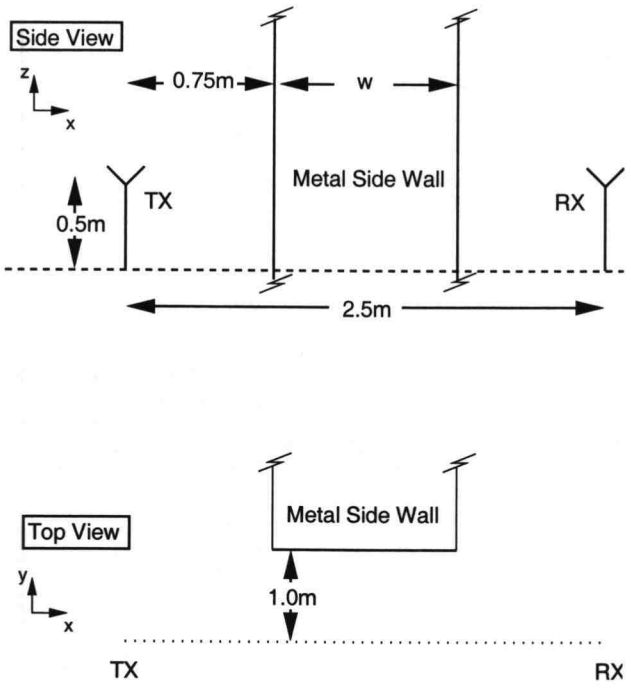

Figure 4.7: Configuration used in simulations.

indicated in each figure. The scattered field is found in two steps: The field corresponding to the direct path is first found in a simulation with no metal wall. Then a second simulation is conducted in which the metal wall is included. The scattered field is calculated by subtracting the direct path field from the simulation result which includes the metal wall. The scattered field result is shown in Figures 4.8(a) and 4.8(b) for two different wall sizes: 2λ (a) and 0.2λ (b). For the larger wall, the diffracted and reflected components of the scattered signal can be clearly discerned. However, for the smaller wall, the magnitude of the reflected component is reduced, making it difficult to see what effect, if any, this ray will have on the received signal. Note that because the direct field has been simply subtracted out, the result in the incident field shadow region (Figure 4.2) is incorrect and should be disregarded.

Three configurations are now considered for various ray interactions (refer to Figure 4.9): First the transmitter and receiver are equally spaced on either side of the wall (Case A), yielding diffraction and specular reflection. The receiver is next positioned nearer the

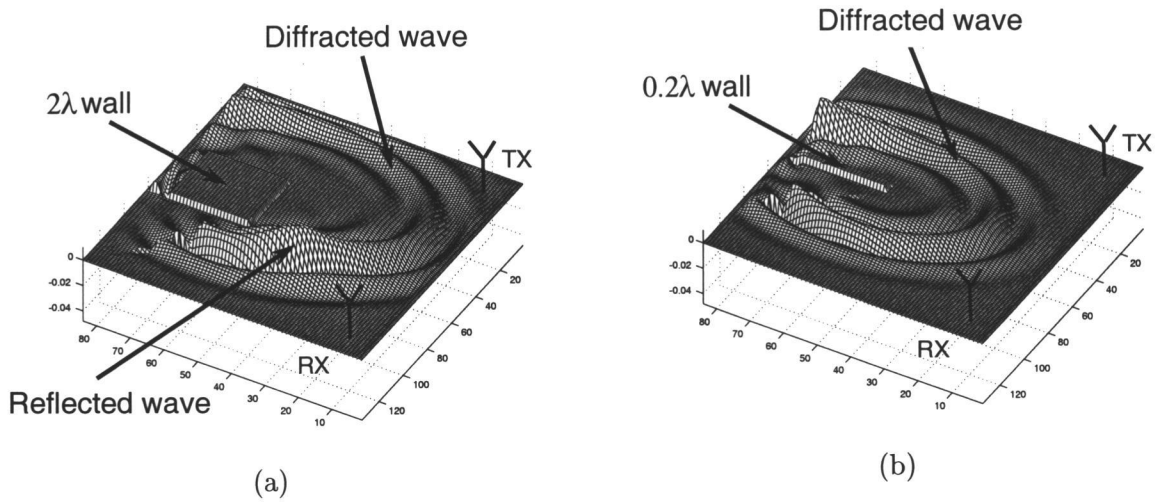

Figure 4.8: Mesh plots showing reflection and diffraction for (a) metal wall of width 2λ and (b) metal wall of width 0.2λ. In each case the direct wave has been subtracted out.

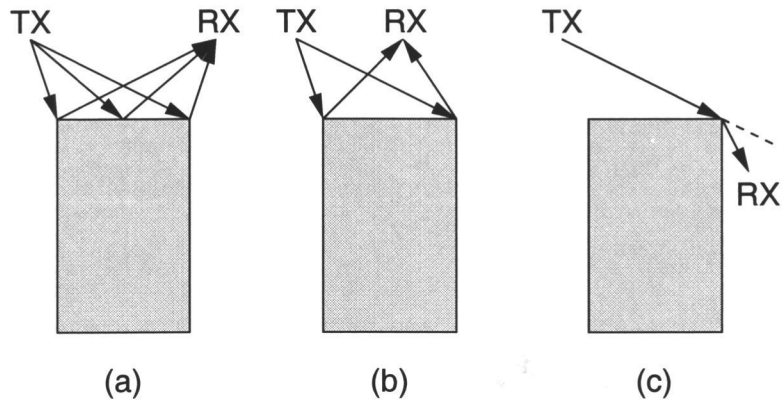

Figure 4.9: Ray interactions considered in Section 4.4 are (a) diffraction and specular reflection, (b) diffraction and "non-specular" reflection, and (c) diffraction field only.

wall (Case B), yielding diffraction and "non-specular" reflection. Finally, the receiver is positioned in the incident field shadow boundary (Case C), yielding a diffraction field only.

4.4.1.2 The Ray-Tracing Method

To find the exact scattered field from an object whose dimensions approach the wavelength of operation, it is necessary to use rigorous full-wave computational techniques

which allow incorporation of details of the scattering surface. Exact techniques include integral equation solutions: the electric field integral equation (EFIE) and the magnetic field integral equation (MFIE) [23, 24, 127, 128]. Integral equation techniques involve finding the surface current of the illuminated scatterer, which is then used as a new source of radiation. The FDTD method is a strictly numerical technique and thus it cannot render fully exact results in this application. However, it may be used, often with sufficient accuracy, to approximate the scattered field, as is done here.

The approach used with ray-tracing in this experiment is an approximation called the *relative phase method* [129, 130]. The relative phase method involves vectorially combining the contributions from individual scattering elements on a single structure. Vectorial combination is utilized even when the scatterer size is only on the order of a wavelength. Historically this technique has been used to find the radar cross section (RCS) of a complex scatterer when it is not feasible or efficient to use a more accurate method. The relative phase method is described in more detail in Appendix F. Use of this method in the present work provides a simple technique for approximating the received signal strength from a single, physically small scatterer. The ray-tracing program MCS^{TM} is used to generate the "experimental" data.

4.4.1.3 The FDTD Method

The source excitation used is a 900MHz carrier modulated by a Gaussian pulse, $p(t)$:

$$p(t) = P_0 e^{-((t-t_0)/\tau)^2} \tag{4.19}$$

where $\tau \approx 1$ ns defines the pulse width, and $t_0 \approx 3.66$ ns is a time offset (see Figure 4.4). The pulse width has been selected to be narrow enough for accurate resolution of the scattered pulse when compared to the direct received pulse (Figure 4.10), yet wide enough to allow coincident illumination of the wall and associated corners. Pulse spreading of the scattered pulse due to the separate effects of reflection and diffraction is thus minimized. That is, the righthand pulse in Figure 4.10 will have approximately the same width for a wide range of wall sizes despite the difference in the arrival times of the reflected and diffracted waves.

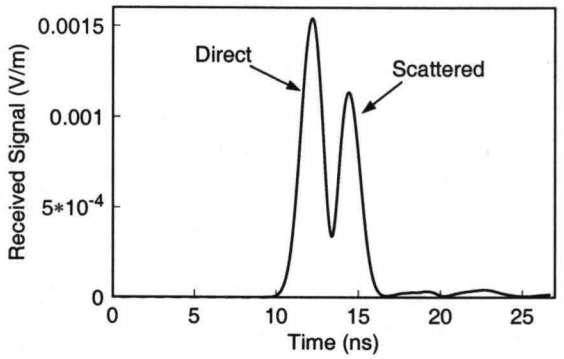

Figure 4.10: Typical demodulated received pulse found with the FDTD method.

The grid cell size $\Delta x = \Delta y = 0.025$ m and $\Delta z = 0.075$ m has been chosen so that height can be increased to minimize diffractive effects over the top of the wall. The cell size of 0.025 m corresponds to approximately $\lambda/15$ at 900 MHz. The computational domain has again been terminated in PML boundary conditions, as discussed in Section 2.1. Calibration between the FDTD simulation and the ray-tracing simulation is accomplished by equating the amplitude of the received direct path signal generated by means of each technique.

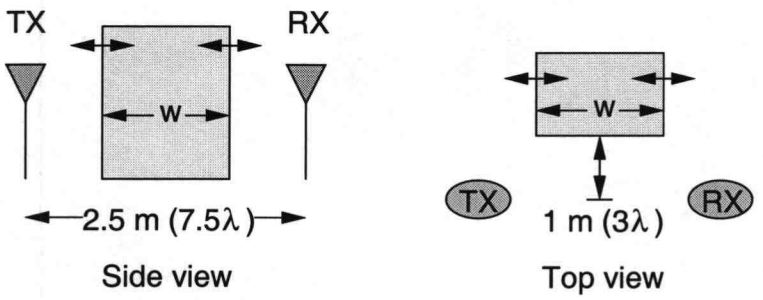

Figure 4.11: Spatial configuration used for Case A. Transmitter and receiver are spaced equally from the center of the wall. The edges of the wall move laterally in equal increments with respect to transmitter and receiver.

4.4.2 Case A: Diffraction and Specular Reflection

In this case, the transmitter and receiver are located equal distances on either side of the wall, as shown in Figure 4.11. The width of the wall, w, varies from 0.2λ to 10λ. Figures 4.12(a) and 4.12(b) indicate that use of the relative phase method provides a fairly accurate portrait of the scattered field strength, even when the dimension of the scattering wall is a fraction of a wavelength.

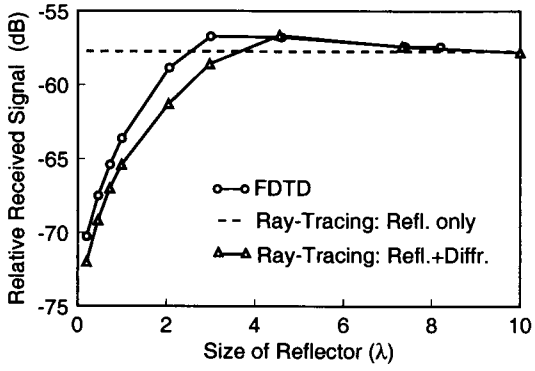

(a)

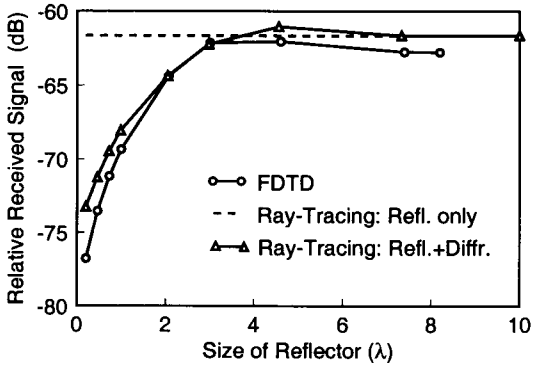

(b)

Figure 4.12: Simulation results for Case A: A comparison of the received signal strength for (a) a metal wall and (b) a dielectric wall with and without the inclusion of diffraction rays. The relative signal levels are referenced to the direct ray.

Figure 4.12(b) shows a comparison of ray-tracing and FDTD total received signal for a dielectric wall. The wall material is that of a poor insulator, like wood, with $\epsilon_r = 10$ and conductivity $\sigma = 0.1$ S/m. The results show a greater overall loss, but behavior of the received rays is similar to that of the perfectly conducting metal wall shown in Figure 4.12(a).

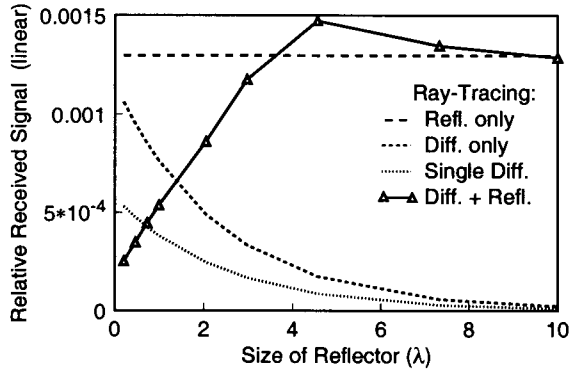

(a)

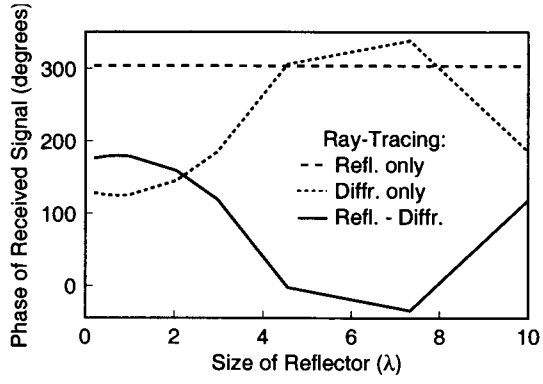

(b)

Figure 4.13: The magnitude (a) and phase (b) of the received signal rays for the metal wall of Case A (see Figure 4.12(a)).

Theoretically, as the width of the wall increases, the three curves in Figures 4.12(a) and 4.12(b) should converge to the value of the specularly reflected signal. The difference in received signal strength between the FDTD method and ray-tracing curves for large

wall sizes may be attributed to resolution accuracy of receiver placement in the ray-tracing program. The feature sizes utilized in this experiment are extremely small relative to a typical ray-tracing simulation. A similar range of error may be expected in the other ray-tracing data points as well.

As demonstrated in Figures 4.8(a) and 4.8(b), as scatterer size decreases, the relative amplitude of the reflected wave decreases. Since the specularly reflected ray in the ray-tracing method is independent of scatterer size, this indicates that as the feature size is reduced the contribution from the diffracted rays becomes significant. In fact, it appears that in ray-tracing, the diffracted rays compensate for the non-physical nature of the specularly reflected ray, as is now discussed.

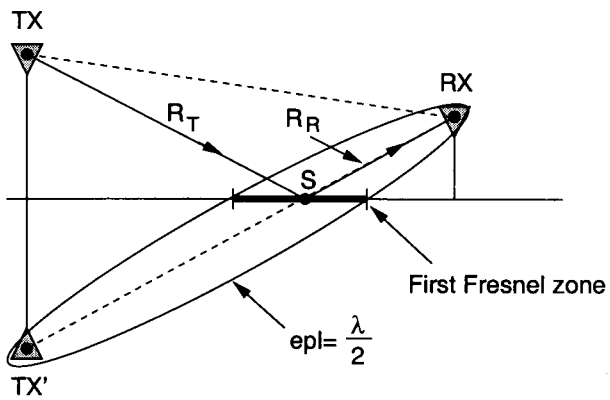

Figure 4.14: Definition of the first Fresnel zone.

Figures 4.13(a) and 4.13(b) show the components of the ray-tracing signal, plotted on a linear scale. For smaller wall sizes, the magnitude of the two diffracted rays, combined using the relative phase method, is significant. As shown in Figure 4.13(b), the diffracted and reflected signals are out of phase for small wall sizes, yielding a total received signal of small magnitude. Likewise, when the two signals are in phase, the total received signal is maximum. The point at which the two rays (diffracted and reflected) are in phase (wall size of approximately 4λ) is the point where the *extra path length* (*epl*), i. e. the difference

in path length between the diffracted and reflected rays, is $\lambda/2$. This is also the edge of the first Fresnel zone [131], as shown in Figure 4.14. The Fresnel zones describe the spatial regions where signals add either constructively (e. g. for $epl < \lambda/2$) or destructively. These regions alternate every multiple of $\lambda/2$ of the *epl*. However, the magnitude of the oscillatory effect decreases as the extra path lengths get larger, and thus the effect is not noticeable for larger wall sizes in Figure 4.13.

One way to determine the Fresnel zone (Figure 4.14) is to form an ellipsoid of revolution around the straight line connecting 1) the image of the transmitter, TX'; 2) the specular reflection point, S; and 3) the receiver, RX, with the focal points at TX' and RX. The intersection of the reflector plane with the ellipsoid of revolution is called the first Fresnel zone. Rays which fall inside this region add constructively, adding perfectly in phase at the edge, where $epl = \lambda/2$. In general, the center of the Fresnel zone does not correspond to S unless $R_T = R_R$. However, in the examples just presented in Case A this is true.

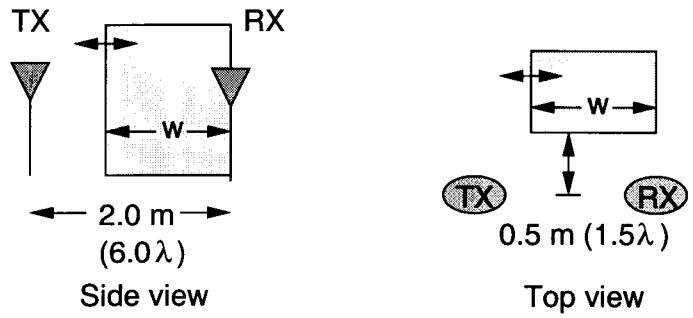

Figure 4.15: Spatial configuration used for Case B. The receiver location is fixed in line with one edge of the wall. The other edge of the wall moves laterally.

4.4.3 Case B: Diffraction and Non-specular Reflection

In the next experimental scenario, Figure 4.15, the position of the edge of the wall nearest the receiver is fixed. The transmitter is positioned so that, for smaller wall sizes, no

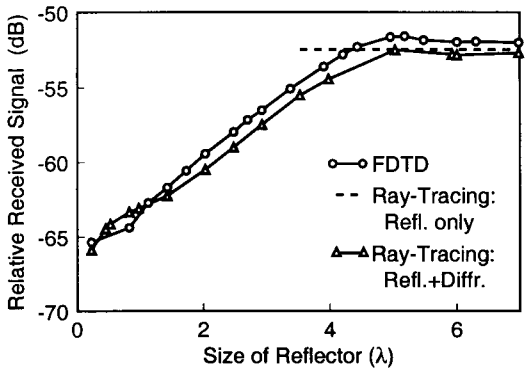

Figure 4.16: Simulation results for Case B: A comparison of the ray-tracing and FDTD method for a shallower angle of incidence than that of Case A. No specular reflection occurs for wall sizes less than $\sim 4\lambda$.

specularly reflected rays are generated. Again, good agreement is seen between the FDTD method and RT results for wall sizes from $\sim 0.2\lambda - 7\lambda$ (see Figure 4.16). In particular, this example demonstrates the accuracy of the diffracted ray solutions in the illuminated region of the problem space.

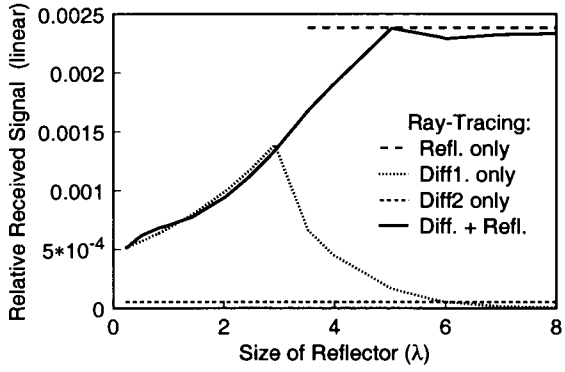

Figure 4.17: Components of the ray-tracing signal for Case B.

The components of the ray-tracing solution, shown on a linear scale in Figure 4.17, indicate that for smaller wall sizes the solution is dominated by the diffracting ray farthest from the transmitter. Equations (4.10) and (4.7) show that diffracted rays decay as $s^{-1/2}$

and reflected rays decay as s^{-1}, respectively. Therefore, this result is not unexpected. Figure 4.17 also shows that the diffracted and reflected rays combine in a manner similar to that in the previous example, adding increasingly in phase as the wall size increases until the maximum signal is received for $epl = \lambda/2$.

4.4.4 Case C: Diffraction Only

To characterize the received signal in the incident field shadow region (defined in Figure 4.2), the simulation configuration shown in Figure 4.18 is utilized. For the ray-tracing simulations, receivers are placed every 1° around the diffracting corner. For the FDTD method, 50 receivers are spaced every 5.4° over the 270° arc (see Figure 4.19).

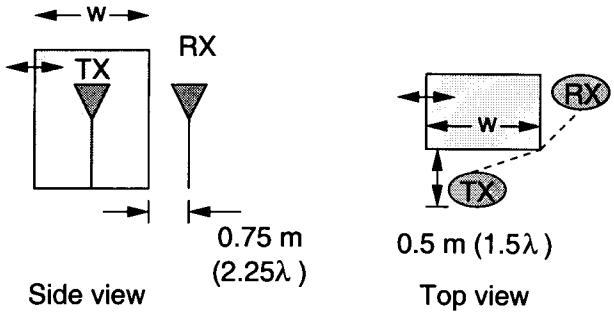

Figure 4.18: Spatial configuration used in Case C. The diffraction region is considered.

For accurate receiver placement in the FDTD simulation, it is useful to extend the FDTD domain via the Kirchhoff surface integral formulation (Section 2.2). Receiver placement is then not limited to FDTD grid point locations. To implement the Kirchhoff surface integral formulation in this case, the scatterer (wall), transmitter, and receiver are all enclosed by the surface of integration (Figure 4.20). Validation of the Kirchhoff surface integral implementation in this configuration is shown in Figure 4.21, where the results of Case A are reproduced using both the FDTD alone and the FDTD combined with the Kirchhoff transformation.

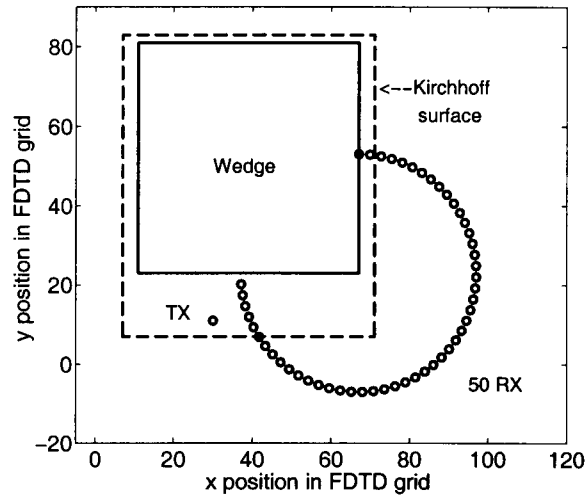

Figure 4.19: Top view of the FDTD method simulation space showing the diffracting wall and receiver placement. 50 receivers (circles) are spaced every 5.4° over the 270° arc. The transmitter location is also shown (cross).

Figure 4.22(a) shows the received signal generated by the combined FDTD/Kirchhoff technique for several different wall widths. In this simulation, the 50 receivers are placed at a radius of 0.75 m (2.25λ) from the diffracting corner. The magnitude of the diffracted signal in the incident field shadow region shows very little dependence on the wall width until the wall size is a small fraction of a wavelength, which agrees with results presented in [125, 126]. In Figure 4.22(b), the effect of carrier frequency on the simulation is considered. The overall amplitude is reduced, following the expected response of the envelope of the modulated carrier as shown in Figure 4.4(b). In Figure 4.22(c) diffraction effects over the top of the wall become significant, interfering with a meaningful evaluation of diffraction from the edge of the wall. This demonstrates the importance of running the simulation with a wall of sufficient height.

Results for diffraction in the shadow region found using the FDTD method are again comparable to results found using ray-tracing, with a mean squared error of $\sim$ 6.2% over the range of the incident field shadow region.

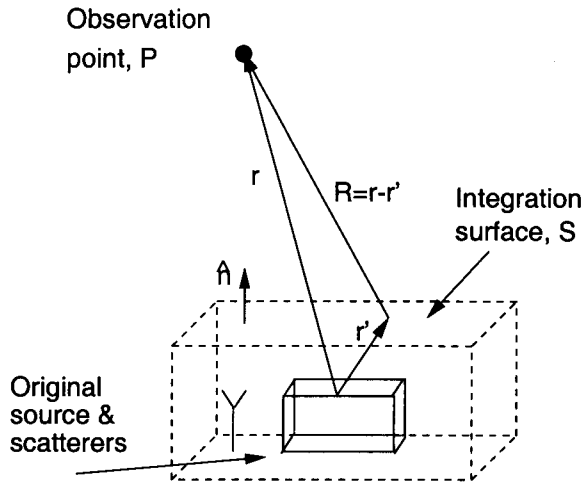

Figure 4.20: The location of source scatterers when the Kirchhoff surface integral formulation is used for indoor propagation modeling.

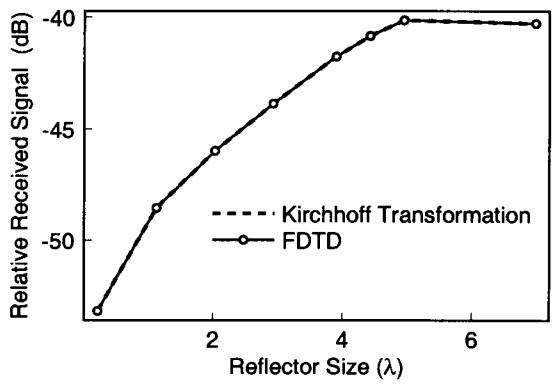

Figure 4.21: Validation of the Kirchhoff surface integral transformation for use in propagation modeling. Comparison is made between the FDTD method and the FDTD method combined with Kirchhoff in the configuration of Case A.

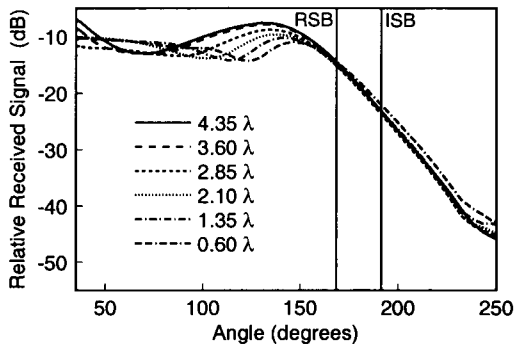

(a)

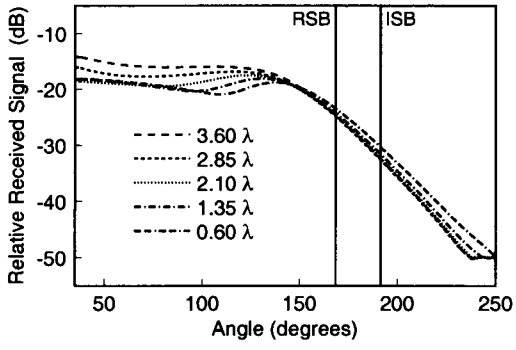

(b)

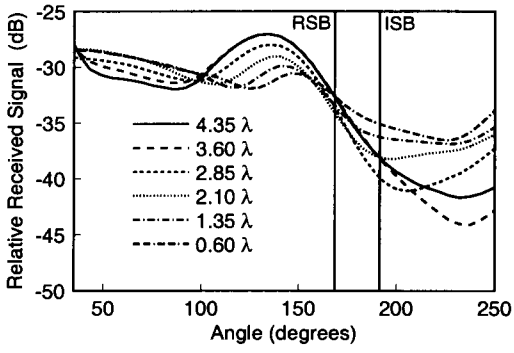

(c)

Figure 4.22: FDTD results in the diffraction region for a perfectly conducting wall of several different widths. In (a), the carrier frequency is 900MHz, in (b), the carrier frequency is 450MHz, and in (c) the carrier frequency is 900MHz, but the wall height is insufficient (3.2λ as opposed to 7.0λ for the case in (a)), yielding unusable data. RSB refers to the reflected field shadow boundary and ISB is the incident field shadow boundary.

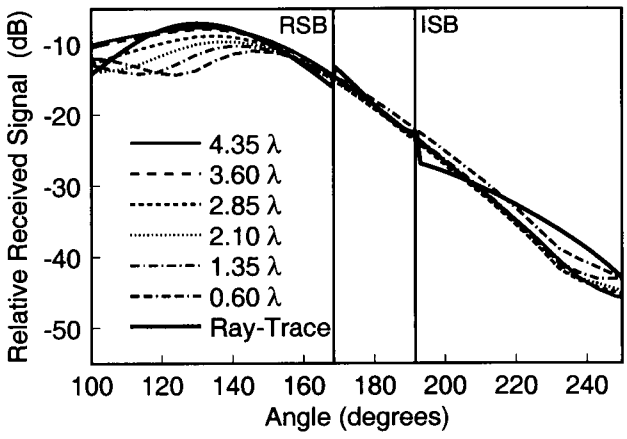

Figure 4.23: Comparison of the FDTD simulation shown in Figure 4.22(a) and the ray-tracing simulation.

4.5 Correction Terms for Diffraction from Dielectric Wedges

An important aspect of propagation modeling is the accurate determination of received signal strength for non-line-of-sight (NLOS) signals. NLOS conditions are frequently encountered in urban cellular/microcellular applications and in many indoor applications such as wireless LAN systems. The accurate determination of diffracted fields is therefore an essential component of any ray-tracing model. As discussed in Section 4.1, the geometrical theory of diffraction (GTD) [60] is the basis for diffraction modeling in many ray-tracing programs. The original GTD successfully treated diffraction from PEC wedges. This technique erroneously predicted discontinuities in the fields at the reflection and incident field shadow boundaries (RSB and ISB, respectively, defined in Figure 4.24). However, the development of the uniform theory of diffraction (UTD) [61] enabled accurate prediction of the fields in the transition regions between the illuminated and shadowed regions. In the UTD, the original GTD diffraction coefficients are multiplied by Fresnel integrals in the transition regions. Then, as the GTD fields become infinite at the shadow boundaries, the Fresnel integrals decrease toward zero, and the resulting field remains finite.

While diffraction modeling methodology for PEC wedges is well-established, the development of a uniform diffraction coefficient for wedges with finite conductivity is the subject of continuing research. A limited number of methods have been proposed. An asymptotic solution for diffraction from lossy wedges was originally developed by Maliuzhinets in 1953 [132]. Improvements to this technique, including development of a transition function for continuity at the reflection shadow boundaries, have been proposed in subsequent work [133]–[136]. This technique has not been widely incorporated into ray-tracing programs because the integration involved in determination of the diffraction coefficients can be difficult to evaluate except for certain wedge angles ($n = 1/2, 1, 3/2, 2$) [137].

A second method, proposed by Luebbers in 1984 [121], introduces a heuristic modification to the UTD equations. Fresnel reflection coefficients corresponding to the dielectric material of the diffracting wedge are incorporated into the UTD diffraction coefficient terms associated with the reflection field shadow boundary. Further discussion on this work can

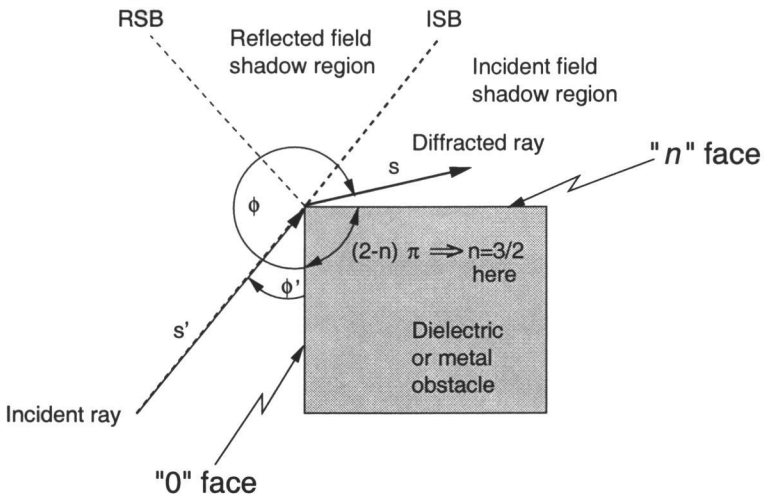

Figure 4.24: Geometry of the diffraction problem. The 90° (n=3/2) wedge problem is illustrated, with the "0" face and the "n" face denoted.

be found in Refs. [138, 137, 139]. The original formulation for this work appears in an earlier work by Burnside and Burgener (1983) [140] in which reflection and transmission coefficients are incorporated into the UTD diffraction coefficient equations for characterization of scattering by a thin lossless dielectric slab.

A third technique for development of uniform diffraction coefficients recently has been proposed by Stratis and Taflove [115]. The suggestion has been made to compile a library of numerically-generated diffraction coefficients derived from simulations carried out with the FDTD method. The library would provide a look-up table for a variety of materials and wedge shapes.

Because the Luebbers model can be easily implemented in a computer program, this formulation (D.2) is currently used in many ray-tracing propagation programs, e. g., [57, 117, 141, 142]. However, as discussed by Luebbers in Refs. [121, 139], the heuristic coefficients were developed for a limited set of applications, including, among other things, those with wedges having a large interior angle, with observation angles near shadow boundaries, and with observation angles greater than angles of incidence. In the present section, a heuristic improvement to the Luebbers coefficients is proposed, enabling accurate prediction of diffraction fields for a wide range of wedge angles and for any observation angle.

The improvement is developed by comparison to results generated with the combined FDTD/Kirchhoff method.

The chapter begins with a more detailed description of the Luebbers formulation and a discussion of the inaccuracies arising from the method when it is used for applications other than those for which it was intended. Simulation results are presented for several different dielectric materials. In Section 4.5.2, validation is presented for the use of the FDTD/Kirchhoff method in diffraction calculations by comparison to published data of scattering from an infinitely high, perfectly conducting square cylinder. The heuristic modification to the Luebbers coefficients is presented in Section 4.5.3, with validation given by comparison to FDTD method simulations. Results are presented for a 90° wedge including a variety of materials and for the entire range of angles of incidence.

4.5.1 Description of the Luebbers Formulation and Its Inherent Inaccuracies

To describe the Luebbers formulation for diffraction coefficients, consider a wedge with the interior angle defined by $(2-n)\pi$ (see Figure 4.24). For convenience, the diffraction coefficients given in Appendix D are repeated below. Fresnel reflection coefficients, such as those given in (4.4) and (4.5), which correspond to either the incidence face ("0" face) or the diffraction face ("n" face), are incorporated into the two UTD diffraction coefficients associated with the reflection shadow boundary (the terms with argument $(\phi + \phi')$ in (4.21)).

$$
\begin{aligned}
D_{\substack{\perp \\ \parallel}}(L,\phi,\phi') &= \frac{-e^{-j\pi/4}}{2n\sqrt{2\pi\beta}\sin\gamma_o'} \\
&\times \left[\cot\left(\frac{\pi+(\phi-\phi')}{2n}\right) F\left[\beta L a^+(\phi-\phi')\right]\right. \\
&+ \cot\left(\frac{\pi-(\phi-\phi')}{2n}\right) F\left[\beta L a^-(\phi-\phi')\right] \\
&+ R_{\substack{\perp \\ \parallel}}^0 \cot\left(\frac{\pi-(\phi+\phi')}{2n}\right) F\left[\beta L a^-(\phi+\phi')\right] \\
&+ \left. R_{\substack{\perp \\ \parallel}}^n \cot\left(\frac{\pi+(\phi+\phi')}{2n}\right) F\left[\beta L a^+(\phi+\phi')\right]\right]
\end{aligned}
\tag{4.20}
$$

Here, the terms R^0 and R^n are the reflection coefficients found in (4.4) and (4.5), where 0 refers to the illuminated wedge face (toward the incident field) and n refers to the diffraction face, as shown in Figure 4.24.

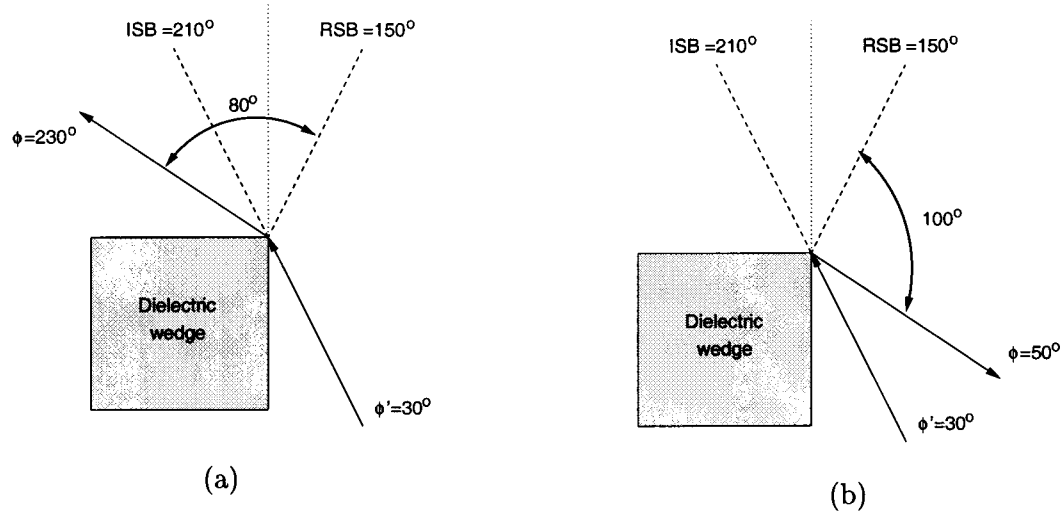

Figure 4.25: Diffraction from a dielectric wedge ($\sigma = 0.1$ S/m, $\epsilon_r = 15.0$) with angle of incidence, $\phi' = 30°$, and various angles of observation, ϕ: (a) $\phi' = 30°$ and $\phi = 230°$ (shadowed region), (b) $\phi' = 30°$ and $\phi = 50°$ (illuminated region).

The two diffraction coefficient terms with argument $\pi - (\phi + \phi')$ correspond to the RSB, as is now demonstrated. Consider the wedge shown in Figure 4.25(a), where a ray is incident on a diffracting corner at 30°. The RSB occurs at $180° - 30° = 150°$, and the ISB occurs at $180° + 30° = 210°$. For an observation point at $\phi = 230°$, the quantities

$$\pi - (\phi + \phi') = 180° - 260° = -80° \tag{4.21}$$

$$\pi + (\phi + \phi') = 180° + 260° = 440°, \quad (440° - 360° = 80°) \tag{4.22}$$

correspond to the angular distance between the observation point, ϕ, and the RSB.

The dielectric wedge shown in Figure 4.25(b) is now considered. The incident ray is still at an angle of 30°, but now the observation point is in the illuminated region, at

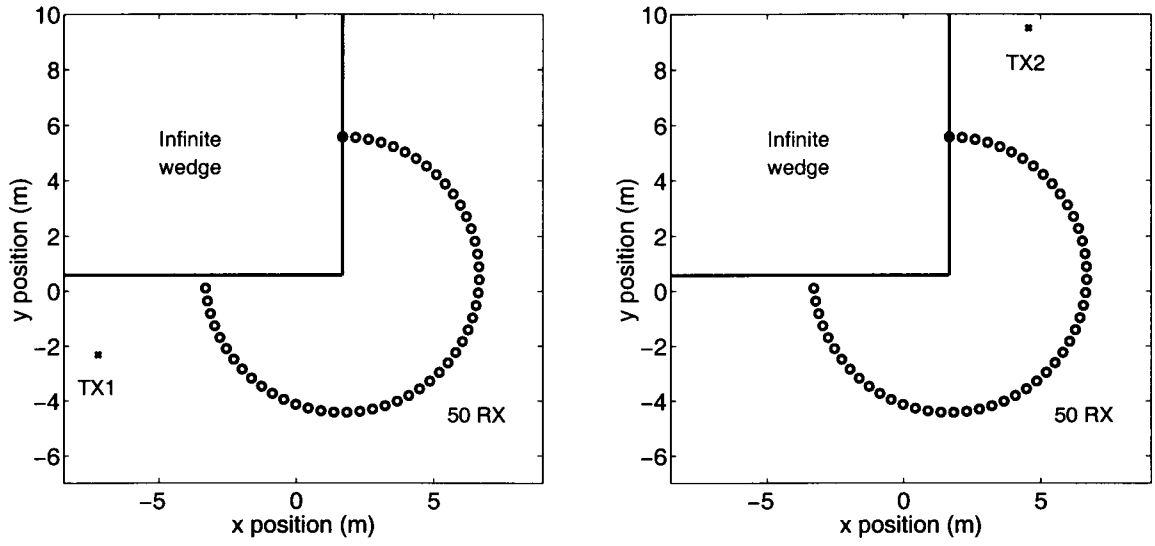

(a) (b)

Figure 4.26: Two configurations for comparing diffracted signals from an infinite wedge. 50 receivers are placed equidistant from the diffracting corner: (a) Transmitter at $\phi' = 22°$; (b) Transmitter $\phi' = 248°$.

$\phi = 50°$. The arguments of the diffraction coefficients are given by

$$\pi - (\phi + \phi') = 180° - 80° = 100° \tag{4.23}$$

$$\pi + (\phi + \phi') = 180° + 80° = -100° \tag{4.24}$$

These quantities correspond to the angular distance between ϕ and the RSB, but note the angles have the opposite sign compared to (4.21) and (4.22). From these examples, the relation $(\phi + \phi')$ may be thought of as corresponding to the RSB. The other two terms of 4.21 correspond to the ISB through the relation $(\phi - \phi')$.

The Luebbers coefficients can give inaccurate results for diffraction calculations for certain angles of incidence, as noted in [135]. As a demonstration, the total field found using ray-tracing is calculated for two infinite wedges made from a perfect electrical conductor (PEC) and from a lossy dielectric. In these simulations, observation points are located in a circular ring centered around the diffracting corner (Figure 4.26). The angle of incidence is 22° from either the 0 face ($\phi' = 22°$) or the n face ($\phi' = 248°$). Both the source and

observation point locations are in the far field ($s' = 28.0\text{m}$ ($\approx 84\lambda$), $s = 27.5\text{m}$ ($\approx 82.5\lambda$), for a frequency of 900MHz). The solution consists of direct, reflected, and diffracted rays.

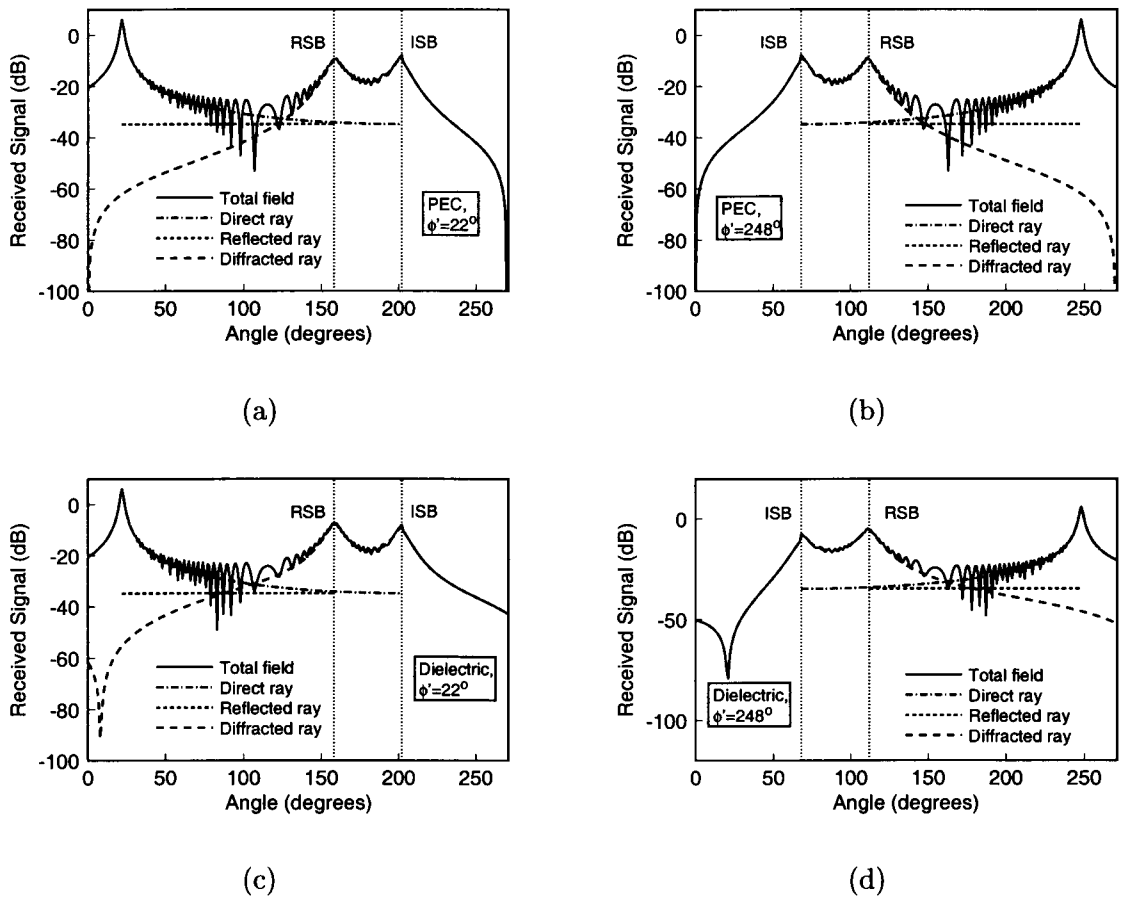

Figure 4.27: Comparison of the ray-tracing field components of the total field from a diffracting corner for a PEC wedge ($\sigma = 1.0e6$ S/m, $\epsilon_r = 1.0$) and a dielectric wedge ($\sigma = 0.1$ S/m, $\epsilon_r = 15.0$): (a) $\phi' = 22°$, PEC wedge; (b) $\phi' = 248°$, PEC wedge; (c) $\phi' = 22°$, dielectric wedge; and (d) $\phi' = 248°$, dielectric wedge. The dip in the diffracted ray in the illuminated region of (c) and the dip in the diffraction region of (d) are non-physical. Their elimination is the goal of the present work.

Figures 4.27(a)&(c) and 4.27(b)&(d) compare the ray-tracing calculations for the PEC and the dielectric wedge, respectively. As shown, the direct ray exists in the illuminated region up to the incident field shadow boundary (ISB). The specularly reflected ray exists in the illuminated region up to the reflected field shadow boundary (RSB), and

has a constant value since the total path length is constant for all receiver locations. The diffracted ray is generated for all receiver locations from $\phi = 0°$ to $\phi = 270°$. The interference pattern between the direct and reflected rays is apparent in the total received signal. In the reflected field shadow region, the total field is given by the combination of the direct and diffracted rays; in the incident field shadow region, the total received signal is given by the diffracted ray alone.

The dips occurring in the illuminated region in Figure 4.27(b) and in the diffraction region in Figure 4.27(d) are erroneous. The diffracted ray solution should be monotonically decreasing, as with the results shown in Figures 4.27(a)&(c). In the present formulation of the Luebbers coefficients [117] and in the formulation of [142], the inaccuracy in the illuminated region occurs when the angle of incidence is less than 180°. The inaccuracy in the shadowed region occurs when the angle of incidence is greater than 180°. However, other researchers [135, 136], have encountered the opposite effect, where the dip occurs in the diffraction region for $\phi' < 180°$. These discrepancies may be due to implementation of the diffraction coefficients. Note that when $\phi' < 180°$, the inaccuracy may not be apparent, since the direct and specularly reflected rays dominate the total received signal.

To eliminate the inaccuracy and increase the versatility of the Luebbers diffraction coefficients, a heuristic modification may be implemented by comparing the Luebbers results to diffraction field results calculated using the combined FDTD/Kirchhoff method. In the next section, validation of the FDTD/Kirchhoff method for use in diffraction problems is presented by comparison to published data. Then, in Section 4.5.3, the development of the heuristic improvement is presented.

4.5.2 Validation of the Combined FDTD/Kirchhoff Method for Use in Diffraction Problems

This section presents validation of the FDTD/Kirchhoff method for calculation of the fields in the diffraction region. A numerical experiment characterizing scattering from an infinitely high rectangular cylinder is considered. The geometry of the problem is given in Figure 4.28. This numerical experiment was first carried out for the case of parallel

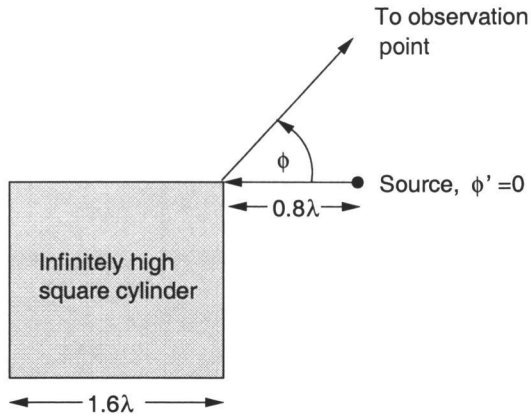

Figure 4.28: A cylindrical wave is incident on an infinitely high rectangular PEC cylinder at grazing incidence.

polarization in 1975 by Mautz and Harrington [126]. They compared results found using the GTD with results obtained with the MoM. The experiment was reproduced in 1997 by Holm [120] to demonstrate a higher order diffraction coefficient for use in the UTD. Holm used the 1975 results to validate his technique, and he extended the experiment to the case of perpendicular polarization. The results of Holm's experiment with perpendicular polarization are reproduced here to provide validation of the FDTD/Kirchhoff technique for use in diffraction modeling problems.

In the experiment (Figure 4.28), a vertical line source creates a cylindrical wave which is incident on one corner of a rectangular cylinder at grazing incidence, that is, $\phi' = 0°$. The source is located 0.8λ from the corner. The cylinder is square and is 1.6λ on a side. Observation points are located in the far field in a circular ring centered around the diffracting corner.

For the FDTD/Kirchhoff technique, the line source is approximated by a Hertzian dipole source. The simulation is essentially a 2-D case because the source and receivers are all in the same plane. Therefore, the wavefront is approximately cylindrical at the diffracting corner, and the use of the Hertzian dipole source is justified. The source is located 0.8λ (≈ 0.2664m) from the diffracting corner, with $\phi' = 0°$. Both sinewave excitation and a Gaussian-pulse-modulated excitation with carrier frequency of 900MHz are utilized. The

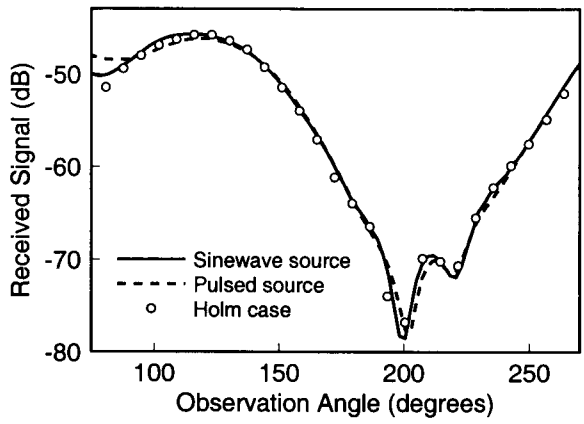

Figure 4.29: Comparison of results generated using the FDTD/Kirchhoff method and those published by Holm. Results from the FDTD/Kirchhoff method are presented with both sinewave and pulse-modulated excitation.

Gaussian pulse, $p(t)$, is given by:

$$p(n\Delta t) = e^{\left(\frac{n\Delta t - t_0}{\tau}\right)^2} \tag{4.25}$$

with pulse width $\tau = 0.915$ns, and delay time $t_0 = 4\tau = 3.66$ns. The FDTD grid cell dimensions, chosen according to the guidelines presented in Section 2.1.2, are $\Delta x = \Delta y =$ 0.025m, and $\Delta z = 0.075$m.

The infinitely high cylinder is approximated by a perfectly conducting square metal cylinder whose height (2.325m $\approx 7\lambda$) is much greater than the side dimension (0.525m $\approx 1.57\lambda$). The Kirchhoff transformation is used to find the field at receiver points spaced every 2.24° on a circle with a radius of 5m ($\approx 15\lambda$) centered around the diffracting corner (The configuration is similar to that shown in Figure 4.26). The distance of 15λ is in the far field, as demonstrated by an example in Section 3.2 (see Figure 3.3).

Results are shown in Figure 4.29 for the FDTD/Kirchhoff method with both sinewave excitation and pulsed excitation. These are compared to published results presented by Holm in [120]. The agreement between the FDTD/Kirchhoff method and Holm's results serves to validate the technique. Frequency dependence of the FDTD diffraction problem does not appear to be significant since results for the broadband pulse-modulated case are quite similar to the single-frequency case except in the deep shadow region.

4.5.3 Development of Heuristic Improvement Terms

The basis of the heuristic modification of the Luebbers formulation is the determination of the angle at which the Fresnel coefficients R^0 and R^n are calculated. In the Luebbers formulation, R^0 is calculated at $\theta_1 = \phi'$ and R^n is calculated at $\theta_2 = n\pi - \phi$. For a wedge with interior angle of 90°, commonly associated with objects in propagation modeling, $\theta_2 = 270° - \phi$. Additionally, in the Luebbers formulation, it is assumed that the angle of incidence, ϕ', is always greater than the angle of observation, ϕ.

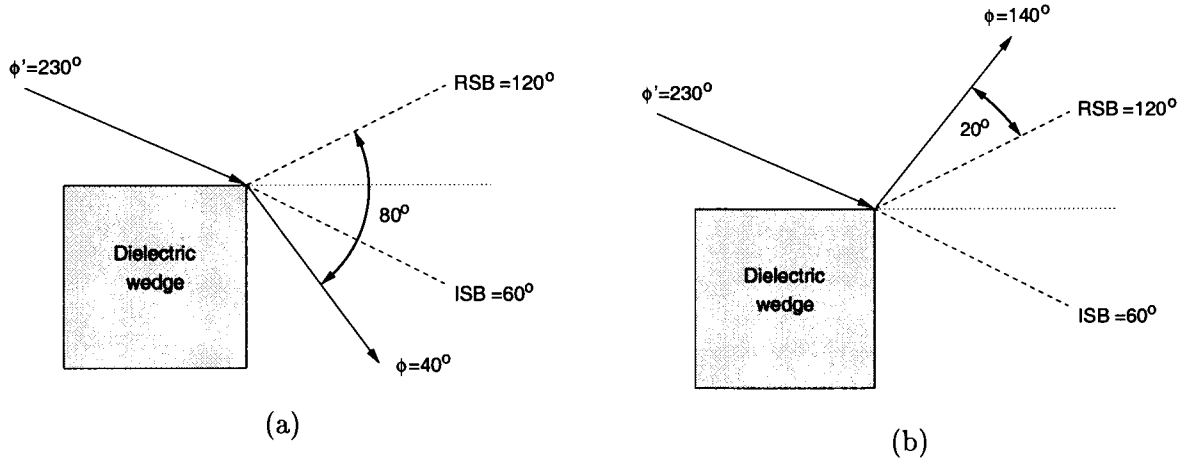

Figure 4.30: Diffraction from a dielectric wedge ($\sigma = 0.1$ S/m, $\epsilon_r = 15.0$) with angle of incidence, $\phi' = 230°$, and various angles of observation, ϕ: (a) $\phi' = 230°$ and $\phi = 40°$ (shadowed region), and (b) $\phi' = 230°$ and $\phi = 140°$ (illuminated region).

In the proposed heuristic modification of the Luebbers formulation, θ_1 remains dependent on ϕ', as in the original formulation. However, since the relationship between the observation point and the RSB depends on both ϕ and ϕ', the proposed modification contains the quantity $\phi + \phi'$.

Four different configurations of ϕ' and ϕ are considered in the present work. They depend on whether the angle of incidence is greater than or less than 180°, and whether the observation point, ϕ, is in the "illuminated" region (where $(\phi - \phi') < 180°$, i. e, smaller

Region	$\theta_{1,L}$	$\theta_{2,L}$	$\theta_{1,H}$	$\theta_{2,H}$
$\phi' < \pi$, illum., Fig. 4.25(a)	ϕ'	$n\pi - \phi$	$-\phi'$	$-(\phi + \phi')$
$\phi' < \pi$, shadow, Fig. 4.25(b)	ϕ'	$n\pi - \phi$	ϕ'	$n\pi - (\phi + \phi')$
$\phi' > \pi$, illum., Fig. 4.30(a)	ϕ'	$n\pi - \phi$	ϕ'	$n\pi - (\phi + \phi')$
$\phi' > \pi$, shadow, Fig. 4.30(b)	ϕ'	$n\pi - \phi$	$n\pi - \phi'$	ϕ

Table 4.2: Comparison of the Luebbers coefficients ($\theta_{1,2,L}$) and the heuristic modification ($\theta_{1,2,H}$).

than the angle of the ISB) or in the "shadow" region, where ϕ is greater than the angle of the ISB. A summary of the Luebbers formulation values for θ_1 and θ_2, and the proposed modification for these four cases is given in Table 4.2. An example of each case is given in Figures 4.25(a)&(b) and Figures 4.30(a)&(b). Note that the Luebbers formulation is not valid for angles of incidence greater than angles of observation. Corresponding to the difference in sign noted between (4.21)/(4.22) and (4.23)/(4.24), $\theta_{1,H}$ and $\theta_{2,H}$ have different signs depending on whether they are in the illuminated or shadowed region.

The proposed modification to the Luebbers coefficients has been implemented, and simulation results are presented in Figures 4.31(a)-(d). The different components of the ray-tracing signal are shown without and with the improvement in place. With the improvement in place, the diffracted rays are always monotonically decreasing away from the shadow boundaries as, theoretically, they should be. Figure 4.32(a)-(f) shows the diffracted ray solution with and without the improvement terms for angles of incidence ranging from 5° to 265°. In each case, the dielectric wedge has $\sigma = 0.1$ S/m, $\epsilon_r = 15.0$, $s' = 28.0$m ($\approx 84\lambda$), $s = 27.5$m ($\approx 82.5\lambda$), and the frequency is 900MHz.

To validate the improvement terms, comparison is made to simulations carried out with the FDTD/Kirchhoff technique in the incident field shadow region. To approximate an infinite wedge, the transmitter and receivers are placed close enough to the wedge to prevent diffraction around the back of the wedge for the duration of the simulation. Transmission

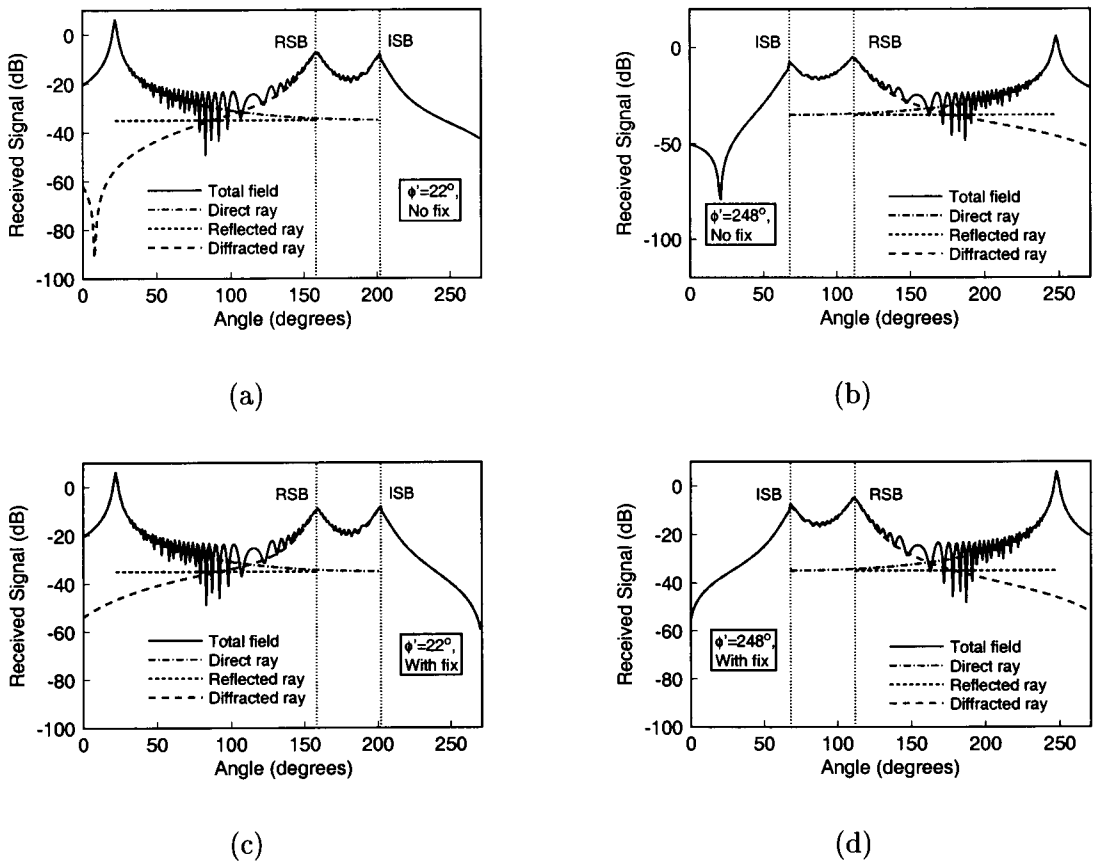

Figure 4.31: The components of the total field from a diffracting dielectric corner with $\sigma = 0.1$ S/m, $\epsilon_r = 15.0$. (a) $\phi' = 22°$, no fix, (b) $\phi' = 248°$, no fix (c) $\phi' = 22°$, with fix and (d) $\phi' = 248°$, with fix.

through the dielectric material is not significant, as determined by examination of mesh field plots from the FDTD simulations. The configuration shown in Figure 4.19 on page 76 is used, with 50 receiver points located in a circular ring with a radius of 0.75m (2.25λ) centered around the diffracting corner. The Kirchhoff surface integral formulation is used to determine the field at the observation points. Note that some of the observation points are located within the Kirchhoff surface and must be disregarded. The FDTD/Kirchhoff solution is valid up to approximately 260°. The transmitter is located 0.8m (2.4λ) from the corner. The FDTD grid cell dimensions are again $\Delta x = \Delta y = 0.025$m and $\Delta z = 0.075$m. The overall grid size is 79x91x50. The large y-dimension is required to ensure that there is no diffraction around the back side of the dielectric wedge.

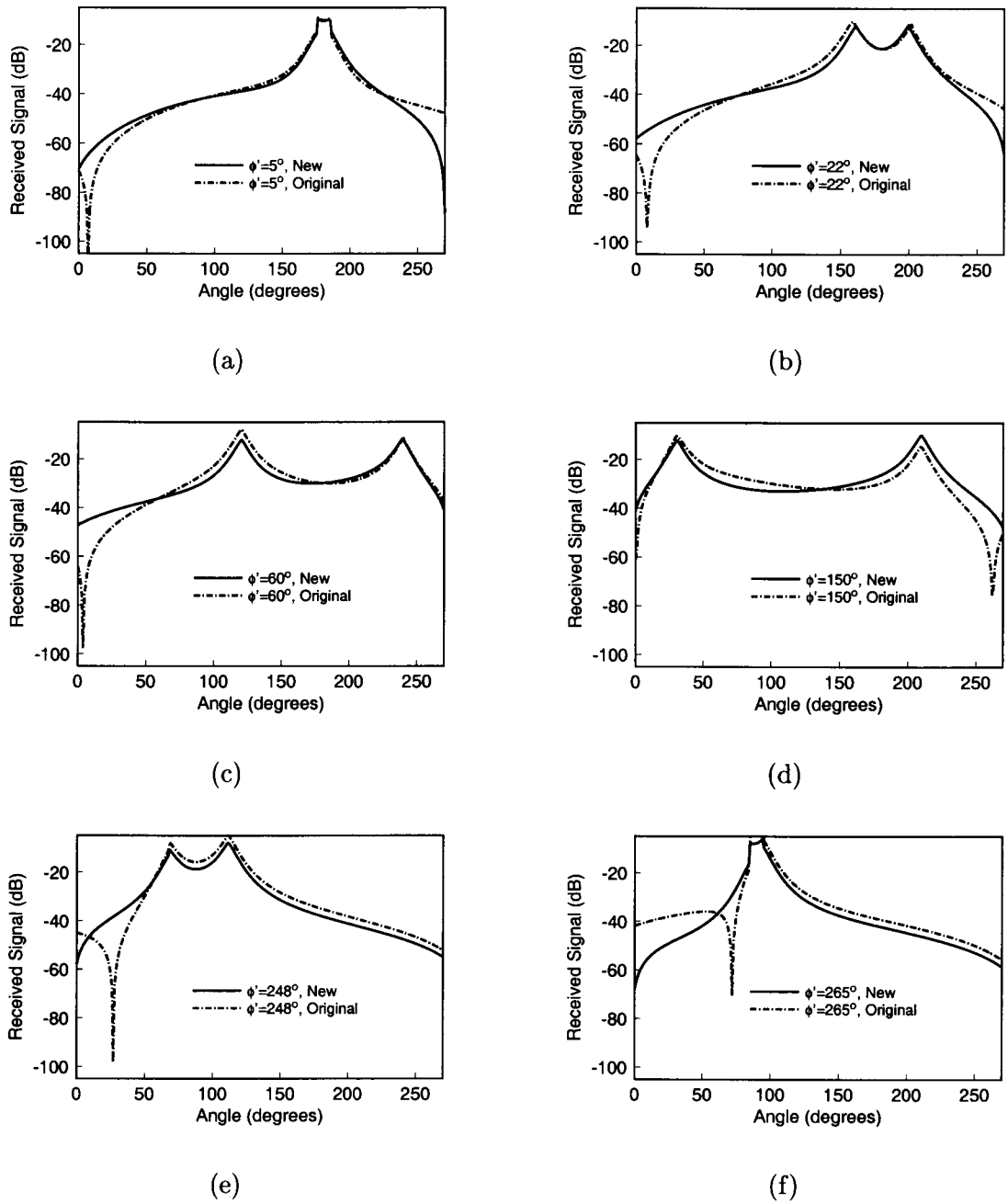

Figure 4.32: Comparison of the new (modified) and original Luebbers diffraction coefficients for a wide range of incident angles: (a) $\phi' = 5°$, (b) $\phi' = 22°$, (c) $\phi' = 60°$, (d) $\phi' = 150°$, (e) $\phi' = 248°$, (f) $\phi' = 265°$. Note that the modified coefficients have smooth and monotonically decreasing magnitude away from the shadow boundaries.

Figures 4.33(a)-(c) and 4.34(a)-(c) compare the FDTD method results with the ray-tracing results in the diffraction region for $\phi' = 22°$ and for $\phi' = 248°$ respectively. Comparison is made with and without the improvement terms for three different materials. The PEC case (a), with $\sigma = 1.0\text{x}10^6$ S/m, $\epsilon_r = 1.0$, is compared to two dielectric materials: case (b), with $\sigma = 0.1$ S/m, $\epsilon_r = 15.0$, and case (c), with $\sigma = 0.001$ S/m, $\epsilon_r = 3.4$, with a frequency of 900MHz in each case. For the cases shown in Figures 4.33(a)-(c), $s' = 0.8$m ($\approx 2.4\lambda$), $s = 0.75$m ($\approx 2.25\lambda$). The curves corresponding to the original Luebbers formulation in Figures 4.34(a)-(c) were calculated at ten times these distances ($s' = 8.0$m and $s = 7.5$m) to better illustrate the dip effect, which becomes more pronounced at larger distances.

The PEC cases in Figure 4.33(a) and in Figure 4.34(a) represent the original UTD formulation, and therefore, no difference between the original and new ray-tracing representations is expected. The comparison of the curves generated by the FDTD method and the ray-tracing technique for the PEC case represents the fundamental level of accuracy which can be expected when comparing these two computational methods in diffraction calculations. The improvement in the ray-tracing cases with $\phi' = 248°$ (Figure 4.34(b)&(c)) is readily apparent, since the dip in the diffraction region has been eliminated. For the cases with $\phi' = 22°$ (Figure 4.33(b)&(c)), note that the slope of the diffraction coefficient with the original formulation is shallower than that of the FDTD method case. The results obtained with the original formulation differ by more than 5 dB from those produced by the new formulation for some observation angles for the angular range shown, and are even worse in the deep diffraction region ($\phi > 260°$), as can be readily seen in a comparison of the diffraction region slopes in Figures (4.31)(a) and (4.31)(c).

This implementation of the heuristically modified Luebbers diffraction coefficients requires only a simple modification of the original computer code, i. e., the inclusion of two conditional statements. Therefore, it is still computationally efficient when compared to the original implementation. Additionally, the proposed modification provides increased accuracy in both the diffraction and illuminated regions, and it enables simulations over a wider range of angles than does the original formulation.

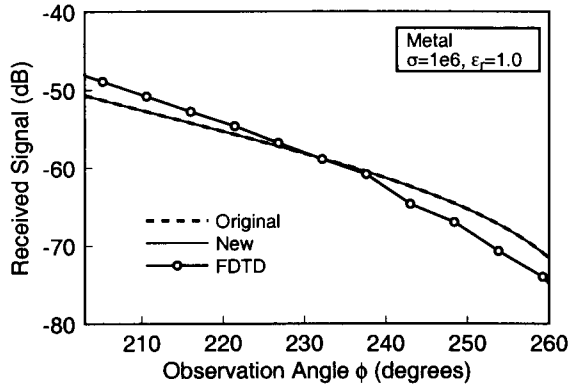

(a)

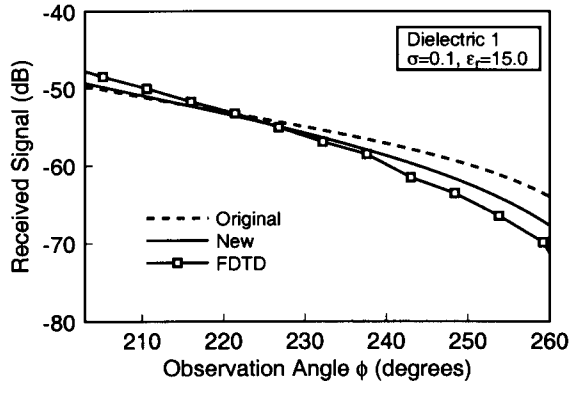

(b)

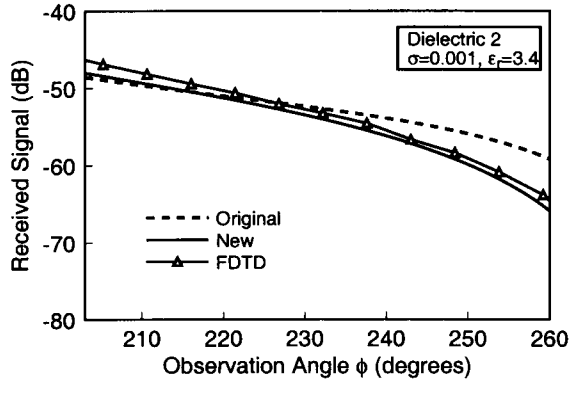

(c)

Figure 4.33: Comparison of the original Luebbers formulation, the heuristic improvement, and the combined FDTD/Kirchhoff method for $\phi' = 22°$ with (a) metal $\sigma = 1.0\text{x}10^6, \epsilon_r = 1.0$; (b) dielectric with $\sigma = 0.1, \epsilon_r = 15.0$; and (c) dielectric with $\sigma = 0.001, \epsilon_r = 3.4$.

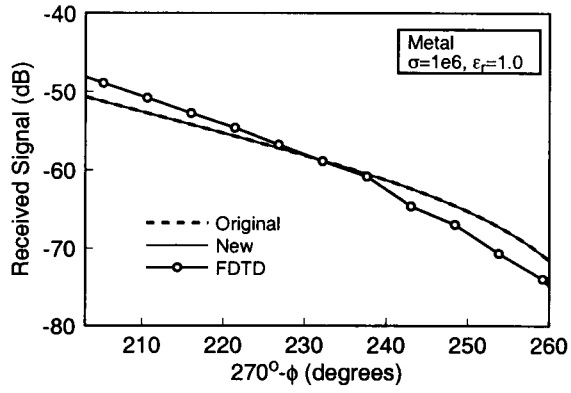

(a)

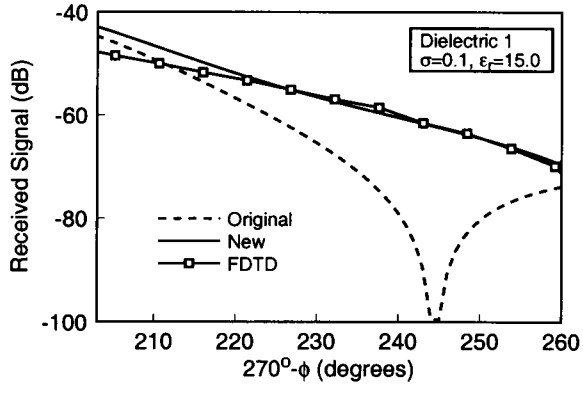

(b)

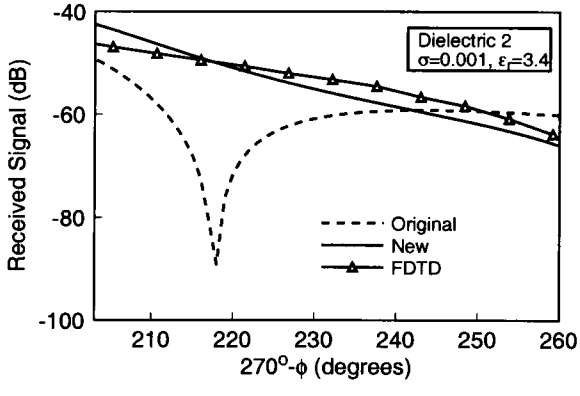

(c)

Figure 4.34: Comparison of the original Luebbers formulation, the heuristic improvement, and the combined FDTD/Kirchhoff method for $\phi' = 248°$ with (a) metal $\sigma = 1.0\text{x}10^6, \epsilon_r = 1.0$; (b) dielectric with $\sigma = 0.1, \epsilon_r = 15.0$; and (c) dielectric with $\sigma = 0.001, \epsilon_r = 3.4$.

4.6 Conclusion

In this chapter, the accuracy of the ray-tracing method for indoor propagation modeling was investigated. First the fundamentals of the ray-tracing technique were reviewed, including derivations of the direct, reflected, and diffracted ray propagation primitives. Then, some of the key parameters used in describing multipath signal propagation were defined. An example was next presented to illustrate implementation aspects of both ray-tracing and the FDTD method in indoor propagation modeling. A simple multipath environment was simulated and the use of each computational technique to determine the power delay profile was discussed.

In Section 4.4, a numerical experiment was carried out to investigate the accuracy of the ray-tracing method for local scatterer sizes approaching the wavelength of operation. Simulations were carried out for three different cases involving 1) diffraction and specular reflection, 2) diffraction and "non-specular" reflection, and 3) diffraction only. The received signal predicted by the ray-tracing method was compared to results generated using the FDTD and the combined FDTD/Kirchhoff methods. Results demonstrated the accuracy of the ray-tracing method for scatterer sizes down to a fraction of a wavelength when the phase of the received rays for small scatterers was accounted for. An explanation for the ray-tracing results was provided in terms of the path length difference between the diffracted and reflected rays.

Finally, the heuristic development of improvement terms for a set of diffraction coefficients that are often utilized in ray-tracing models was presented. The Luebbers coefficients are commonly used to characterize diffraction from dielectric wedges. They were originally developed for use in a limited set of diffraction applications, and have inherent inaccuracies when used otherwise. The proposed improvement terms eliminate some of the inaccuracies and thus enable the use of the Luebbers coefficients for a wider range of propagation modeling problems, especially in indoor environments. Throughout Chapter 4, the use of the combined FDTD/Kirchhoff technique has provided a standard against which the ray-tracing technique can be both evaluated and improved upon.

5. CONCLUSIONS AND SUGGESTIONS FOR FURTHER WORK

In this final chapter, the main points presented in the thesis are briefly summarized, and the more significant contributions of this work are discussed. The motivation behind the development of the combined FDTD/Kirchhoff technique and its applicability to various simulation scenarios is discussed. Examples taken from the thesis demonstrate the advantages and disadvantages of this technique. Next, the use of computationally intensive techniques such as the combined FDTD/Kirchhoff method as standards to assist in the assessment, improvement, and development of more computationally efficient methods for device characterization is discussed. The thesis has presented several examples of this comparison-oriented use of the combined FDTD/Kirchhoff technique, and some of the important contributions arising from this methodology are highlighted. In the final section, potential avenues of exploration for further research work are considered.

5.1 Conclusions

The goal of the thesis has been to develop improvements, either in accuracy or in efficiency, in the modeling of a class of electromagnetic (EM) radiative systems that can be readily characterized using the FDTD technique. These systems include those with non-time-harmonic excitation, those with a distributed source of excitation, and those which contain a variety of material parameters. Additionally, radiative systems from which broadband characteristics are of interest, such as the impulse response of wireless communication systems, may be modeled directly in the time domain. The computational technique developed in this thesis, the combined FDTD/Kirchhoff method, is versatile enough to accurately predict EM radiation from all of the above mentioned systems, and it can do so for near- and far-field observation points. It is complementary to the well-established FDTD technique, and in many cases it improves the efficiency and/or the accuracy of the FDTD method. Because of the computational intensity of the combined FDTD/Kirchhoff method, it is not practical for use as a commercial design tool. However, because it provides very accurate solutions, it may be used in the development of other, more computationally

efficient techniques by acting as a standard against which other techniques can be validated and/or verified.

The main points examined in the thesis will be discussed in this section. They fall into two broad topic areas: The advantages and disadvantages in the application of the combined FDTD/Kirchhoff computational technique to various modeling problems, and the use of the FDTD/Kirchhoff technique to develop and/or improve other, more efficient, computational techniques.

5.1.1 The Combined FDTD/Kirchhoff Technique

As demonstrated in several examples in this thesis, the combination of the FDTD method with a spatial transformation technique enables characterization of EM radiation from a wider variety of systems than does the use of the FDTD method alone. In the present work, the FDTD method was combined with the scalar Kirchhoff integral formulation [30, 31, 21] as opposed to other spatial transformation techniques based on equivalent surface current source terms [41, 40, 44, 45]. This choice was made because the Kirchhoff integral requires no interpolation between electric and magnetic equivalent source terms in the FDTD implementation, a necessary feature of the other techniques. The following discussion will refer to the combined FDTD/Kirchhoff method. However, the points raised would generally apply to the combination of the FDTD with other spatial transformation techniques.

One primary advantage of the combined FDTD/Kirchhoff method over the use of the FDTD alone is the ability to find the fields at locations far removed from the FDTD computational domain. This was demonstrated in Chapter 3, where the far-field radiation from a photoconducting structure was modeled. The high level of detail required to accurately model the inhomogeneous regions of current/field interaction in the photoconducting structure would have necessitated an unreasonably large FDTD grid for observation points in the far field. FDTD/Kirchhoff simulation results for the far-field radiation demonstrated that the pulsewidth of the excitation as compared to transit time through the device is important in design because significant distortion of the received signal can occur.

Another advantage of combining the FDTD method with a spatial transformation such as the Kirchhoff surface integral is that it allows determination of fields at analytically specified observation points, i. e., there is no restriction to FDTD grid cell locations as points of observation. While interpolation between FDTD grid points is possible, the use of the spatial transformation enables easy specification of arbitrary observation points, such as the ring of 50 receivers used in the diffraction modeling problems of Sections 4.4 and 4.5.

A further advantage the combined FDTD/Kirchhoff technique over utilization of the FDTD method alone is that EM waves need to propagate no farther through the FDTD grid than to the integration surface. This can reduce the effects of grid dispersion, an artifact of the FDTD method which can introduce errors into phase and time delays of signals that propagate long distances through the FDTD grid. An example of this was given in Section 2.1.3 on page 11, where a sinusoidal signal that had propagated approximately 6λ through the FDTD grid developed a delay time error of more than 0.56%.

Combined FDTD/spatial transformation techniques also have disadvantages. The requirement that the integration surface be in a homogeneous problem space means that all interacting surfaces need to be enclosed (or, equivalently, that all significant surface fields be contained on a single quasi-infinite plane). This can create the need for an unreasonably large FDTD computational domain in order to "capture" all important field/surface interactions as, for example, reflections off a wall or floor. This effect was exemplified in Section 4.4, where it was necessary to utilize a large computational domain and unequal grid spacing to simulate an infinitely high diffracting wedge (see Figure 4.22(c)). Application of the Kirchhoff surface integral requires that the integration surface be located in a homogeneous medium, i. e., external to the wedge, further increasing the size of the computational domain.

Another limitation of combined FDTD/spatial transformation techniques is the restriction on secondary interactions. The field at the observation point cannot, at present, easily be used as a secondary source to generate a further interaction. The FDTD technique used alone does not suffer from this problem, since the fields at each grid cell location

are components of the full-wave solution and may be used, in turn, to generate further interactions. Suggestions for alleviating this limitation in the spatial transformation include the use of equivalent source techniques, such as those proposed independently by Taflove and Umashankar [79, 44] and Merewether et al. [143] as well as the use of multiple FDTD simulation spaces [36, 37]. To date, however, an efficient method has not been presented in the literature. This topic will be discussed in more detail in Section 5.2.

5.1.2 Using the FDTD/Kirchhoff Technique to Assess, Improve, and Develop Other Computational Methods

While the combination of the spatial transformation with the FDTD method can increase the efficiency of the latter, this full-wave simulation technique still tends to be computationally intensive compared to other techniques based on approximations. As was demonstrated in several examples in this thesis, the FDTD/Kirchhoff method can be used to validate, improve, and develop approximate computational techniques. Some of these examples will now be discussed.

In Chapter 3, the far-field approximation was assessed for use in modeling radiation from a photoconducting structure by comparing it to the FDTD/Kirchhoff technique. The far-field approximation is commonly used for modeling radiation from free-space antennas, and has been proposed for use in modeling the radiation from photoconducting structures [13, 14, 66]. In the far-field approximation, only the dominant term is retained in the equations that describe the fields arising from a dipole source, e. g., (2.20). Propagation in a homogeneous problem space is assumed in the far-field approximation, and this was found to be a significant source of error in modeling the radiation from a photoconducting structure when compared to the modeling results obtained using the combined FDTD/Kirchhoff technique.

Inclusion of inhomogeneous material parameters in the characterization of the far-field radiation from the photoconducting structure led to the development of a computationally efficient model for the radiation from within the substrate. This approximate method was developed by considering the edges of the substrate as secondary diffract-

ing sources and replacing the substrate material by equivalent Hertzian dipole sources. When compared to results from the combined FDTD/Kirchhoff method, the approximate technique was found to accurately reproduce the effects of the substrate material on the far-field radiation. These simulations demonstrated that distortion can be significant for pulse widths on the order of 1/3 the transit time across the substrate to the diffracting edges.

In Chapter 4, the combined FDTD/Kirchhoff method was used to assess the accuracy of the ray-tracing technique as local scatterer size approaches the wavelength of operation, a situation often found in indoor wireless communication environments. The ray-tracing technique is a high frequency approximation in which EM waves are assumed to propagate as rays, that is, as narrow cylinders with constant cross-sectional phase and amplitude. The high frequency approximation means that the wavelength is assumed to be much smaller than objects in the propagation environment, and, hence, ray interactions such as diffractions and reflections are assumed to be independent of each other.

A numerical experiment was carried out in Section 4.4 in which the width of an infinitely thick wall was incrementally decreased to quantify the accuracy of the ray-tracing method. The wall generated three ray interactions: one reflection and two diffractions. Use of the relative phase method, in which the phase of nearby ray interactions is accounted for in the total received signal, allowed a comparison of ray-tracing results to those obtained by use of the combined FDTD/Kirchhoff method. It was shown that the ray-tracing method can accurately represent the received signal for scatterer sizes down to a fraction of a wavelength. This experiment demonstrates the importance of incorporating the phase of the received rays in the total received signal. Additionally, it provides confidence in the ray-tracing method for modeling systems in which objects approach the wavelength of operation such as is commonly found in indoor propagation environments.

Finally, in Section 4.5, improvement terms were developed for a set of coefficients commonly used in ray-tracing to model diffraction effects from dielectric objects. The so-called Luebbers coefficients were heuristically developed by Raymond Luebbers in 1984 [121] for characterization of fields for a limited class of diffraction problems. The original

Luebbers formulation was restricted to the characterization of wedges with a large interior angle, to cases with observation points near the shadow boundaries, and to cases where the angle of incidence is less than the angle of observation. In recent years, the Luebbers coefficients have been adopted for use in many ray-tracing programs, e. g., [57, 117, 141, 142]. In many cases, these coefficients have been shown to provide adequate solutions for diffraction fields from dielectric wedges even when the restrictions mentioned above are not met. Currently, computationally efficient alternatives which can be easily incorporated into ray-tracing programs do not exist.

A set of heuristically derived modifications to Luebbers' original diffraction coefficients was presented in Section 4.5. These modifications were developed by comparison of the diffraction fields predicted by the modified ray-tracing algorithm to the diffraction fields found using the FDTD/Kirchhoff technique. The new set of coefficients improve the accuracy in modeling dielectric wedge diffraction for any angle of incidence or observation (see Figures 4.32(a)-(f)) and for a wide range of dielectric materials with finite conductivity (see Figures 4.33(a)-(c) and 4.34(a)-(c)).

In summary, the use of the combined FDTD/Kirchhoff technique has proven advantageous in a number of time domain modeling problems for radiative EM fields. The technique is often more accurate and/or efficient than the use of the FDTD method alone. Further, its use as a standard against which other, more computationally efficient techniques can be assessed, improved, and developed is a great asset.

5.2 Suggestions for Future Work

Several of the topics discussed in this thesis would provide opportunities for further research. Three broad categories, based on Chapters 2-4 of the thesis, may be defined as potential areas for further development:

1. Improvements to the implementation of the combined FDTD/Kirchhoff method

2. Improvements in modeling radiation from the photoconducting structure and other ultrafast electronic devices

3. Improvements in propagation modeling

Some suggestions for addressing these topics are presented in the following sections.

5.2.1 Improvements to the Implementation of the Combined FDTD/Kirchhoff Technique

The combination of the Kirchhoff spatial transformation with the FDTD method presented in this thesis extends the work of DeMoer and DeZutter [21] to include multiple observation points. In this extension, the Kirchhoff integral is iteratively solved for each observation point at each timestep. The development of a computationally efficient algorithm for the case involving multiple observation points is an area in which further research is needed. Incorporation of a simple parallel processing routine could greatly enhance efficiency, as would the use of precalculated surface or observation point field values for a given configuration. The latter may be applicable when observation points share certain Cartesian coordinates, as in the cases of Sections 4.4 and 4.5 where the receivers are all located in a plane. In these cases, calculations made for certain field components at one observation point could subsequently be utilized by all observation points.

The present work was implemented as a modification of an FDTD method code already in existence. Presumably this is the case for many such spatial transformation implementations [21, 35, 42]. The development of a combined FDTD/Kirchhoff method code with well-integrated initialization and calculation routines and with a carefully designed user interface would shorten computation times and increase efficiency.

5.2.2 Improvements in Modeling Radiation from Photoconducting Structures and other Ultrafast Electronic Devices

Several areas relating to the modeling of radiative effects from ultrafast devices would provide opportunities for further research. Some of these are discussed below.

5.2.2.1 Extension of Radiation Modeling to Other Structures

The simulation results presented in the thesis compare favorably with published data, such as that presented in [91]. This work could readily be extended by compari-

son to published results with other structures such as those presented in [99] or through collaborative efforts with other research groups. The versatility of the PMC-3D and the combined FDTD/Kirchhoff technique would enable characterization of a wide range of device structures.

5.2.2.2 Incorporation of the Spatial Transformation into the PMC-3D

The implementation of the Kirchhoff spatial transformation for characterization of the far-field radiation from a photoconducting structure was carried out as an extension of an existing computer code. In this extension, the far-field radiation is calculated in a "post-processing" step. The current density found from an external simulation is used as excitation for a Hertzian dipole (or array of Hertzian dipoles) embedded in the GaAs substrate. The radiation arising from the dipole source is then transformed to the far field with the Kirchhoff surface integral formulation. The external simulation is provided by the PMC-3D computer code, introduced in Section 3.1. Incorporation of the Kirchhoff surface integral formulation into the PMC-3D would increase both accuracy and efficiency of the far-field radiation model. It would eliminate the approximation of the source as a Hertzian dipole or array of dipoles, increasing accuracy. Further, it would eliminate the post-processing calculation routine, increasing efficiency.

5.2.2.3 Improvement of the Computationally Efficient Model for Radiation from the Photoconducting Device

The development of a model for characterization of broadband radiation by substituting secondary sources for diffraction fields arising from the edges of the substrate material was presented in Chapter 3. This model could readily be extended to characterize reradiation from other materials (such as the metal electrodes). A further improvement to this model would enable implicit representation of the far-field radiation by monitoring points on the edges of the substrate or other relevant diffracting locations.

5.2.2.4 *Incorporation of Frequency-Dependent Material Parameters*

For the photoconducting structure model presented in Chapter 3 and for other ultrafast device models, incorporation of frequency-dependent permittivity ($\epsilon(\omega)$) is important. The frequency-dependence of the GaAs substrate material is well documented [144]. Similarly, accurate implementation of the metal electrodes may require incorporation of frequency-dependent conductivity. In general, implementation of frequency-dependent materials is difficult in time domain computational methods, but various alternatives have been proposed. One basic technique involves Fourier transformation of a known $\epsilon(\omega)$ to the time domain, and subsequent convolution of $\epsilon(t)$ with the appropriate field quantities in the FDTD equations. For example, the discretized Maxwell's equation for E_z would be written

$$\epsilon(t) \otimes \frac{\partial E_z}{\partial t} = \left(\frac{\partial H_y}{\partial x} - \frac{\partial H_x}{\partial y} \right) - J_z \tag{5.1}$$

where

$$\epsilon(t) = \mathcal{F}^{-1}\epsilon(\omega) \tag{5.2}$$

and F^{-1} is the inverse Fourier transformation operation.

The development of computationally efficient methods for implementing both complex impedance materials and numerical convolution procedures are topics of current research. These methods could be incorporated into the PMC-3D code.

5.2.3 Improvements in Propagation Modeling

Interesting areas for further research in propagation modeling include an extension of the FDTD/Kirchhoff technique to allow multiple interactions and the development of a physical basis for the improvements to the Luebbers diffraction coefficients.

5.2.3.1 *Development of a Technique to Model Multiple Scattering Interactions*

As discussed in Section 5.1, one drawback of the use of spatial transformation techniques is that the received field cannot easily be used as a secondary source to generate a subsequent interaction. The FDTD method does not suffer from this limitation because

field/object interaction occurs naturally in the FDTD algorithm, as shown in Figure 5.1. It would seem that a comparable use of the combined FDTD/Kirchhoff technique to find secondary interactions would be viable because the FDTD/Kirchhoff method can provide all six scalar field components at each timestep, as does the FDTD method. The development of such a technique would be of great benefit in, for example, propagation modeling because the transmitter could be located far from scatterers, which could, in turn, be located far from receivers. One possible method for modeling secondary interactions is briefly outlined below and the difficulties encountered in its implementation are discussed. The technique has been the subject of substantial research for the present work, but because of the inherent limitations in the method, has not as yet proved useful in propagation modeling.

The proposed technique is an extension of the "total field/scattered field" method proposed independently by Taflove and Umashankar [79, 44] and Merewether et al. [143]. Both formulations proposed by these researchers utilize an equivalent Huygens' surface source to specify the field resulting from an external source that is incident on the FDTD problem space (see Figure 5.2). Analytical expressions for an incident plane wave field are incorporated into the FDTD grid surrounding a scatterer in such a way that, while the total field (incident and scattered) exists inside the surface, only the field due to the interaction with the scatterer exists outside the surface.

In the proposed extension of this technique, a Kirchhoff integration surface surrounding the Huygens' surface transforms the scattered field to an external observation point (Figure 5.3). This would enable placement of a transmitter far from the FDTD grid, and, through use of the Kirchhoff transformations, would permit arbitrary receiver placement. In a further extension proposed in [36, 37], multiple FDTD grids are used to develop both the primary and secondary interactions (Figure 5.4). This is an interesting proposal. However, satisfactory simulations results have not yet been published.

Currently there are two primary limitations on these proposed techniques. One limitation is that the use of an equivalent Huygens' surface source requires a much higher degree of discretization than is required by the FDTD technique alone. For example, Taflove and

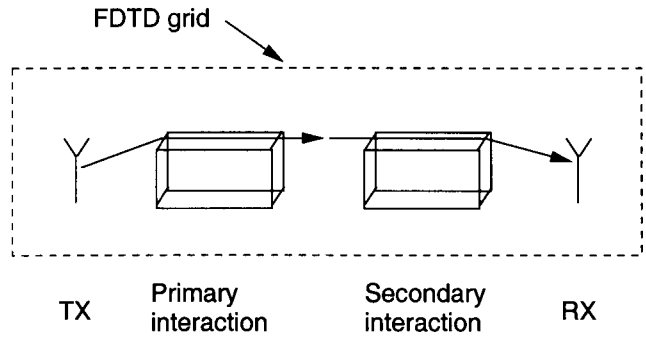

Figure 5.1: Secondary interactions in the FDTD method arise naturally from object/field interactions.

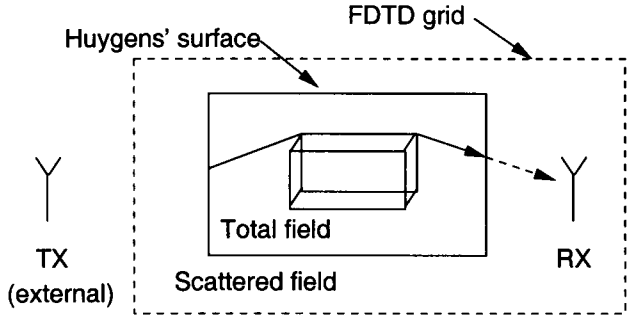

Figure 5.2: The total field/scattered field formulation.

Umashankar [44] compute the surface currents on an infinitely high square metal cylinder using the equivalent surface source technique. Their FDTD grid discretization is smaller than $\lambda/60$, impractical for most EM field calculations. The second limitation on the technique is the computational burden necessitated by calculation of all six scalar field components at locations surrounding a scatterer. Again, parallel implementation could relieve the computational burden, or possibly, development of a more efficient algorithm could be carried out.

The multiple transformation/multiple interaction concept has much to offer. With its use, arbitrary transmitting structures, including embedded antennas, could be accurately

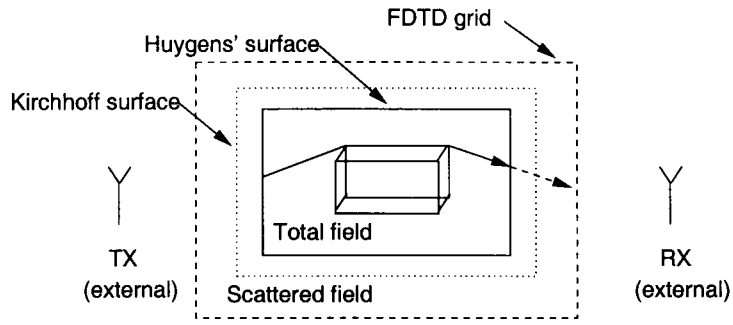

Figure 5.3: Proposed extension of the total field/scattered field formulation to include a spatial transformation.

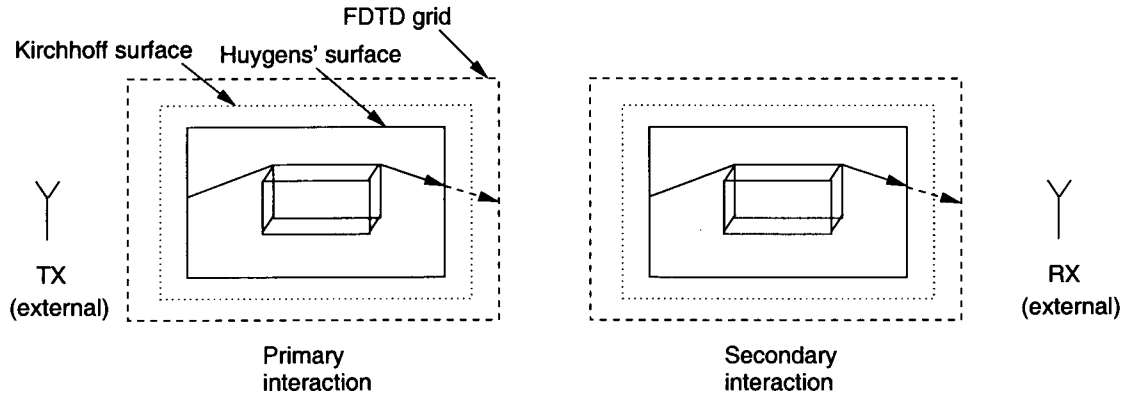

Figure 5.4: Proposed extension of the total field/scattered field formulation to include multiple spatial transformations.

incorporated into propagation modeling problems. Characterization of an entire indoor propagation environment could be carried out with a degree of accuracy not yet attainable using current modeling techniques.

5.2.3.2 Improvements to the Proposed Diffraction Model

The basis of the heuristic modification of the Luebbers formulation presented in this thesis is the determination of the angle at which the Fresnel coefficients R^0 and R^n are calculated. Because R^n multiplies the diffraction coefficient that relates to the reflection field shadow boundary, the angle θ_2 at which R^n is calculated in the modification depends on the angular distance from the reflection field shadow boundary to the observation point.

The original Luebbers formulation used a value for θ_2 measured the from the n face of the wedge to the observation point, regardless of the angle of incidence. With the restrictions that Luebbers placed on the use of the coefficients, this value for θ_2 gave results of sufficient accuracy. The heuristically developed modification has an apparent physical basis, and the connection of the diffraction coefficients to the physics from which they were derived would be an interesting topic of further research.

BIBLIOGRAPHY

1. T. S. Rappaport, *Wireless Communications: Principles and Practice.* New Jersey: Prentice-Hall, 1996.

2. S. Y. Wang and S. H. Lin, "High speed III-V electrooptic waveguide modulators at $\lambda = 1.3\mu$m," *J. Lightwave Technol.*, vol. 6, pp. 758–771, June 1988.

3. D. Jäger, R. Kremer, and A. Stöhr, "Travelling-wave optoelectronic devices for microwave applications," in *1995 IEEE MTT-S International Microwave Symposium Digest*, pp. 163–166, Orlando, FL, USA, 1995.

4. M. Piket-May, A. Taflove, and J. Baron, "FD-TD modeling of digital signal propagation in 3-D circuits with passive and active loads," *IEEE Trans. Microwave Theory Tech.*, vol. 42, pp. 1514–1523, Aug. 1994.

5. W. Sui, D. A. Christensen, and C. H. Durney, "Extending the two-dimensional FD-TD method to hybrid electromagnetic systems with active and passive lumped elements," *IEEE Trans. Microwave Theory Tech.*, vol. 40, pp. 724–730, Apr. 1992.

6. D. Paul, N. M. Pothecary, and C. J. Railton, "Calculation of dispersive characteristics of open dielectric structures by the finite-difference time-domain method," *IEEE Trans. Microwave Theory Tech.*, vol. 42, pp. 1207–1212, July 1994.

7. G. Franceschetti and C. H. Papas, "Pulsed antennas," *IEEE Trans. Antenn. Propagat.*, vol. AP-22, pp. 651–661, Sept. 1974.

8. R. Cicchetti, "Transient analysis of radiated field from electric dipoles and microstrip lines," *IEEE Trans. Antenn. Propagat.*, vol. 39, pp. 910–918, July 1991.

9. T. P. Montoya and G. S. Smith, "A study of pulse radiation from several broad-band loaded monopoles," *IEEE Trans. Antenn. Propagat.*, vol. 44, pp. 1172–1182, Aug. 1996.

10. E. M. Kennaugh and D. L. Moffatt, "Transient and impulse response approximations," *Proc. IEEE*, vol. 53, pp. 893–901, Aug. 1965.

11. E. Sano and T. Shibata, "Fullwave analysis of picosecond photoconductive switches," *IEEE J. Quantum Electron.*, vol. 26, pp. 372–377, Feb. 1990.

12. S. M. El-Ghazaly, F. P. Joshi, and R. O. Grondin, "Electromagnetic and transport considerations in subpicosecond photoconductive switch modeling," *IEEE Trans. Microwave Theory Tech.*, vol. 38, pp. 629–637, May 1990.

13. N. M. Froberg, B. B. Hu, X. C. Zhang, and D. H. Auston, "Terahertz radiation from a photoconducting antenna array," *IEEE J. Quantum Electron.*, vol. 28, pp. 2291–2301, Oct. 1992.

14. A. J. Taylor, P. K. Benicewicz, and S. M. Young, "Modeling of femtosecond electromagnetic pulses from large-aperture photoconductors," *Opt. Lett.*, vol. 18, pp. 1340–1342, August 15 1993.

15. H. Hashemi, "The indoor radio propagation channel," *Proc. IEEE*, vol. 81, pp. 943–968, July 1993.

16. A. A. M. Saleh and R. A. Valenzuela, "A statistical model for indoor multipath propagation," *IEEE J. Select. Areas Commun.*, vol. SAC-5, pp. 128–137, Feb. 1987.

17. J. R. Barry, J. M. Kahn, W. J. Krause, E. A. Lee, and D. G. Messerschmitt, "Simulation of multipath impulse response for indoor wireless optical channels," *IEEE J. Select. Areas Commun.*, vol. 11, pp. 367–379, Apr. 1993.

18. T. S. Rappaport, *Wireless Communications: Principles and Practice*, pp. 139–152. New Jersey: Prentice-Hall, 1996.

19. M. C. Jeruchim, P. Balaban, and K. S. Shammugan, *Simulation of Communication Systems.* New York: Plenum, 1992.

20. T. S. Rappaport, "Characterization of UHF multipath radio channels in factory buildings," *IEEE Trans. Antenn. Propagat.*, vol. 37, pp. 1058–1069, Aug. 1989.

21. J. De Moerloose and D. De Zutter, "Surface integral representation radiation boundary condition for the FDTD method," *IEEE Trans. Antenn. Propagat.*, vol. 41, pp. 890–896, July 1993.

22. M. G. M. Hussain, "Antenna patterns of nonsinusoidal waves with the time variation of a Gaussian pulse – Part 1," *IEEE Trans. Electromagn. Compat.*, vol. 30, pp. 504–512, Nov. 1987.

23. J. H. Richmond, "Digital computer solutions of the rigorous equations for scattering problems," *Proc. IEEE*, vol. 53, pp. 796–804, Aug. 1965.

24. E. F. Knott, J. F. Shaeffer, and M. T. Tuley, *Radar Cross Section*, pp. 90–112. Dedham, MA: Artech House, 1985.

25. A. R. Bretones, R. Mittra, and R. G. Martin, "A hybrid technique combining the method of moments in the time domain and FDTD," *IEEE Microwave Guided Wave Lett.*, vol. 8, pp. 281–283, Aug. 1998.

26. G. Cerri, P. Russo, A. Schiavoni, G. Tribellini, and P. Bielli, "MoM-FDTD hybrid technique for analysing scattering problems," *Electron. Lett.*, vol. 34, pp. 438–440, Mar. 1998.

27. K. S. Yee, "Numerical solution of initial boundary value problems involving Maxwell's equations in isotropic media," *IEEE Trans. Antenn. Propagat.*, vol. AP-14, pp. 302–307, Dec. 1966.

28. A. Taflove, *Computational Electrodynamics: The Finite-Difference Time-Domain Method.* Boston: Artech House, 1995.

29. K. S. Kunz and R. J. Luebbers, *The Finite Difference Time Domain Method for Electromagnetics*, pp. 105–122. Boca Raton: CRC Press, 1993.

30. G. R. Kirchhoff, "Zur Theorie der Lichstrahlen," *Annalen der Physik und Chemie*, vol. 18, no. 8, pp. 663–695, 1883.

31. B. B. Baker and E. T. Copson, *The Mathematical Theory of Huygen's Principle.* Oxford: Oxford, 1939.

32. A. E. H. Love, "The integration of the equations of propagation of electric waves," *Philosophical Transactions*, vol. A197, pp. 1–45, 1901.

33. S. A. Schelkunoff, "Kirchhoff's formula, its vector analogue, and other field equivalence theorems," in *The Theory of Electromagnetic Waves, A Symposium*, pp. 107–123, Interscience Publishers, 1951.

34. J. D. Jackson, *Classical Electrodynamics.* New York: Wiley, 1962.

35. O. Ramahi, "Near- and far-field calculation in FDTD simulations using Kirchhoff surface integral representation," *IEEE Trans. Antenn. Propagat.*, vol. 45, pp. 753–759, May 1997.

36. J. M. Johnson and Y. Rahmat–Samii, "MR-FDTD: a multiple-region finite-difference-time domain method," *Microwave and Optical Technol. Lett.*, vol. 14, pp. 101–105, Feb. 1997.

37. J. M. Johnson and Y. Rahmat-Samii, "Multiple region FDTD (MR/FDTD) and its application to microwave analysis and modeling," in *1996 IEEE MTT-S International Microwave Symposium Digest*, pp. 1475–1478, San Franciso, CA, USA, 1996.

38. K. L. Shlager and G. S. Smith, "Comparison of two FDTD near-field to near-field transformations applied to pulsed antenna problems," *Electronics Letters*, vol. 31, pp. 936–938, Aug. 1995.

39. C. L. Britt, "Solution of electromagnetic scattering problems using time domain techniques," *IEEE Trans. Antenn. Propagat.*, vol. 37, pp. 1181–1192, Sept. 1989.

40. J. A. Stratton and L. J. Chu, "Diffraction theory of electromagnetic waves," *Phys. Rev.*, vol. 56, pp. 99–107, 1939.

41. S. A. Schelkunoff, "Some equivalence theorems of electromagnetics and their application to radiation problems," *Bell System Tech. J.*, vol. 15, pp. 92–112, 1936.

42. A. Taflove, *Computational Electrodynamics: The Finite-Difference Time-Domain Method*, pp. 203–224. Boston: Artech House, 1995.

43. V. W. Franz, "Zur Formulierung des Huygensschen Prinzips," *Z. Naturforsch. A*, vol. 3a, pp. 500–506, 1948.

44. K. Umashankar and A. Taflove, "A novel method to analyze electromagnetic scattering of complex objects," *IEEE Trans. Electromagn. Compat.*, vol. EMC-24, pp. 397–405, Nov. 1982.

45. R. J. Luebbers, K. S. Kunz, M. Schneider, and F. Hunsberger, "A finite-difference time-domain near zone to far zone transformation," *IEEE Trans. Antenn. Propagat.*, vol. 39, pp. 429–433, Apr. 1991.

46. K. S. Yee, D. Ingham, and K. L. Shlager, "Time-domain extrapolation to the far field based on FDTD calculations," *IEEE Trans. Antenn. Propagat.*, vol. 39, pp. 410–413, Mar. 1991.

47. A. Reineix and B. Jecko, "Analysis of microstrip patch antennas using finite difference time domain method," *IEEE Trans. Antenn. Propagat.*, vol. 37, pp. 1361–1369, Nov. 1989.

48. I. J. Craddock and C. J. Railton, "Application of the FDTD method and a full time-domain near-field transform to the problem of radiation from a PCB," *Electron. Lett.*, vol. 29, pp. 2017–2018, Nov. 1993.

49. K. L. Shlager and G. S. Smith, "Near-field to near-field transformation for use with FDTD method and its application to pulsed antenna problems," *Electron. Lett.*, vol. 30, pp. 1262–1264, Aug. 1994.

50. M. J. Barth, R. R. McLeod, and R. W. Ziolkowski, "A near- and far-field projection algorithm for finite-difference time-domain codes," *J. Electromagnetic Waves and Applications*, vol. 6, no. 1, pp. 5–18, 1992.

51. J. G. Maloney, G. S. Smith, and W. R. Scott, Jr., "Accurate computation of the radiation from simple antennas using the finite-difference time-domain method," *IEEE Trans. Antenn. Propagat.*, vol. 38, pp. 1059–1068, July 1990.

52. M. Khalladi, J. A. Morente, J. A. Portí, and G. Giménez, "Two near- to far-zone approaches for scattering problems using the TLM method," *IEEE Trans. Antenn. Propagat.*, vol. 41, pp. 502–505, Apr. 1993.

53. K. S. Kunz and R. J. Luebbers, *The Finite Difference Time Domain Method for Electromagnetics*, pp. 105–122. Boca Raton: CRC Press, 1993.

54. C. A. Balanis, *Advanced Engineering Electromagnetics*, pp. 329–334. New York, NY: Wiley, 1989.

55. O. M. Bucci, G. D'Elia, and M. D. Migliore, "Near-field far-field transformation in time domain from optimal plane-polar samples," *IEEE Trans. Antenn. Propagat.*, vol. 46, pp. 1084–1088, July 1998.

56. W. L. Stutzman and G. A. Thiele, *Antenna Theory and Design*, pp. 545–620. New York: Wiley and Sons, 2nd ed., 1998.

57. H. R. Anderson, "A ray-tracing propagation model for digital broadcast systems in urban areas," *IEEE Trans. Broadcasting*, vol. 39, pp. 309–317, Sept. 1993.

58. K. R. Schaubach, N. J. Davis IV, and T. S. Rappaport, "A ray tracing method for predicting path loss and delay spread in microcellular environments," in *Proceedings of the IEEE Vehicular Technology Conference*, pp. 932–935, May 1992.

59. M. Born and E. Wolf, *Principles of Optics*, pp. 109–132. Oxford: Pergamon Press, 2nd ed., 1964.

60. J. B. Keller, "Geometrical theory of diffraction," *J. Opt. Soc. Amer. A*, vol. 52, pp. 116–130, Feb. 1962.

61. R. G. Kouyoumjian and P. H. Pathak, "A uniform geometrical theory of diffraction for an edge in a perfectly conducting surface," *Proc. IEEE*, vol. 62, pp. 1448–1461, Nov. 1974.

62. D. A. McNamara, C. W. I. Pistorius, and J. A. G. Malherbe, *Introduction to the Uniform Geometrical Theory of Diffraction.* Boston: Artech House, 1990.

63. A. Taflove and M. E. Brodwin, "Numerical solution of steady-state electromagnetic scattering problems using the time-dependent Maxwell's equations," *IEEE Trans. Microwave Theory Tech.*, vol. MTT-23, pp. 623–630, Aug. 1975.

64. M. De Pourcq and C. Eng, "Field and power-density calculations in closed microwave systems by three-dimensional finite differences," *IEE Proc. H*, vol. 132, pp. 360–368, Oct. 1985.

65. X. Zhang, J. Fang, K. K. Mei, and Y. Lu, "Calculations of the dispersive characteristics of microstrips by the time-domain finite difference method," *IEEE Trans. Microwave Theory Tech.*, vol. 36, pp. 263–267, Feb. 1988.

66. K. A. Remley, A. Weisshaar, S. M. Goodnick, and V. K. Tripathi, "Modeling of radiation fields in a sub-picosecond photo-conducting system," *VLSI Design*, vol. 8, no. 1-4, pp. 407–412, 1998.

67. J. B. Judkins and R. W. Ziolkowski, "Finite-difference time-domain modeling of nonperfectly conducting metallic thin-film gratings," *J. Opt. Soc. Amer. A*, vol. 12, pp. 1974–1983, Sept. 1995.

68. K. S. Kunz and K. M. Lee, "A three-dimensional finite-difference solution of the external response of an aircraft to a complex transient EM environment," *IEEE Trans. Electromagn. Compat.*, vol. EMC-20, pp. 328–341, Nov. 1978.

69. A. Taflove and K. Umashankar, "Radar cross section of general three-dimensional scatterers," *IEEE Trans. Electromagn. Compat.*, vol. EMC-25, pp. 433–440, Nov. 1983.

70. R. Holland, "Two-pass finite-difference time-domain (FDTD) calculations on a fighter aircraft," *IEEE Trans. Antenn. Propagat.*, vol. 44, pp. 659–664, May 1996.

71. W. L. Stutzman and G. A. Thiele, *Antenna Theory and Design*, pp. 524–531. New York: Wiley and Sons, 2nd ed., 1998.

72. M. R. Zunoubi, N. H. Younan, J. H. Beggs, and C. D. Taylor, "FDTD analysis of linear antennas driven from a discrete impulse excitation," *IEEE Trans. Electromagn. Compat.*, vol. 39, pp. 247–250, Aug. 1997.

73. K. L. Shlager and J. B. Schneider, "A selective survey of the finite-difference time-domain literature," *IEEE Ant. and Prop. Mag.*, vol. 37, pp. 39–56, Aug. 1995.

74. W. L. Stutzman and G. A. Thiele, *Antenna Theory and Design*, pp. 493–544. New York: Wiley and Sons, 2nd ed., 1998.

75. G. Mur, "Absorbing boundary conditions for the finite-difference approximation of the time-domain electromagnetic-field equations," *IEEE Trans. Electromagn. Compat.*, vol. 23, pp. 1073–1077, 1981.

76. T. G. Moore, F. G. Blaschak, A. Taflove, and G. A. Kriegsmann, "Theory and application of radiation boundary operators," *IEEE Trans. Antenn. Propagat.*, vol. 36, pp. 1797–1812, Dec. 1988.

77. J. P. Berenger, "A perfectly matched layer for the absorption of electromagnetic waves," *J. Computational Physics*, vol. 114, pp. 185–200, 1994.

78. C. A. Balanis, *Advanced Engineering Electromagnetics*, ch. 6. New York: Wiley, 1st ed., 1989.

79. A. Taflove and K. R. Umashankar, "Solution of complex electromagnetic penetration and scattering problems in unbounded regions," in *Computational Methods for Infinite Domain Media-Structure Interaction*, vol. 46, pp. 83–113, New York: ASME, 1981.

80. A. Taflove, *Computational Electrodynamics: The Finite-Difference Time-Domain Method*, pp. 40–46 and 93–106. Boston: Artech House, 1995.

81. The MathWorks, *MATLAB v5.1*, Apr. 1997.

82. M. C. Falconer, *Three dimensional electromagnetic FDTD simulation of general lossy structures with nonuniform grid spacing.* PhD thesis, Oregon State University, Department of Electrical and Computer Engineering, Jan. 1997.

83. H. F. Harmuth, *Antennas and Waveguides for Nonsinusoidal Waves*, vol. supp. 15 of *Advances in Electronics and Electron Physics*, pp. 44–54. Orlando: Academic Press, 1984.

84. D. Buechler, D. Roper, C. Durney, and D. Christensen, "Modeling sources in the FDTD formulation and their use in quantifying source and boundary condition errors," *IEEE Trans. Microwave Theory Tech.*, vol. 43, pp. 810–814, Apr. 1995.

85. S. M. Sohel Imtiaz, M. A. Llsunaidi, and S. M. El-Ghazaly, "Performance comparison of MODFET and MESFET using combined electromagnetic and solid-state simulator," in *1996 IEEE MTT-S International Microwave Symposium Digest*, (San Francisco, CA, USA), pp. 1783–1786, 1996.

86. J. A. Valdmanis and G. Mourou, "Subpicosecond electrooptic sampling: principles and applications," *IEEE J. Quantum Electron.*, vol. QE-22, pp. 69–78, Jan. 1986.

87. B. I. Greene, J. F. Federici, D. R. Dykaar, A. F. Levi, and L. Pfeiffer, "Picosecond pump and probe spectroscopy utilizing freely propagating terahertz radiation," *Opt. Lett.*, vol. 16, pp. 48–49, Jan. 1991.

88. K. A. Remley, A. Weisshaar, S. M. Goodnick, and V. K. Tripathi, "Characterization of near- and far-field radiation from ultrafast electronic systems," *IEEE Trans. Microwave Theory Tech.*, vol. 45, no. 12, pp. 407–412, 1998.

89. K. A. Remley, A. Weisshaar, S. M. Goodnick, and V. K. Tripathi, "Near and far field characterization of radiation from ultra-fast electronic systems," in *1998 IEEE MTT-S International Microwave Symposium Digest*, (Baltimore, MD, USA), pp. 1073–1076, June 1998.

90. M. van Exter and D. R. Grischkowsky, "Characterization of an optoelectronic terahertz beam system," *IEEE Trans. Microwave Theory Tech.*, vol. 38, pp. 1684–1691, Nov. 1990.

91. J. Son, W. Sha, T. B. Norris, J. F. Whitaker, and G. A. Mourou, "Transient velocity overshoot dynamics in GaAs for electric fields <200kV/cm," *Appl. Phys. Lett.*, vol. 63, pp. 923–925, Aug. 1993.

92. U. D. Keil and D. R. Dykaar, "Electro-optic sampling and carrier dynamics at zero propagation distance," *Appl. Phys. Lett.*, vol. 61, pp. 1504–1506, Sept. 1992.

93. Y. Lu, "New method of analysing transient processes in picosecond photoconductive switch," *Electron. Lett.*, vol. 26, pp. 444–445, Mar. 1990.

94. U. D. Keil, D. R. Dykaar, R. F. Kopf, and S. B. Darack, "Femtosecond reflectivity measurements and second harmonic generation in nonresonant excitation of photoconductive switches," *Appl. Phys. Lett.*, vol. 64, pp. 1812–1814, Apr. 1994.

95. P. R. Smith, D. H. Auston, and M. C. Nuss, "Subpicosecond photoconducting dipole antennas," *IEEE J. Quantum Electron.*, vol. 24, pp. 255–260, Feb. 1988.

96. C. R. Lutz and A. P. DeFonzo, "Far-field characteristics of optically pulsed millimeter wave antennas," *Appl. Phys. Lett.*, vol. 54, pp. 2186–2188, May 1984.

97. B. B. Hu, J. T. Darrow, X. Zhang, and D. H. Auston, "Optically steerable photoconducting antennas," *Appl. Phys. Lett.*, vol. 56, pp. 886–888, Mar. 1990.

98. B. I. Greene, P. N. Saeta, D. R. Dykaar, S. Schmitt-Rink, and S. L. Chuang, "Far-infrared light generation at semiconductor surfaces and its spectroscopic applications," *IEEE J. Quantum Electron.*, vol. 28, pp. 2302–2312, Oct. 1992.

99. L. Duvillaret, F. Garet, and J. Coutaz, "A reliable method for extraction of material parameters in terahertz time-domain spectroscopy," *IEEE J. Select. Topics Quantum Electron.*, vol. 2, pp. 739–746, Sept. 1996.

100. E. Özbay, E. Michel, G. Tuttle, R. Biswas, and K. M. Ho, "Terahertz spectroscopy of three-dimensional photonic band-gap crystals," *Opt. Lett.*, vol. 19, pp. 1155–1157, Aug. 1994.

101. S. M. Goodnick, S. Pennathur, U. Ranawake, P. M. Lenders, and V. K. Tripathi, "Parallel implementation of a Monte Carlo particle simulation coupled to Maxwell's equations," *Intl. J. of Num. Modelling*, vol. 8, pp. 205–219, 1995.

102. C. A. Balanis, *Advanced Engineering Electromagnetics*, pp. 285–305. New York: Wiley, 1989.

103. D. K. Cheng, *Field and Wave Electromagnetics*, pp. 602–607. Reading, MA: Addison-Wesley, 2nd ed., 1990.

104. T. S. Rappaport and S. Sandhu, "Radio-wave propagation for emerging wireless personal-communications systems," *IEEE Ant. and Prop. Mag.*, vol. 36, pp. 14–23, Oct. 1994.

105. M. Döttling, T. C. Becker, and W. Wiesbeck, "Modeling of the DECT outdoor radio channel," in *Proceedings of the 47th IEEE Vehicular Technology Conference*, pp. 1947–1951, May 1997.

106. R. P. Torres, L. Valle, and M. Domingo, "Computer tool to analyze radio channel in arbitrary enclosed spaces using ray tracing," in *Proceedings of the 48th IEEE Vehicular Technology Conference*, pp. 581–585, Ottawa, Canada, May 1998.

107. G. Wölfle and F. M. Landstorfer, "Field strength predictions in indoor environments with neural networks," in *Proceedings of the 47th IEEE Vehicular Technology Conference*, pp. 82–86, May 1997.

108. G. Wölfle and F. M. Landstorfer, "Dominant paths for the field strength prediction," in *Proceedings of the 48th IEEE Vehicular Technology Conference*, pp. 552–556, May 1998.

109. M. Nidd, S. Mann, and J. Black, "Using ray tracing for site-specific indoor radio signal strength analysis," in *Proceedings of the 47th IEEE Vehicular Technology Conference*, pp. 795–799, May 1997.

110. F. Aguado, F. P. Fontan, and A. Formella, "Indoor and outdoor channel simulator based on ray tracing," in *Proceedings of the 47th IEEE Vehicular Technology Conference*, pp. 2065–2069, IEEE, May 1997.

111. B. De Backer, H. Börjeson, F. Olysager, and D. De Zutter, "The study of wave-propagation through a windowed wall at 1.8 GHz," in *Proceedings of the 46th IEEE Vehicular Technology Conference*, pp. 165–169, 1996.

112. A. Lauer, A. Bahr, and I. Wolff, "FDTD simulations of indoor propagation," in *Proceedings of the 44th IEEE Vehicular Technology Conference*, pp. 883–886, 1994.

113. A. Lauer, I. Wolff, A. Bahr, J. Pamp, and J. Kunisch, "Multi-mode FDTD simulations of indoor propagation including antenna properties," in *Proceedings of the 45th IEEE Vehicular Technology Conference*, pp. 454–458, 1995.

114. J. Litva, C. Wu, and A. Ghaforian, "Use of FDTD for simulating the angle of arrival and time delay of signals propagating in indoor environments," *Electron. Lett.*, vol. 32, pp. 930–932, May 9 1996.

115. G. Stratis, V. Anantha, and A. Taflove, "Numerical calculation of diffraction coefficients of generic conducting and dielectric wedges using FDTD," *IEEE Trans. Antenn. Propagat.*, vol. 45, pp. 1525–1529, Oct. 1997.

116. H. R. Anderson, *Development and Applications of Site-Specific Microcell Communications Channel Modelling Using Ray-Tracing.* PhD thesis, University of Bristol, Department of Electrical Engineering, Oct. 1994.

117. H. R. Anderson, EDX Engineering, "Microcell 3D Ray-Tracing Module," *Microcell Communication Simulator Software*, 1997.

118. W. L. Stutzman and G. A. Thiele, *Antenna Theory and Design*, pp. 76–81. New York: Wiley and Sons, 2nd ed., 1998.

119. T. S. Rappaport, *Wireless Communications: Principles and Practice*, pp. 70–77. New Jersey: Prentice-Hall, 1996.

120. P. D. Holm, "Diffraction coefficients for higher order wedge diffracted fields," *IEEE Trans. Antenn. Propagat.*, vol. 44, pp. 879–888, June 1996.

121. R. J. Luebbers, "Finite conductivity uniform UTD versus knife diffraction prediction of propagation path loss," *IEEE Trans. Antenn. Propagat.*, vol. AP-32, pp. 70–76, Jan. 1984.

122. T. S. Rappaport, *Wireless Communications: Principles and Practice*, pp. 153–159. New Jersey: Prentice-Hall, 1996.

123. M. J. Neve, G. B. Rowe, K. W. Sowerby, and A. G. Williamson, "On the investigation of radiowave propagation mechanisms for future wireless communications services planning," in *Proceedings of the 46th IEEE Vehicular Technology Conference*, vol. 2, pp. 615–619, May 1996.

124. D. M. J. Devasirvatham, "Time delay spread and signal level measurements of 850 MHz radio waves in building environments," *IEEE Trans. Antenn. Propagat.*, vol. AP-34, pp. 1300–1305, Nov. 1986.

125. M. I. Herman and J. L. Volakis, "High frequency scattering by a double impedance wedge," *IEEE Trans. Antenn. Propagat.*, vol. 36, pp. 664–678, May 1988.

126. J. R. Mautz and R. F. Harrington, "Radiation and scattering from large polygonal cylinders, transverse electric fields," *IEEE Trans. Antenn. Propagat.*, vol. AP-24, pp. 469–477, July 1976.

127. W. L. Stutzman and G. A. Thiele, *Antenna Theory and Design, 2nd ed.*, pp. 427–492. New York: Wiley and Sons, 2nd ed., 1998.

128. J. R. Mentzer, "Scattering and diffraction of radio waves," in *Electronics and Waves–a series of monographs* (D. W. Fry, ed.), vol. 7, pp. 6–55, London: Pergamon Press, 1955.

129. J. W. Crispin and K. M. Siegal, eds., *Methods of Radar Cross-Section Analysis.* New York: Academic Press, 1968.

130. J. W. Crispin and A. L. Maffett, "Radar cross-section estimation for complex shapes," *Proc. IEEE*, vol. 53, pp. 972–982, Aug. 1965.

131. A. J. Giger, *Low-Angle Microwave Propagation: Physics and Modeling*, pp. 99–124. Artech House, 1991.

132. G. D. Maliuzhinets, "Excitation, reflection, and emission of surface waves from a wedge with given face impedances," *Sov. Akad. Phys.*, vol. 3, pp. 752–755, 1958.

133. D. E. Eliades, "High-frequency scattering from the edges of impedance discontinuities on a flat plane," *IEEE Trans. Antenn. Propagat.*, vol. AP-31, pp. 16–33, July 1983.

134. A. V. Osipov, "General solution of a class of diffraction problems," *J. Phys. A: Math. Gen.*, vol. 27, pp. 27–32, 1994.

135. C. Demetrescu, C. C. Constantinou, and M. J. Mehler, "Scattering by a right-angled lossy dielectric wedge," *IEE Proc.-Microw. Antennas Propag.*, vol. 144, pp. 392–396, Oct. 1997.

136. C. Demetrescu, C. C. Constantinou, and M. J. Mehler, "Corner and rooftop diffraction in radiowave propagation prediction tools: A review," in *Proceedings of the 48th IEEE Vehicular Technology Conference*, pp. 515–519, May 1998.

137. R. J. Luebbers, "Comparison of lossy wedge diffraction coefficients with application to mixed path propagation loss prediction," *IEEE Trans. Antenn. Propagat.*, vol. 36, pp. 1031–1034, July 1988.

138. R. J. Luebbers, "Propagation prediction for hilly terrain using GTD wedge diffraction," *IEEE Trans. Antenn. Propagat.*, vol. AP-32, pp. 951–955, Sept. 1984.

139. R. J. Luebbers, "A heuristic UTD slope diffraction coefficient for rough lossy wedges," *IEEE Trans. Antenn. Propagat.*, vol. 37, pp. 206–211, Feb. 1989.

140. W. D. Bursnide and K. W. Burgener, "High frequency scattering by a thin lossless dielectric wedge," *IEEE Trans. Antenn. Propagat.*, vol. AP-31, pp. 104–110, Jan. 1983.

141. G. A. J. van Dooren and M. H. A. J. Herben, "Field strength prediction behind lossy dielectric obstacles by using the UTD," *Electron. Lett.*, vol. 29, pp. 1016–1018, May 1993.

142. K. Rizk, J. Wagen, and F. Gardiol, "Two-dimensional ray-tracing modeling for propagation prediction in microcellular environments," *IEEE Trans. Vehic. Technol.*, vol. 46, pp. 508–517, May 1997.

143. D. E. Merewether, R. Fisher, and F. W. Smith, "On implementing a numeric Huygen's source scheme in a finite difference program to illuminate scattering bodies," *IEEE Trans. Nucl. Sci.*, vol. NS-27, pp. 1829–1833, Dec. 1980.

144. P. Bhattacharya, *Semiconductor Optoelectronic Devices*, pp. 119–139. Englewood Cliffs, NJ: Prentice-Hall, 1st ed., 1994.

APPENDICES

A. FDTD GRID DISPERSION: TWO-DIMENSIONAL CASE

Find the velocity of a wave as it travels through a 2-D FDTD grid as a fraction of the velocity in free space, c. Specify the angle of propagation, α, off the x axis of the grid ($\alpha = 0$ corresponds to the x axis of the grid, $\alpha = \pi/2$ corresponds to the y axis of the grid).

Start with the 2-D grid dispersion relationship (see [80]):

$$\left[\frac{1}{c\,\Delta t}\sin\left(\frac{\omega\Delta t}{2}\right)\right]^2 = \left[\frac{1}{\Delta x}\sin\left(\frac{k_x\Delta x}{2}\right)\right]^2 + \left[\frac{1}{\Delta y}\sin\left(\frac{k_y\Delta y}{2}\right)\right]^2. \tag{A.1}$$

For $\Delta = \Delta x = \Delta y = \Delta z$, (A.1) may be written

$$\left(\frac{\Delta}{c\,\Delta t}\right)^2 \sin^2\left(\frac{\omega\Delta t}{2}\right) = \sin^2\left(\frac{k_x\Delta}{2}\right) + \sin^2\left(\frac{k_y\Delta}{2}\right). \tag{A.2}$$

Letting $k_x = k\cos\alpha$, and $k_y = k\sin\alpha$,

$$\left(\frac{\Delta}{c\,\Delta t}\right)^2 \sin^2\left(\frac{\omega\Delta t}{2}\right) = \sin^2\left(\frac{\Delta k\cos\alpha}{2}\right) + \sin^2\left(\frac{\Delta k\sin\alpha}{2}\right). \tag{A.3}$$

Use the Newton-Rapheson method to find the values of k that satisfy (A.3):

$$k_{i+1} = k_i - \frac{f(k_i)}{f'(k_i)}. \tag{A.4}$$

Here

$$f(k_i) = \sin^2\left(\frac{\Delta k_i\cos\alpha}{2}\right) + \sin^2\left(\frac{\Delta k_i\sin\alpha}{2}\right) - \left(\frac{\Delta}{c\,\Delta t}\right)^2 \sin^2\left(\frac{\omega\Delta t}{2}\right), \tag{A.5}$$

and, using the trigonometric identity $\sin^2 x = \frac{1}{2} - \frac{\cos 2x}{2}$,

$$f'(k) = 1 - \frac{\Delta\cos\alpha}{2}\cos\left(\Delta k_i\cos\alpha\right) - \frac{\Delta\sin\alpha}{2}\cos\left(\Delta k_i\sin\alpha\right). \tag{A.6}$$

Letting $A = \frac{\Delta\cos\alpha}{2}$, $B = \frac{\Delta\sin\alpha}{2}$, and $C = \left(\frac{\Delta}{c\,\Delta t}\right)^2\sin^2\left(\frac{\omega\Delta t}{2}\right)$,

$$k_{i+1} = k_i - \frac{\sin^2\left(Ak_i\right) + \sin^2\left(Bk_i\right) - C}{1 - A\cos\left(2Ak_i\right) - B\cos\left(2Bk_i\right)} \tag{A.7}$$

Equation (A.7) is iteratively solved for a desired accuracy. The initial choice for k_i is the free space wave number, $k_0 = \frac{2\pi}{\lambda}$. The final result, v_p, is given as:

$$v_p = k_0/k_{i+1} \tag{A.8}$$

B. DERIVATION OF THE KIRCHHOFF SURFACE INTEGRAL

Given functions ψ and β that satisfy the wave equation:

$$\frac{\partial^2 \Phi}{\partial t^2} = c^2 \nabla^2 \Phi \qquad \Phi = \psi,\ \beta \tag{B.1}$$

where ∇ represents partial differentiation with respect to x, y, and z, and c is the speed of light in a vacuum. A function of this type would be, for example,

$$\Phi = \frac{1}{R} \cos 2\pi \left(\frac{R}{\lambda} - \frac{t}{T} \right) = \frac{1}{R} \cos \left(k_0 R - \omega t \right). \tag{B.2}$$

where k_0 is the free space wavenumber, and ω is the frequency in radians.

Write Green's theorem as:

$$\int_{s'} \left(\psi \frac{\partial \beta}{\partial n} - \beta \frac{\partial \psi}{\partial n} \right) ds = \int_{V'} \left(\beta \nabla^2 \psi - \psi \nabla^2 \beta \right) dV. \tag{B.3}$$

Substitute from (B.1)

$$\int_{s'} \left(\psi \frac{\partial \beta}{\partial n} - \beta \frac{\partial \psi}{\partial n} \right) ds = \frac{1}{c^2} \int_{V'} \left(\beta \frac{\partial^2 \psi}{\partial t^2} - \psi \frac{\partial^2 \beta}{\partial t^2} \right) dV. \tag{B.4}$$

Or, since integration and differentiation are linear operators,

$$\int_{s'} \left(\psi \frac{\partial \beta}{\partial n} - \beta \frac{\partial \psi}{\partial n} \right) ds = \frac{1}{c^2} \frac{\partial}{\partial t} \int_{V'} \left(\beta \frac{\partial \psi}{\partial t} - \psi \frac{\partial \beta}{\partial t} \right) dV. \tag{B.5}$$

Integrate both sides with respect to time:

$$\int_{-t'}^{t''} dt \int_{s'} \left(\psi \frac{\partial \beta}{\partial n} - \beta \frac{\partial \psi}{\partial n} \right) ds = \frac{1}{c^2} \left[\int_{V'} \left(\beta \frac{\partial \psi}{\partial t} - \psi \frac{\partial \beta}{\partial t} \right) dV \right]_{-t'}^{t''}. \tag{B.6}$$

Let

$$\beta = \frac{F\left(r_o + ct\right)}{r_o} \tag{B.7}$$

where the $F\left(r_o + ct\right) = 0$ for all positive and negative arguments, and

$$\int F(\zeta) d\zeta = 1. \tag{B.8}$$

i.e., $F\left(r_o + ct\right)$ is a delta function.

Given a surface, s, in a homogeneous problem space, let r_o be the distance from a small area ds on the surface to any point o. Let o be at the center of a small sphere, S, and perform a time shift such that $(r_o - ct')$ is negative and finite for the largest value of r_o. Then the arguments of β and $\frac{\partial\beta}{\partial t}$ have values for which $(r_o + ct')$ is finite (nonzero) and therefore the righthand side of (B.6) vanishes.

Assuming no singularities (sources) on the side of s where S is located, one can write:

$$\int_{-t'}^{t''} dt \int_{s'} \left(\psi\frac{\partial\beta}{\partial n} - \beta\frac{\partial\psi}{\partial n}\right) ds + \int_{-t'}^{t''} dt \int_{S'} \left(\psi\frac{\partial\beta}{\partial n} - \beta\frac{\partial\psi}{\partial n}\right) dS = 0. \tag{B.9}$$

The second integral (relating to S) can be solved. Let R be the radius of the small sphere. Then $\partial n = \partial R$ and

$$\frac{\partial\beta}{\partial n} = \frac{\partial\frac{F(R+ct)}{R}}{\partial R} = \frac{R\frac{\partial}{\partial R}F(R+ct) - 1F(R+ct)}{R^2}. \tag{B.10}$$

Letting $R \to 0$,

$$\frac{\partial\beta}{\partial n} \to \frac{-F(ct)}{R^2}, \tag{B.11}$$

and $\beta \to 0$ since $R + ct \neq 0$.

Therefore,

$$\int_{S'} \left(\psi\frac{\partial\beta}{\partial n} - \beta\frac{\partial\psi}{\partial n}\right) dS = \int_0^{2\pi}\int_0^{\pi} \psi\frac{\partial\beta}{\partial n}R^2\sin\theta d\theta d\phi = -4\pi\psi F(ct). \tag{B.12}$$

As $R \to 0, \psi \to \psi_o$. ψ_o is the value of ψ at point o and so

$$\int_{S'} \left(\psi\frac{\partial\beta}{\partial n} - \beta\frac{\partial\psi}{\partial n}\right) dS = -4\pi\psi_o F(ct). \tag{B.13}$$

Another property of the delta function is:

$$\int_{-t'}^{t''} F(at)dt = \frac{1}{a}. \tag{B.14}$$

to maintain an area of one. So

$$-4\pi\psi_o F(ct) = \frac{4\pi}{c}\psi_o(0), \tag{B.15}$$

where $\psi_o(0)$ means ψ_o at time $t = 0$. Now (B.9) becomes

$$\int_{-t'}^{t''} dt \int_{s'} \left(\psi \frac{\partial \beta}{\partial n} - \beta \frac{\partial \psi}{\partial n} \right) ds = \frac{4\pi}{c} \psi_o(0). \tag{B.16}$$

ψ_o is the scalar field quantity which will be the final solution of the Kirchhoff surface integral.

Now consider the lefthand term of (B.9). We can write

$$c \int_{-t'}^{t''} \beta \frac{\partial \psi}{\partial n} dt = c \int_{-t'}^{t''} \frac{F(r_o + ct)}{r_o} \frac{\partial \psi}{\partial n} dt = \frac{1}{r_o} \frac{\partial \psi}{\partial n}. \tag{B.17}$$

This is nonzero when $t = -r_o/c$. Or

$$c \int_{-t'}^{t''} \beta \frac{\partial \psi}{\partial n} dt = \frac{1}{r_o} \frac{\partial \psi \left(\frac{-r_o}{c} \right)}{\partial n}. \tag{B.18}$$

This is the *normal* derivative term of the Kirchhoff surface integral.

Now look at the other term on the lefthand side of (B.9). Use the chain rule to find:

$$\begin{aligned} \frac{\partial \beta}{\partial n} = \frac{\partial \frac{F(r_o+ct)}{r_o}}{\partial n} &= \frac{\partial \frac{1}{r_o}}{\partial n} F(r_o + ct) + \frac{1}{r_o} \frac{\partial F(r_o + ct)}{\partial (r_o + ct)} \frac{\partial (r_o + ct)}{\partial n} \\ &= \frac{\partial \frac{1}{r_o}}{\partial n} F\left(\frac{r_o}{c} \right) + \frac{1}{r_o} \frac{\partial r_o}{\partial n} \frac{1}{c} \frac{\partial F(r_o + ct)}{\partial t}. \end{aligned} \tag{B.19}$$

Then,

$$\begin{aligned} c \int_{-t'}^{t''} \psi \frac{\partial \beta}{\partial n} dt &= \frac{\partial \frac{1}{r_o}}{\partial n} \int_{-t'}^{t''} \psi F(r_o + ct) dt + \frac{1}{r_o} \frac{\partial r_o}{\partial n} \int_{-t'}^{t''} \psi \frac{\partial F(r_o + ct)}{\partial t} dt \\ &= \frac{\partial \frac{1}{r_o}}{\partial n} \psi \left(\frac{-r_o}{c} \right) + \frac{1}{r_o} \frac{\partial r_o}{\partial n} \int_{-t'}^{t''} \psi \frac{\partial F(r_o + ct)}{\partial t} dt. \end{aligned} \tag{B.20}$$

where $t = -r_o/c$.

Do integration by parts on the righthand term of (B.20):

$$\int_a^b u dv = uv \Big]_a^b - \int_a^b v du \tag{B.21}$$

Let

$$\begin{aligned} u &= \psi \\ du &= \frac{\partial \psi}{\partial t} dt \\ dv &= \frac{\partial F(r_o + ct)}{\partial t} dt \\ v &= \frac{1}{c} F(r_o + ct) \end{aligned}$$

Substitute into (B.21)

$$\begin{aligned}\int_{-t'}^{t''} \psi \frac{\partial \beta}{\partial n} dt &= \psi \frac{F(r_o + ct)}{c} \Big]_{-t'}^{t''} - \frac{1}{c} \int_{-t'}^{t''} F(r_o + ct) \frac{\partial \psi}{\partial t} dt \\ &= -\frac{1}{c} \frac{\partial \psi(r_o + ct)}{\partial t}\end{aligned} \tag{B.22}$$

The first term on the righthand side of (B.22) vanishes when the integral is evaluated at the limits, since the argument of the delta function is nonzero. The second term on the righthand side is the result of the time shifting property of the delta function.

This leads to the final form of the integral:

$$\psi_o(t) = \frac{1}{4\pi} \int_{s'} \left\{ \frac{\partial \frac{1}{r_o}}{\partial n} \psi \left(t - \frac{r_o}{c} \right) - \frac{1}{c r_o} \frac{\partial r_o}{\partial n} \frac{\partial \psi \left(t - \frac{r_o}{c} \right)}{\partial t} - \frac{1}{r_o} \frac{\partial \psi \left(t - \frac{r_o}{c} \right)}{\partial n} \right\} ds. \tag{B.23}$$

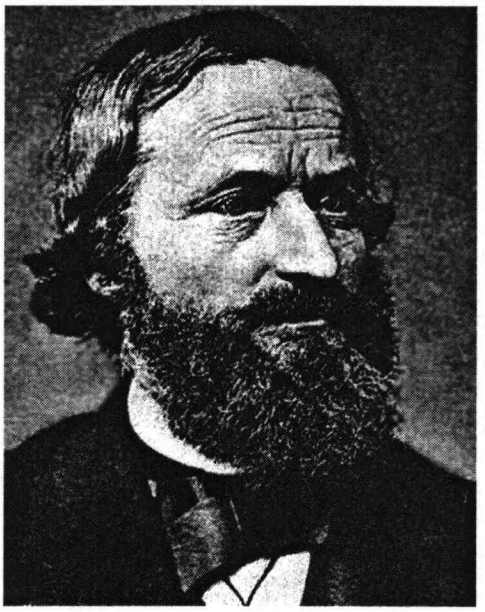

Gustav Robert Kirchhoff

German Physicist

1824-1887

Figure B.1: Portrait of G. R. Kirchhoff.

C. THE ALGORITHM USED IN THE KIRCHHOFF SURFACE INTEGRAL FORMULATION

The algorithm used for implementation of the Kirchhoff surface integral is common to both the analytic and the combined FDTD/Kirchhoff versions of the code. It is presented in three sections below: Initialization of the Spatial Transformation, Calculation of the Surface Field, and Integration. In each section, the main points of action are first stated, followed by a more detailed description of each step.

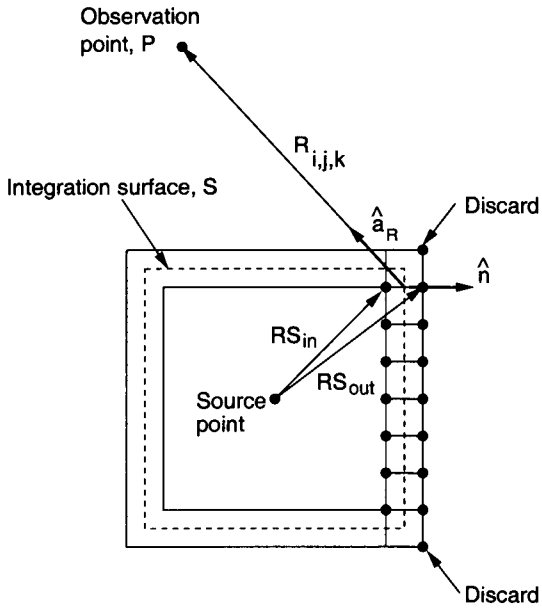

Figure C.1: Calculation of the inner and outer surface field position vectors, RS_{in} and RS_{out}. The position vector from the surface to the observation point is given by $R_{i,j,k}$.

Initialization of the Spatial Transformation

1. **Observation point(s) are specified in Cartesian coordinates.** When multiple points are specified, the integration calculation is performed with respect to each observation point at each timestep.

2. **The dimensions and location of the integration surface are specified.** The surface of integration may be considered to lie between an inner and an outer cube. In the FDTD implementation, the surface for each scalar field component is offset spatially corresponding to the Yee cell (Figure 2.1). For example, for calculation of the integral in the yz plane, the surface used to determine E_z is spatially offset from the surface used to determine E_x by $\Delta y/2$.

3. **$\vec{RS}$, $\vec{R}$, p, and $\hat{n} \cdot \hat{a}_R$ are calculated and stored** (refer to Figure C.1). The distances from the center of the integration surface to each grid point on the inner and outer cubes, RS_{in} and RS_{out}, respectively (as shown in Figure C.1), may be precalculated in the code and stored. The distances $R_{i,j,k}$ from each surface element $\Delta s_{i,j,k}$ to each observation point P_n also may be precalculated and stored.

   As stated previously, the terms $\frac{\partial R}{\partial n}$ and $\frac{\partial}{\partial n}\left(\frac{1}{R}\right)$ in (2.14) are equivalent to $(\hat{n} \cdot \hat{a}_R)$ and $\frac{-(\hat{n} \cdot \hat{a}_R)}{R^2}$, respectively, where $\hat{a}_R$ is the unit vector in the direction of $\vec{R}$. The terms $nu = \hat{n} \cdot \hat{a}_R$ and p (used for the time interpolation described below) may be precalculated and stored for each surface element. The subscripts i, j, k have been omitted for clarity.

Surface Field Calculation

1. **The source excitation is calculated or loaded from a data file.** If the source is modeled analytically as a Hertzian dipole, i. e., a dipole with negligible length, the equations can be found from (2.20). If the FDTD method is used for the implementation of a Hertzian dipole, the technique presented in Ref. [84] is used, i. e., the current distribution is considered constant over the volume of one grid cell. Again, the excitation is given by (2.20).

2. **The surface and normal derivative fields are found.** As described above, the inner and outer surface fields can be generated in two ways: first, by using analytic expressions for the fields from a known current distribution, and second, by using the fields naturally generated by a current source implemented in the FDTD code.

For both implementations, the following routine may be used to find the discretized components of the surface integral:

a. The inner and outer surface fields, ϕ_{in} and ϕ_{out} respectively, are calculated (using RS_{in} and RS_{out}).

b. The surface field (used in the *direct* and *time* terms) is found using the mean of the inner and outer fields, $\frac{\phi_{out}+\phi_{in}}{2}$.

c. The normal derivative field (used in the *normal* term) is found from a difference equation utilizing the inner and outer surface fields, $\frac{\phi_{out}-\phi_{in}}{\Delta}$, where Δ is the distance between the inner and outer cubes.

Integration

1. **The *direct*, *time*, and *normal* terms are calculated and combined in the delayed field vector.** Each term is assigned its proper delay time and is added to the delayed field vector, as shown in Figure 2.7. In this manner, the integration routine may be considered as a time-weighted summation. The time it takes the wave to travel from surface element $\Delta s_{i,j,k}$ to the n_{th} observation point P_n is not generally a multiple of the time increment, therefore interpolation is used. Linear interpolation is sufficient to maintain second order accuracy for the *direct* and *time* terms. The delayed field, $[\phi_{i,j,k}]$, is divided between the two nearest time steps. Since the same fractional division, p, will occur at each time step, this quantity can be precalculated and stored. For example, let the total delay time $\tau_{i,j,k}$ at time step n associated with surface element $\Delta s_{i,j,k}$ be 3.2 ms. Further, let the time increment, Δt, be 1 ms. Then, the fractional part of $\tau_{i,j,k}/\Delta t$ is $p = 0.2$. As given in (2.18), $0.8\times[\phi_{i,j,k}]$ is assigned a delay time of 3 ms and $0.2\times[\phi_{i,j,k}]$ is assigned a delay time of 4 ms. To maintain second order accuracy for the time derivative term, a Lagrange interpolation scheme is utilized during the integration. Again, see (2.18) for details.

   The primary output of the code is the delayed field vector, which contains the time evolution of the fields at the observation point, i. e. $[E_x]$, $[E_y]$, and $[E_z]$.

D. RAY-TRACING DIFFRACTION COEFFICIENTS

Based on the geometry shown in Figure 4.2, the Luebbers diffraction coefficients [121] are given as follows:

$$
\begin{aligned}
D_{\substack{\perp \\ \parallel}}(L,\phi,\phi') &= \frac{-e^{-j\pi/4}}{2n\sqrt{2\pi\beta}\sin\gamma_o'} \\
&\times \left[\cot\left(\frac{\pi+(\phi-\phi')}{2n}\right) F\left[\beta L a^+(\phi-\phi')\right]\right. \\
&+ \cot\left(\frac{\pi-(\phi-\phi')}{2n}\right) F\left[\beta L a^-(\phi-\phi')\right] \\
&+ R^0_{\substack{\perp \\ \parallel}} \cot\left(\frac{\pi-(\phi+\phi')}{2n}\right) F\left[\beta L a^-(\phi+\phi')\right] \\
&+ \left. R^n_{\substack{\perp \\ \parallel}} \cot\left(\frac{\pi+(\phi+\phi')}{2n}\right) F\left[\beta L a^+(\phi+\phi')\right]\right]
\end{aligned}
\tag{D.1}
$$

where the terms R_0 and R_n are the reflection coefficients found in equations (4.4) and (4.5), where 0 refers to the illuminated wedge face (toward the incident field) and n refers to the diffraction face, as shown in Figure 4.2. The distance parameter L is given by [56]

$$
L = \begin{cases} s\sin^2\gamma_o & \text{for plane waves} \\ \dfrac{ss'}{s+s'} & \text{for cylindrical waves} \\ \dfrac{ss'\sin^2\gamma_o}{s+s'} & \text{for spherical waves} \end{cases}
\tag{D.2}
$$

The correction factor, F, based on the Fresnel integral is given by:

$$
F(X) = 2j\left|\sqrt{X}\right| e^{jX} \int_{|\sqrt{X}|}^{\infty} e^{-j\tau^2} d\tau,
\tag{D.3}
$$

where a is given by:

$$
a^{\pm}(\phi\pm\phi') = 2\cos^2\left[\frac{2n\pi N^{\pm}-(\phi\pm\phi')}{2}\right].
\tag{D.4}
$$

$N^{\pm}$ are the integers that most nearly satisfy the four equations

$$
2\pi n N^+ - (\phi\pm\phi') = \pi
\tag{D.5}
$$

$$
2\pi n N^- - (\phi\pm\phi') = -\pi
\tag{D.6}
$$

E. IMPULSE RESPONSE MODEL FOR A MULTIPATH CHANNEL

In this section, the impulse response model for a general multipath channel is developed. The low-pass equivalent model for a general bandpass signal will first be discussed as an introduction to the nomenclature and concepts. The low-pass equivalent model will then be extended to the case of the multipath channel.

E.1 Development of the Low-Pass Equivalent Model for a General Bandpass Signal

For simplification of calculations and simulations of bandpass signals, it is desirable to eliminate the carrier from the analysis and work solely with the baseband signal. This is the motivation behind the development of the equivalent low-pass model of the system. A general bandpass signal, $y(t)$, can be represented as the convolution of an input signal, $s(t)$, (which is often a bandpass signal also) with a bandpass filter having impulse response $h(t)$. This system also can be represented using an equivalent low-pass filter with a complex-valued impulse response and is then called the low-pass equivalent representation [19, pages 40-44].

E.1.1 Representation of a General Bandpass Signal

A general carrier modulated (AM/FM/PM) signal can be represented as:

$$\begin{aligned} s(t) &= A_c(t)\,\cos\left[\omega_c\, t + \theta(t)\right] \\ &= \mathcal{R}e\left[\tilde{s}(t)\, e^{j\omega_c t}\right] \end{aligned} \tag{E.1}$$

where

$$\tilde{s}(t) = A_c(t)\, e^{j\theta(t)} \tag{E.2}$$

In the above, $A_c(t)$ is the time-varying amplitude, $e^{j\theta(t)}$ is the time-varying phase, and ω_c is the carrier frequency. The signal $s(t)$ is a *bandpass signal*, which means its energy will be contained in a band of frequencies surrounding the carrier and will be zero elsewhere. The signal $s(t)$ is real since it physically exists in space. The *complex envelope*, $\tilde{s}(t)$, describes

the amplitude and phase of the baseband part of the signal.

E.1.2 The Bandpass Model

A bandpass signal, $y(t)$, may be modeled as the convolution of the modulated carrier signal, $s(t)$, with the impulse response of a bandpass filter, $h(t)$ (see Figure E.1):

$$y(t) = s(t) \otimes h(t) \tag{E.3}$$

where:

$$s(t) = \mathcal{R}e\left[\tilde{s}(t)\, e^{j\omega_c t}\right] \tag{E.4}$$

$$h(t) = \mathcal{R}e\left[\tilde{h}(t)\, e^{j\omega_c t}\right] \tag{E.5}$$

$$y(t) = \mathcal{R}e\left[\tilde{y}(t)\, e^{j\omega_c t}\right] \tag{E.6}$$

and $\otimes$ denotes convolution

Note that $s(t)$, $h(t)$, and $y(t)$ are all real signals and $\tilde{s}(t)$, $\tilde{h}(t)$, and $\tilde{y}(t)$ are all complex signals.

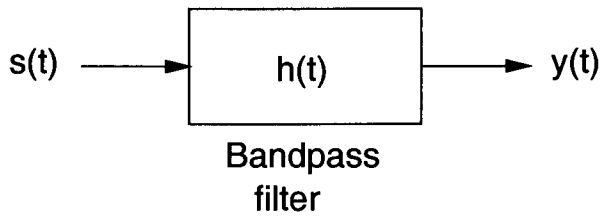

Figure E.1: Block diagram of a bandpass filter.

The frequency domain representation of the impulse response $h(t)$ may be found from the Fourier transformation of (E.5):

$$H(f) = \frac{1}{2}\tilde{H}\left[f - f_c\right] + \frac{1}{2}\tilde{H}^*\left[-f - f_c\right] \tag{E.7}$$

where $\tilde{H}^*$ represents the complex conjugate of $\tilde{H}$. The magnitude spectrum of $H(f)$ is that of a bandpass signal, as shown in Figure E.2.

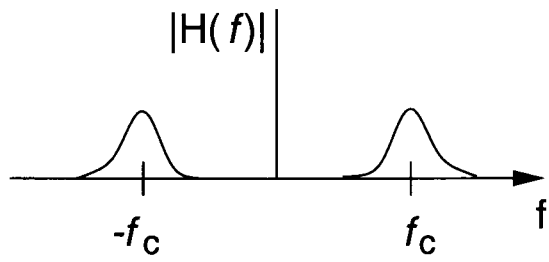

Figure E.2: The magnitude spectrum of a bandpass signal.

E.1.3 The Equivalent Low-Pass Model

To derive the equivalent low-pass model, the bandpass filter impulse response is represented using an equivalent low-pass filter with a complex-valued impulse response. Again, it is convenient to work in the frequency domain. The Fourier transformation of $y(t) = s(t) \otimes h(t)$ may be written using (E.4)-(E.6) as

$$\frac{1}{2}\widetilde{Y}[f-f_c] + \frac{1}{2}\widetilde{Y}^*[-f-f_c] = \left(\frac{1}{2}\widetilde{S}[f-f_c] + \frac{1}{2}\widetilde{S}^*[-f-f_c]\right) \times \left(\frac{1}{2}\widetilde{H}[f-f_c] + \frac{1}{2}\widetilde{H}^*[-f-f_c]\right) \quad \text{(E.8)}$$

Note:

$$\begin{aligned} \widetilde{S}[f-f_c] \times \widetilde{H}^*[-f-f_c] &= 0 \\ \widetilde{S}^*[-f-f_c] \times \widetilde{H}[f-f_c] &= 0 \end{aligned}$$

since there is no spectral overlap.

Therefore:

$$\frac{1}{2}\widetilde{Y}[f-f_c] + \frac{1}{2}\widetilde{Y}^*[-f-f_c] = \frac{1}{2}\widetilde{S}[f-f_c]\,\frac{1}{2}\widetilde{H}[f-f_c] + \frac{1}{2}\widetilde{S}^*[-f-f_c]\,\frac{1}{2}\widetilde{H}^*[-f-f_c] \quad \text{(E.9)}$$

With a change of variables, $f - f_c \rightarrow f$,

$$\begin{aligned} \frac{1}{2}\widetilde{Y}(f) &= \frac{1}{2}\widetilde{S}(f) \times \frac{1}{2}\widetilde{H}(f) \\ \widetilde{Y}(f) &= \widetilde{S}(f) \times \frac{1}{2}\widetilde{H}(f) \end{aligned} \quad \text{(E.10)}$$

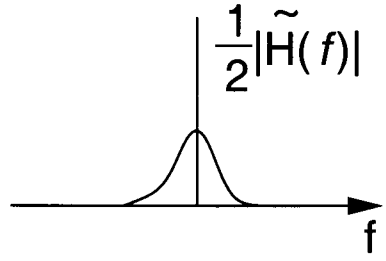

Figure E.3: Magnitude response of a low-pass filter.

The magnitude spectrum of the equivalent low-pass filter is shown in Figure E.3.
Note that $|\tilde{H}(f)|$ does not have to be symmetric. It can, however, be decomposed into in-phase and quadrature phase components which exhibit symmetry and antisymmtery respectively. In the time domain (E.10) can be written as

$$\tilde{y}(t) = \tilde{s}(t) \otimes \frac{1}{2}\tilde{h}(t) \tag{E.11}$$

where $\tilde{s}$(t), $\tilde{h}(t)$, and $\tilde{y}(t)$ are, again, all complex signals. See Figure E.4 for a schematic representation of the low-pass equivalent system.

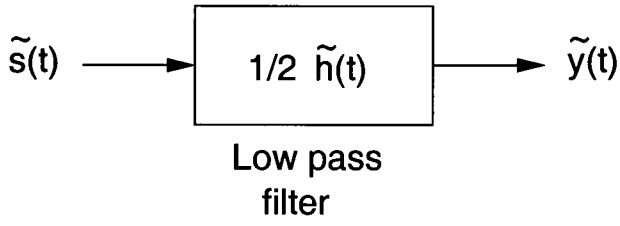

Figure E.4: Block diagram of a low-pass filter.

E.2 Low-Pass Equivalent for a Discrete Multipath Channel

In an indoor propagation environment, multipath signals often occur because of reflection and diffraction from objects and surfaces in the vicinity of the transmitter and receiver. When there is no overlap between received multipath signal components, as,

for example, when a short duration pulse is used in channel sounding, the channel is characterized as a *discrete* multipath channel. Each discrete path will have an associated time delay and attenuation. The multipath channel can then be modeled as a filter which allows signals containing any range of frequency components to pass with an appropriate time delay and attenuation. For cases where the transmitter, receiver, and/or a multipath-producing object are in motion, the attenuation and time delay may be time varying as well. In the following, t represents the time variation due to motion ($d = vt$, with d=distance and v=velocity) and τ represents the channel multipath delay for a fixed time t.

In the next section, the low-pass equivalent impulse response of the multipath channel [19, pages 374-375] will be derived in a manner similar to that presented in Section E.1 for the low-pass equivalent of the bandpass signal. Because $h(t)$ for the multipath signal is broadband (as opposed to bandpass), some differences in the derivation exist and these will be highlighted.

E.2.1 Channel Representation Without Motion

The multipath signal may be modeled in a manner similar to that for a bandpass signal, where now the impulse response $h(\tau)$ of the multipath channel replaces $h(t)$ of the bandpass signal channel in the previous example. The impulse response for an ideal multipath channel, whose characteristics were described above, may be given by

$$h(\tau) = \sum_{k=0}^{N-1} a_k \, \delta(\tau - \tau_k) \tag{E.12}$$

where $h(\tau)$ is broadband (rather than bandpass).

In the above

a_k are the (real) amplitudes of each multipath component

N is the total number of multipath signal components

τ_0 represents the first arriving signal at the receiver

τ_k are the excess delays (i. e., time delays greater than τ_o)

and δ is the delta function.

The received multipath signal then may be represented as follows:

$$\begin{aligned} y(\tau) &= s(\tau) \otimes h(\tau) \\ &= \int_0^{\tau} s(\eta)\, h(\tau - \eta)\, d\eta \\ &= \sum_{k=0}^{N-1} a_k\, s(\tau - \tau_k) \end{aligned} \tag{E.13}$$

The integration limits in (E.13) are due to signal causality. Convolution with delta functions implies that the received multipath signals are exact copies of the original signal, delayed in time and reduced (generally) in amplitude. Pulse spreading effects (dispersion) and other nonidealities are neglected in this model.

In (E.12), τ_0 represents the first arriving multipath signal. By convention it is set equal to zero, neglecting the propagation delay between transmitter and receiver. All other delays, τ_k, are measured relative to τ_0 and are called *excess delays*. One measure of the severity of multipath in a channel is the excess delay spread, which indicates the time range over which multipath signals with amplitude above a given threshold exist.

E.2.2 Low-Pass Representation of the Channel Response

To find the low-pass representation of the channel in the form of (E.11), write the bandpass response of the multipath signal given in (E.13) using the form for $s(t)$ given in (E.4)

$$\begin{aligned} y(\tau) &= s(t) \otimes h(t) \\ y(\tau) &= \mathcal{R}e\left[\tilde{s}(\tau)\, e^{j\omega_c \tau}\right] \otimes h(\tau) \\ &= \mathcal{R}e\left[\tilde{s}(\tau)\, e^{j\omega_c \tau} \otimes h(\tau)\right] \end{aligned} \tag{E.14}$$

Note that even though $h(\tau)$ is a real signal, it cannot be represented in the form given in (E.5) because it is not a bandpass signal.

Substituting the expression for $h(\tau)$ from (E.12)

$$y(\tau) = \mathcal{R}e\left[\sum_k a_k\, \tilde{s}(\tau - \tau_k) e^{j\omega_c(\tau - \tau_k)}\right]$$

$$= \mathcal{R}e\left[\left(\sum_k a_k e^{-j\omega_c\tau_k}\ \tilde{s}(\tau-\tau_k)\right) e^{j\omega_c\tau}\right] \tag{E.15}$$

Identify

$$\tilde{y}(\tau) = \sum_k a_k\ e^{-j\omega_c\tau_k}\ \tilde{s}(\tau-\tau_k) \tag{E.16}$$

Then the complex equivalent low-pass impulse response can be represented as

$$\tilde{h}(\tau) = \sum_k a_k\ e^{-j\omega_c\tau_k}\ \delta(\tau-\tau_k) \tag{E.17}$$

This is often written as

$$\tilde{h}(\tau) = \sum_{k=0}^{N-1} a_k\ e^{-j\theta_k}\ \delta(\tau-\tau_k) \tag{E.18}$$

or

$$\tilde{h}(\tau) = \sum_{k=0}^{N-1} \tilde{a}_k\ \delta(\tau-\tau_k) \tag{E.19}$$

with $\theta_k = \omega_c\tau_k$ or equivalently, $\tilde{a}_k$ is the k_{th} complex amplitude coefficient. Note that this low-pass representation is a complex-valued function dependent on the time delay, τ_k, associated with the k_{th} multipath component. Also note that because $h(\tau)$ is not a bandpass signal (and thus cannot be represented in the form of (E.5)), the factor of 1/2 due to the Fourier transformation of the bandpass signal in (E.11) does not appear in (E.17) – (E.19).

E.2.3 Incorporation of Reflection Coefficients

When a path contains a specular reflection, the reflection coefficient $\rho = a_\rho e^{j\phi_\rho}$ may be incorporated into the impulse response as follows. The phase change $\phi_{\rho,k}$ for the k_{th} multipath signal component can be represented in the time domain as $\phi_{\rho,k} = \tau_{\rho,k}\ \omega_c$ (see Figure E.5), assuming negligible frequency dependence of the reflection coefficient around ω_c. In this case, the complex equivalent low-pass impulse response for the k_{th} component of the multipath signal is

$$\begin{aligned}\tilde{h}_k(\tau) &= a_k a_\rho\ \delta(\tau-\tau_k)\ e^{-j\omega_c(\tau_{\rho,k}+\tau_k)} \\ &= a_{\rho,k}\ \delta(\tau-\tau_k)\ e^{-j(\theta_k+\phi_{\rho,k})}\end{aligned} \tag{E.20}$$

where $\omega_c\ \tau_{\rho,k}$ is the phase of the reflection for the k_{th} multipath signal component, and $a_{\rho,k} = a_k a_\rho$. The value of $a_{\rho,k}$ is determined by the propagation path without reflections, and a_ρ and τ_ρ depend on the reflection coefficient. For multiple reflecting surfaces, $\phi_{\rho,k} = \omega_c\ \tau_{\rho,k}$ is the sum of all phase changes and $a_{\rho,k}$ is the product of the amplitude coefficients.

The effect of the reflection coefficient phase term, $\phi_{\rho,k}$, is to add a constant phase change to the carrier phase of the k_{th} multipath signal component. This can be a problem in a multipath signal, since each reflecting path will change the absolute phase of the carrier by a different amount. This is one reason non-coherent detection is desirable in wireless communication channels. The absolute phase of the carrier is not important in non-coherent detection.

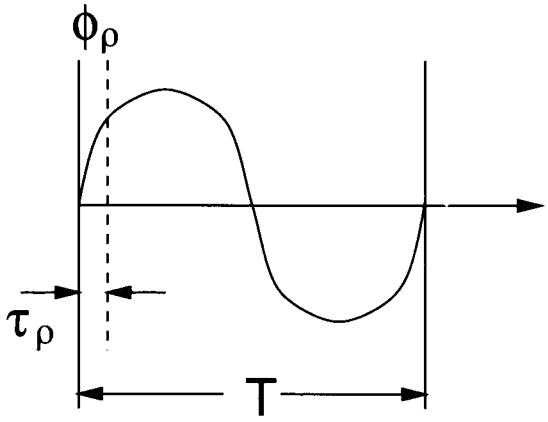

Figure E.5: Determination of ϕ_ρ and τ_ρ of a reflection coefficient.

E.2.4 Channel Representation Including Motion

When motion is added, the impulse response is a function of the position of the receiver and is given by $h(d,\tau)$ [1, pages 143-147]:

$$\begin{aligned} y(d,\tau) &= s(\tau) \otimes h(d,\tau) \\ &= \int_{-\infty}^{\tau} s(\eta)\ h(d,\tau-\eta)\, d\eta \end{aligned} \tag{E.21}$$

When v is constant over a short time or distance, the impulse response may be written as a function of t and τ:

$$\begin{aligned} y(t,\tau) &= s(\tau) \otimes h(t,\tau) \\ &= \int_0^{\tau} s(\eta)\, h(t,\tau-\eta)\, d\eta \end{aligned} \tag{E.22}$$

where t represents time variations due to motion and, again, τ is the channel multipath delay for a fixed value of t. Various parameters will now be functions of the motion:

$$\tau_k \rightarrow \tau_k(t), \quad \tilde{h}(\tau) \rightarrow \tilde{h}(t,\tau), \quad \phi_{\rho,k} \rightarrow \phi_{\rho,k}(t)$$

Then,

$$\tilde{h}(t,\tau) = \sum_k a_{\rho,k}(t)\, e^{-j(\omega_c \tau_k + \phi_{\rho,k}(t))}\, \delta\left[\tau - \tau_k\right] \tag{E.23}$$

The reflection coefficient will change depending on the angle of incidence, that is, it will change with motion, but it is still not a function of τ.

F. THE RELATIVE PHASE METHOD

Utilizing the relative phase method, the radar cross section, σ_a, due to N scattering elements on a body is given by:

$$\sigma_a = \left| \sum_{j=1}^{N} (\sigma_j)^{1/2} \exp(i\phi_j) \right|^2 , \tag{F.1}$$

where σ_j is the RCS of the jth component and ϕ_j is the relative phase angle associated with the jth component. The RCS is related to the electromagnetic fields by:

$$\sigma = 4\pi \lim_{R\to\infty} R^2 \frac{\left|\vec{E}^s\right|^2}{\left|\vec{E}^i\right|^2} = 4\pi \lim_{R\to\infty} R^2 \frac{\left|\vec{H}^s\right|^2}{\left|\vec{H}^i\right|^2} \tag{F.2}$$

where $|\vec{E}^s|$, $|\vec{H}^s|$ are the scattered electric and magnetic fields, respectively, and $|\vec{E}^i|$, $|\vec{H}^i|$ are the incident fields.